5-7-2014

# Magnetic Apatites for Biomedical Applications

Erica R. Kramer
erica.kramer@uconn.edu

# Magnetic Apatites for Biomedical Applications

Erica Kramer, Ph. D

University of Connecticut 2014

Biomedical applications utilizing magnetic nanoparticles have the ability to impact diagnostic and therapeutic outcomes and beneficially affect numerous patients worldwide. Paramagnetic nanoparticles can potentially be used to improve targeting in drug delivery systems, improve contrast in biomedical imaging, and treat cancer via hyperthermia. Unfortunately, the most widely used type of nanoparticles for several biomedical applications are currently iron oxides. Safety is a constant concern when using these types of materials as toxicity limits therapeutic efficiency, as well as having the potential to induce new damage and problems in the patient's cells. For these reasons, iron oxide particles often require the application of a biocompatible coating, which can be unstable.

Hydroxyapatite, the main inorganic component of natural bone, is widely studied as a biomaterial due to its excellent biocompatibility. Furthermore, the crystal structure of hydroxyapatite lends itself to a wide variety of substitutions and ion doping, which allows for tailoring of material properties. Substituted hydroxyapatite with paramagnetic properties is of interest as a promising biomaterial to be used to replace iron oxides in biomedical applications. In this work, both iron- and cobalt-substituted hydroxyapatite powders were synthesized. Iron-substituted hydroxyapatite (FeHA) was created by subjecting pure hydroxyapatite to a simple room temperature ion exchange procedure. Cobalt-substituted hydroxyapatite (CoHA) was

synthesized using both ion exchange and via wet synthesis. All resulting powders were carefully characterized to verify that the ion of interest had substituted into the apatite lattice, thus yielding a phase-pure material. Iron- and cobalt-substituted hydroxyapatites were further found to be materials with paramagnetic properties. Both materials were subjected to sintering and cell culture studies to evaluate their stability and suitability for the proposed applications of drug delivery, MRI contrast agents, and nanoparticles for hyperthermia based cancer treatments. Characterization of these substituted apatite materials indicate that FeHA and CoHA are biodegradable and biocompatible materials with paramagnetic properties, thus resulting in a wider range of potential applications than pure HA, including, but not limited to, cell stimulation in bone repair, cell labelling and separation, and combined therapies, as well as drug delivery, MRI contrast agents, and hyperthermia based cancer treatments.

# Magnetic Apatites for Biomedical Applications

**Erica Kramer, Ph.D.**

**Bachelor of Science, University of Connecticut, 2008**

**A Dissertation**

**Submitted in Partial Fulfillment of the**

**Requirements for the Degree of Doctor of Philosophy**

**at the**

**University of Connecticut**

**2014**

**APPROVAL PAGE**

**Doctor of Philosophy Dissertation**

**Magnetic Apatites for Biomedical Applications**

**Presented by Erica Kramer, B.S.**

**Major Advisor** _____
**Mei Wei**

**Associate Advisor** _____
**Menka Jain**

**Associate Advisor** _____
**Montgomery T. Shaw**

**University of Connecticut**
**2014**



iv

**Acknowledgements**

First and foremost, I would like to extend my greatest appreciation to my advisor, Dr. Mei Wei. The amount of support and encouragement provided by Dr. Wei during the course of my studies cannot be overstated. I am also thankful to my associate advisors, Dr. Menka Jain and Dr. Monty Shaw, for their invaluable support and suggestions. I am greatly appreciative of the helpful discussions and ideas provided by Dr. Joseph Budnick as well.

I would like to thank everyone who has helped me conduct experiments: Dr. Lichun Zhang, Dr. Roger Ristau, Dr. Jack Gromek, Dr. Heng Zhang, Dr. Bill Hines, Dr. Aimee M. Morey, Dr. Margo Staruch, Gary Lavigne, and Laura Pinatti. I also need to acknowledge the support provided by the department staff in the Materials Science and Engineering department and the Institute of Materials Science, including Deborah Perko, Nancy Kellerann, Cathy McCracken, Maria Mejias, Kimberly Post, and Trista Albert.

I would like to acknowledge my labmate Michael Zilm for his assistance with cell culture studies, and also for the valuable discussion and collaboration. I would also like to thank Fei Peng, Xiaohua Yu, Zengmin Xia, Max Villa, Drew Clearfield, Stephanie Bendtsen, Jonathan Russo and Changmin Hu. It was a great pleasure to work in the lab with them.

Last, but not least, I would like to thank my parents, my siblings, and my husband for their unconditional love and support.

**Table of Contents**

**LIST OF TABLES**

**LIST OF FIGURES**

# Chapter 1

## Introduction

### *1.1 Hydroxyapatite*

Hydroxyapatite (HA, $Ca_{10}(PO_4)_6(OH)_2$) is the mineral phase of natural bone [1, 2]. It comprises about 70 wt % of bone, and naturally occurs as plate or needle-shaped crystals about 40-60 nm long and 20 nm wide. HA also comprises about 97 wt % of dental enamel, in the form of larger HA crystals about 160-1000 nm long and 40-120 nm wide. Naturally occurring HA is non-stoichiometric and includes incorporated ions such as $Na^+$, $Mg^{2+}$, $K^+$, $F^-$, $Cl^-$ and $CO_3^{2-}$, as well as $H_2O$ [3, 4]. Because of its biocompatibility and bioactivity, synthetic HA is commonly generated and widely applied to biomedical applications such as bone replacement, tissue engineering, drug delivery, and as a bioactive coating [3-5].

Ideally, synthetic HA is a hexagonal material, belonging to space group $P6_3/m$. The unit cell is made up of 44 atoms (Fig. 1.1), and has unit cell dimensions of a=b=9.432 Å, c=6.881 Å. Stoichiometric HA has a calcium to phosphate (Ca/P) ratio of 1.67 [6-8].

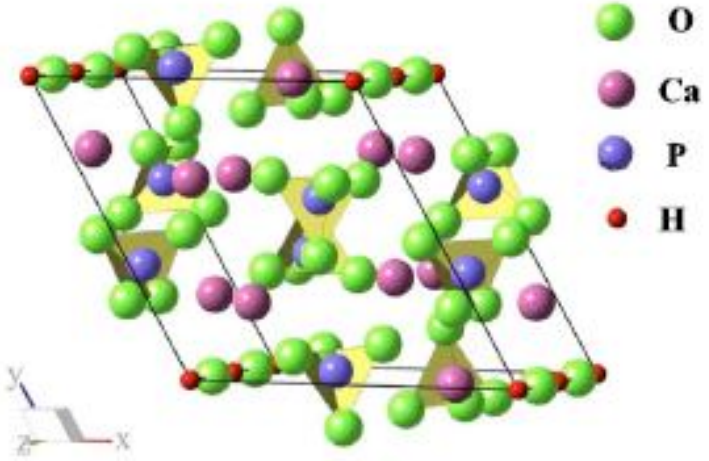


**Figure 1.1** The hydroxyapatite crystal unit cell. [6]

*1.2 Synthesis of Hydroxyapatite*

Synthetic HA particles can be obtained using a wide variety of synthesis methods. Each method has different advantages and disadvantages, and yields HA with certain typical characteristics.

*1.2.1 Synthesis from Biogenic Sources*

HA ceramics can be generated from biogenic sources. These may be better accepted *in vivo* because of physiochemical properties more similar to human bone [9]. The general procedure required to obtain HA from biowaste sources (bovine bones, fish bones, etc.) is to anneal the source material, thereby burning away any organic residue, and then subject the inorganic resultant material to enzymatic hydrolysis or alkaline hydrothermal hydrolysis [9-11]. Alternatively, marine organism skeletons or egg shell waste can be used as the calcium carbonate pre-cursor material in HA synthesis [12, 13].

*1.2.2 Dry Synthesis Methods*

Dry methods are used to generate HA without the use of a solvent. These methods yield HA powders whose characteristics are not strongly influenced by processing parameters, and as such, processing conditions do not need to be carefully controlled, making dry methods suitable for mass production of HA [9]. Solid-state, also known as dry chemical, synthesis utilizes calcium and phosphate containing chemical precursors. These precursors are milled, and then calcined at high temperatures. The disadvantage of solid state synthesis is that the resultant powders have phase composition heterogeneity and irregularly shaped particles [9, 14]. Mechanochemical synthesis, another dry synthesis method, uses a stoichiometric molar ratio of reagents ground in a planetary mill to yield HA. Although this results in a powder with well-defined structure, the phase purity is low using this synthesis method [9, 15]. Dry synthesis methods have recently become unpopular, due to the above noted disadvantages.

*1.2.3 High Temperature Synthesis Methods*

High temperature synthesis methods are characterized by the use of elevated temperatures hot enough to burn or partially burn the precursor materials. The solution combustion method depends on a rapid self-sustaining and exothermic reaction between oxidants and organic fuel in an aqueous phase. The reaction is initiated by heating at a relatively low temperature followed by a sudden increase in temperature and then rapid cooling. The rapid cooling serves to induce nucleation and prevent crystal growth. This one-step process yields high purity HA powder [9, 16, 17].

Another high temperature process is pyrolysis. This process produces HA powder by spraying a precursor solution into a flame or hot zone, and allowing the resultant vapors to react

at high temperature. There are still relatively few studies applying this method to HA synthesis, but the powder generated is stoichiometric, homogenous, and highly crystalline. Unfortunately, there is poor control over the processing variables using this method [9].

*1.2.4 Wet Synthesis Methods*

Wet synthesis methods are the most commonly used HA synthesis processes. These methods yield HA with nanosized structure and regular morphology. Furthermore, HA growth conditions, and therefore final HA properties, can be controlled by adjusting the system parameters. The main disadvantage to wet methods in general is that the low processing temperatures result in the formation of secondary calcium phosphate (CaP) phases and low material crystallinity. Trace impurities can also be incorporated into the HA lattice from ions in solution [9].

One wet synthesis method is hydrolysis. Using this technique, hydrolysis of other CaP phases by dissolution and precipitation yields HA. This technique takes advantage of the fact that acidic CaP salts are less thermodynamically stable at neutral and alkaline pH than HA. [18-22]

The sol-gel method utilizes a 3-D network of precursors (calcium alkoxides) in an aqueous or organic solvent. Low temperature aging, followed by gelation, and then calcination to burn off the organic residues results in HA formation. The reaction between calcium and phosphate occurs during the aging step. The molecular level mixing of reactants using this method results in improved chemical homogeneity of HA, but a secondary phase (typically CaO) is usually generated. [23-28]

In hydrothermal HA synthesis, the reaction of reagents is carried out in an aqueous solution at elevated temperatures and pressures, yielding highly crystalline HA. The disadvantages of this method are poor control over particle morphology and size distribution, as well as the need for expensive equipment [29-32]. The emulsion method utilizes a surfactant to better control particle size and morphology and limit aggregation [9]. Sonochemical synthesis can also be used, where the essential chemical reactions are activated by ultrasound radiation, resulting in uniform, small crystals [9].

The most common of all HA synthesis techniques is the wet-chemical, or wet precipitation, method [9]. In this process, calcium and phosphate containing solutions are mixed by dropwise addition of one into the other under continuous stirring. The characteristics of the resultant HA powder can be controlled by factors including, but not limited to, pH, temperature, and concentration of reagents [9, 33-43]. As with all wet synthesis methods, the HA yielded by wet precipitation has relatively low crystallinity.

### *1.3 Substitutions in Hydroxyapatite*

A wide variety of anions, cations, vacancies, and functional groups can be substituted into the HA lattice. The ability of HA to accept such a wide range of substitutions is a result of the apatite crystal structure being both flexible and highly stable [44, 45]. Cations substitute into the calcium sites in the HA lattice, while anions replace either the phosphate or hydroxyl groups [45-48]. Common anion substitutions include $F^-$ and $CO_3^{2-}$ in both natural and synthetic HA [45]. Naturally occurring apatites are in fact never chemically pure, as they take full advantage of the ability of the apatite structure to accept ionic substitutions. Synthetic HA substitutions may be achieved by modified synthesis procedures and/or by ion exchange procedures [48].

Cationic substitutions can be divalent, monovalent, trivalent, tetravalent, or even hexavalent. Cationic substitutions of interest that can be achieved include, but are not limited to, $Zn^{2+}$ [45,49-51], $Ni^{2+}$ [52], $Mg^{2+}$ [51, 53-55], $Mn^{2+}$ [56-59], $Sr^{2+}$ [44,45], $Na^{+}$ [45], $U^{4+}/U^{6+}$ [45], rare earth elements [45,51,60,61], and $Fe^{2+}/Fe^{3+}$ [56-58, 62-67].

Substitutions in HA allow for the physical, chemical, mechanical, and biological properties of the material to be tailored. An example of the ability to control HA material properties by substitutions is the ability to alter HA magnetic properties. Pure HA is diamagnetic, but substitution or incorporation of metal ions with magnetic properties may yield HA material with paramagnetic properties.

*1.4 Potential applications for hydroxyapatite with magnetic properties*

The use of magnetic materials in biomedical applications such as drug delivery, medical imaging, or hyperthermia based cancer treatments, just to name a few, has the potential to greatly improve the prognosis for numerous patients worldwide suffering from a wide variety of diseases and conditions. The advantages that magnetic nanoparticles bring are their small size, which allows them to interact with the system of interest at the cellular or sub-cellular level, and most importantly “action at a distance”. Magnetic nanoparticles respond to magnetic fields and since a magnetic field can penetrate human tissue the particles can be manipulated by external magnetic fields. Additionally, magnetic nanoparticles can resonantly respond to a time varying magnetic field, for example by generating heat [68-72].

### 1.*4.1 Drug Delivery*

Drug delivery is a "method or process of administering a pharmaceutical compound to achieve a therapeutic effect in humans or animals" [73]. The development of drug delivery systems is attractive in that it allows for the improvement in safety and efficacy of currently available pharmaceutical molecules, without the need to conduct the expensive and time consuming process of developing new drugs. It is estimated that the development of a new drug from discovery through regulatory approval takes about 10 years and at least $120 million. This makes the development of improved drug delivery systems a more realistic approach to improving patient outcomes [73, 74].

The major disadvantage of most chemotherapies is that intravenous administration leads to systemic and non-specific distribution. Specific targeting to a tissue or region of interest (such as a tumor) results in lower side effects and a lower necessary dosage of drug due to increased efficiency. In magnetically targeted drug therapy, a drug is attached to a biocompatible magnetic nanoparticle carrier. The drug/carrier compound is then concentrated at the target site by an external high gradient magnetic field. Once at the target site the drug is released, by either enzymatic activity or changes in surrounding conditions such as pH. The general concept of a magnetic drug delivery system is illustrated in Fig. 1.2 [68].

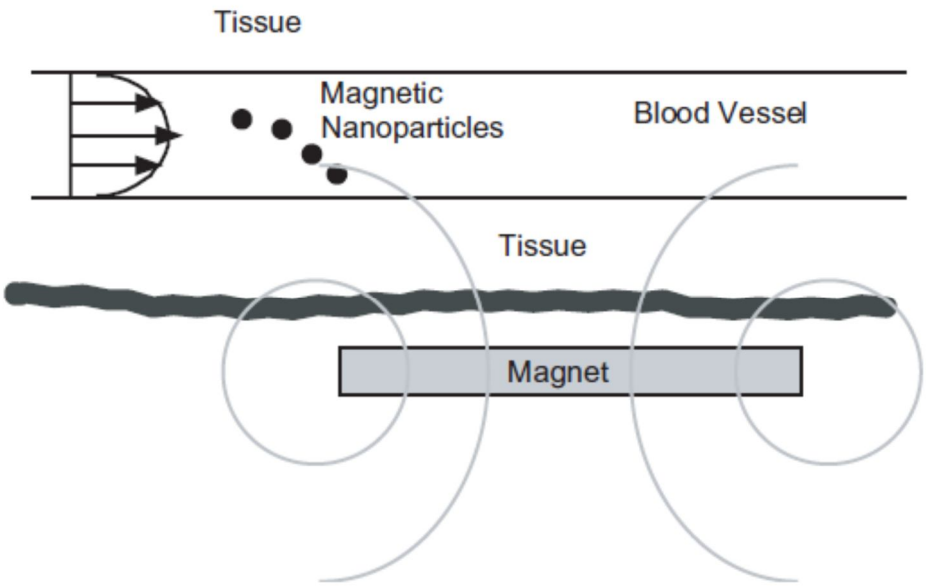


**Figure 1.2** A schematic of a hypothetical magnetic-targeting based drug delivery system in which a magnet placed outside the body will attract and concentrate magnetic nanoparticle drug carriers to the tissue region of interest [68].

There have been studies conducted in which magnetic targeting of drugs has been shown to be successful. For example, Gallo et al. used magnetic microspheres to deliver drugs to the brains of mice. The resulting drug concentrations in the brain were 100-400x the concentrations when a drug solution alone was used [75]. In order for magnetic targeting to successfully concentrate the carrier-drug compound in the tissue region of interest the magnetic force must overcome the hydrodynamic drag force acting on the magnetic particle as a result of flow in the blood vessel [68]. The effectiveness of magnetic drug delivery will be influenced by factors including blood flow rate, the concentration of the delivery solution, magnetic field strength and gradient, the volumetric and magnetic properties of the magnetic nanoparticle, and physiological parameters such as tissue depth.

*1.4.2 MRI Contrast Agents*

Nuclear magnetism is exhibited by all nuclei with an odd number of protons and/or neutrons. When such nuclei are exposed to a magnetic field there is a measureable effect on their magnetization. The removal of the applied magnetic pulse results in the magnetization undergoing relaxation processes to return to equilibrium [76]. These relaxation processes result in two quantities, $T_1$ (spin-lattice, or longitudinal) and $T_2$ (spin-spin, or transverse) Magnetic resonance imaging (MRI) relies on the fact that the extremely large number of protons in biological tissue results in an accumulative effect of the protons' magnetic moments, each of which is exceedingly small, having measureable relaxation times [68,76].

MRI is the "gold standard" for imaging soft tissue such as the central nervous system, and it can also be used for functional imaging of the brain and heart, as well as the detection of tumors [76, 77]. MRI can also be used to image bones and joints. Each tissue type has unique $T_1$ and $T_2$ relaxation times. Furthermore, these relaxation times can be affected by disease or injury states. The magnetic susceptibility of tissue also changes as a result of blood oxygenation, allowing for functional as well as structural imaging. The typical $T_1$ and $T_2$ values for common tissues are summarized in Table 1.1 [76].

**Table 1.1** Typical $T_1$ and $T_2$ relaxation times for various tissue types [76]

| Tissue | $T_1$ (ms) | $T_2$ (ms) |
|---|---|---|
| Gray matter | 520 | 95 |
| White matter | 380 | 85 |
| Typical edema or infarction | 600 | 150 |
| Malignant tumor | 800 | 200 |
| Fat | 160 | 100 |
| CSF | 2000 | 1000 |

While $T_1$ and $T_2$ relaxation times provide natural contrast in MRI imaging, the relaxation time differences between healthy and abnormal tissue can be quite small. Contrast agents can be used to shorten the relaxation times of human body tissues, and thus emphasize the small differences in relaxation times and improve contrast. This relies upon differential uptake of contrast agents in different types of tissue. Fig. 1.3 shows the effect of MnO nanoparticle $T_1$ contrast agent on the structural imaging of a brain.

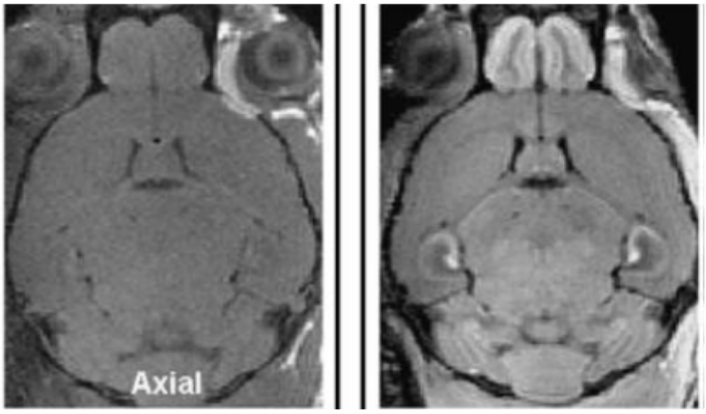


**Figure 1.3** MRI imaging of the axial plane of the brain without (left) and with (right) the use of MnO nanoparticle $T_1$ contrast agent [78].

*1.4.3 Hyperthermia-based cancer treatments*

It has been determined that hyperthermia increases the effect of radiation and chemotherapy treatments for cancer. Additionally, hyperthermia by itself can kill cells if temperatures in the tissue are maintained at around 42°C. Because malignant cells have shown to be more thermo sensitive than surrounding normal cells, hyperthermia-based treatments are attractive possibilities in the fight against cancer [77, 78]. Experimental tests using magnetic materials for hyperthermia date to Gilchrist et al.'s work in 1957 where tissue samples were heated by iron oxide nanoparticles under a 1.2 MHz magnetic field [68].

The main procedure for magnetic nanoparticle based hyperthermia is to disperse magnetic particles in the target tissue, apply an AC magnetic field of sufficient strength and frequency to heat the particles, and maintain the temperature in the tissue at the therapeutic threshold of 42°C for at least 30 minutes. The use of magnetic nanoparticles, as opposed to other types of hyperthermia devices, is preferable because the specific tissue of interest can be targeted and heated, without heating healthy tissue to damaging temperatures [68, 71].

*1.4.4 Iron Oxides: the problem with currently used magnetic nanoparticles in biomedical applications*

The most widely used para- and superpara-magnetic nanoparticles for biomedical applications are iron oxides. Although it is widely believed that iron oxides are well tolerated by the human body, in fact the human body stores iron in the iron oxide form, there are toxicity concerns associated with iron oxide nanoparticles that require the application of a biocompatible coating. Iron oxide nanoparticles are also non-degradable. Aggregations of iron oxide

nanoparticles can form embolisms and block blood flow [81, 82]. Uncoated iron oxide nanoparticles have been shown to be cytotoxic, with cell viability reduced by 20% at a concentration of 0.05 mg/mL and up to 50% at higher concentrations [75].

Iron oxide nanoparticles have been associated with a wide range of toxic effects. *In vivo*, these effects have included inflammation and formation of apoptotic bodies. In addition, iron oxide nanoparticles have been associated with impaired mitochondrial function, membrane leakage of lactate dehydrogenase, genotoxicity, chromosome condensation, and the generation of reactive oxygen species [83]. Reactive oxygen species (ROS), such as the superoxide ion ($O^{2-}$) are highly reactive molecules. ROS can strip electrons from cellular macromolecules and have damaging effects on cells [75].

In addition to toxicity, uncoated iron oxide nanoparticles have low solubility, causing precipitation and aggregation. Therefore, iron oxide nanoparticles typically require an ampiphilic biocompatible coating for clinical applications. Unfortunately, evidence suggests that coatings of some commercially available coated iron oxides (for example, those coated with dextran) are prone to detachment [83]. The biocompatibility and biodegradability of HA means that the application of HA with magnetic properties may minimize the toxicity concerns inherent with the use of iron oxide nanoparticles without the need for a potentially unstable coating.

### *1.5 Objectives of this research*

As described in the previous section, there is a pressing need for biocompatible magnetic nanoparticles for a wide range of applications in the biomedical field. Most studies to date have used iron oxide nanoparticles for these applications, but the toxicity concerns associated with these materials are widespread. In comparison, hydroxyapatite is a well-known and widely used

bioceramic with excellent biocompatibility. The ability to make substitutions into the apatite lattice allows for the tailoring of HA material properties, and the potential inclusion of paramagnetic properties.

The objective of the research shared here is to establish simple procedures for the synthesis of substituted hydroxyapatites with paramagnetic properties. Initially, pure HA was synthesized, and the control of HA morphology was investigated, as different applications call for different size and shape HA particles. Iron- and cobalt-substituted HA powders were then synthesized and fully characterized to determine the effect of each substitution of interest on overall material properties, not just magnetic. Iron substituted HA (FeHA) was achieved using a simple ion exchange procedure. Cobalt substituted HA (CoHA) was achieved via both ion exchange and wet synthesis procedures. The resulting substituted apatites were shown to have paramagnetic properties. The effect of the iron and cobalt substitutions on phase purity and crystal structure were examined and it was established that $Fe^{3+}$ and $Co^{2+}$ substituted into the apatite lattice without the formation of second phases. The sintering behavior, *in vitro* degradation behavior, and *in vitro* biocompatibility of each substituted apatite was compared to that of pure HA, and the results serve as a guide to establish what types of potential applications would be suitable for each substituted apatite studied.

# Chapter 2

## Control of hydroxyapatite nanoparticle morphology using wet rate effects synthesis techniques: Reactant addition

### *2.1 Introduction*

The basic building block of natural bone is mineralized collagen fibrils, with the main mineral phase being hydroxyapatite (HA) [1, 2]. Due to its biocompatibility and bioactivity, synthetic HA is well suited to biomedical applications [5]. In bone, the morphology of HA is nano-sized needle-like crystals. Clinically, it may be used in various forms including powders, granules, dense and porous blocks, and in composites [4]. There are many techniques that have been used to synthesize HA particles, such as wet chemical synthesis, dry chemical synthesis, and sol-gel. Using wet synthesis techniques, by controlling various reaction parameters the characteristics of HA, such as purity, crystallinity, and morphology, can be controlled. The objective of the work in this chapter was to systematically study the effect that changing reactant addition rate has on HA particle morphology. On a practical level this is useful, because different morphologies may be desirable for different applications. For example, small spherical particles may be desired for use in thermal spray coatings, whereas needle-shaped or rod-shaped particles may be used in bone-repair composite materials.

There have been widespread studies on the effect of process parameters on HA morphology, such as temperature [33-36, 84], pH [37, 84], Ca/P ratio [37], and starting solution concentration [35-37]. In the literature, reactant addition rate has been studied in terms of HA purity [85,86] and effect on particle shape factor [85]. It is the author's belief that the work

presented in this chapter is the first study of the effect of reactant addition rate on size and morphology that considers a wide range and large number of rates.

## *2.2 Materials and Methods*

### *2.2.1. Solution Preparation:*

Two solutions were prepared for the production of HA. Solution 1 contained 600 mL of deionized water and 12 grams of calcium nitrate tetrahydrate (99%, Fisher). Solution 2 contained 200 mL of deionized water, 4 grams of ammonium phosphate (99+%, Acros), and 80 mL of ammonium hydroxide (~30%, Fisher). The ammonium phosphate was added to the deionized water, with the ammonium hydroxide being added after the ammonium phosphate completely dissolved. This solution was then titrated into Solution 1. Solution 1 was maintained under constant stirring of about 200 rpm.

### *2.2.2 Performing the Titrations*

Solution 2 was added dropwise to Solution 1. The final combined solution was held for 3 hours under constant stirring and at a set temperature to promote the aging process. All of the samples generated in this work were held at about 75°C. The resulting HA precipitates were collected by filtration and washed with deionized water until the filtrate became neutral. The collected HA was dried at 90°C for 12-16 hours and ground manually into powder. For fast titration rates (>20 mL/min) a separatory funnel was utilized. For titrations from 5-15 mL/min, capillary tubing was used. The tubing was inserted into the mouth of the separatory funnel and secured in place with Teflon tape. Finally, a low speed peristaltic pump was used to achieve flow rates from 0.66 to 2.5 mL/min.

*2.2.3 Characterization of Synthesized HA*

Namely, field emission scanning electron microscopy (FESEM) and x-ray diffraction (XRD) were used to characterize the morphology and crystal structure of the HA samples. A JEOL JSM 6335F field emission scanning electron microscope (FESEM) was used to examine the morphology of sputter coated powder samples with an accelerating voltage of 10 kV. Sample powders were dispersed in ethanol and sonicated for 20 minutes to reduce agglomeration before being collected on copper microscopy grids. Samples were then sputter coated with gold palladium for 1 minute prior to imaging. The micrographs were analyzed using ImageJ to quantitatively determine particle size and aspect ratio. Particle size measurements are presented as averages, where n=50. FESEM micrographs were also used to qualitatively determine particle shape.

Powder samples were examined using a Bruker D2 Phaser X-ray diffractometer with a copper target, and voltage and current conditions of 40 kV and 40 mA, respectively. Conditions used were a 0.02° 2-theta step size and a scan speed of 4°/min with a 2-theta range of 10-90°. Resulting XRD spectra were compared to HA reference pattern, JCPDS card number 9-432, as well as each other.

*2.3 Results and Discussion*

HA particle morphology for varying titration rates is summarized in Table 2.1. A clear trend emerges when comparing both particle size and particle aspect ratio with titration rate. An increase in titration rate leads to a decrease in both size and aspect ratio. For the titration rates tested, the largest particles and highest aspect ratios were produced with a 0.80 mL/min titration

rate (255 nm length, 4.7 aspect ratio). The smallest particles were produced at a titration rate of 140 mL/min (27 nm diameter).

**Table 2.1** Particle morphology measurements for varying titration rates

| Titration speed (mL/min) | Particle Shape | Avg. Length (nm) | Min. Length (nm) | Max. Length (nm) | Stdv. | Avg. Aspect Ratio | Min. Aspect Ratio | Max. Aspect Ratio | Stdv. |
|---|---|---|---|---|---|---|---|---|---|
| 0.80 | Rod | 255 | 75 | 529 | 98.732 | 4.7 | 1.8 | 9.0 | 1.568 |
| 1.66 | Rod | 171 | 42 | 355 | 71.389 | 3.9 | 1.5 | 6.9 | 1.317 |
| 2.33 | Rod | 192 | 59 | 445 | 90.056 | 3.7 | 1.7 | 9.9 | 1.816 |
| 5.60 | Rod | 123 | 38 | 250 | 43.878 | 3.0 | 1.0 | 6.2 | 1.068 |
| 14.0 | Rod | 103 | 42 | 185 | 35.809 | 2.2 | 1.1 | 4.4 | 0.724 |
| 23.3 | Sphere | 50 | 12 | 103 | 23.503 | 1 | - | - | - |
| 35.0 | Sphere | 36 | 6 | 84 | 16.064 | 1 | - | - | - |
| 140 | Sphere | 27 | 11 | 59 | 10.624 | 1 | - | - | - |

An increase from 1.66 to 2.33 mL/min did result in a slight increase in average particle size from 171 to 192 nm, however, this is likely the result of a few outlying particles in the 2.33 mL/min batch which were unusually large, as indicated by the difference in maximum length values (355 nm compared to 445 nm). This hypothesis is supported by the fact that the 2.33 mL/min group has the particle with the single highest aspect ratio measured (9.9, as compared to 9.0 for the 0.8 mL/min batch), but the third-highest average aspect ratio, in accordance with it being the third slowest titration rate. The aspect ratio decreased with increasing titration rate for all sample groups. An ANOVA F-test analysis was conducted on the mean length values for each of the titration rates considered. This analysis resulted in an F-value of 33.4 compared to an $F_{crit}$-value of 2.4, thus verifying that titration rate does affect particle size over the range of titration rates considered in this study.

All titration rates above 20 mL/min (23.33, 35, 140 mL/min) resulted in spherical shaped particles with aspect ratios of about 1. Slower titration rates resulted in needle- or rod-shaped particles. For spherical shaped sample groups the aspect ratio is assumed to be about 1 for all particles and only diameter, not length and width, measurements were made. As a result, no minimum or maximum aspect ratio values are reported for these groups. ANOVA F-test analysis was also conducted on aspect ratios for titration speeds of 0.08 mL/min to 14.0 mL/min (rod-shaped particles) and it was verified that titration rate does have a statistically significant effect on aspect ratio ($F=24.0$, $F_{crit}=2.41$).

Representative FESEM images for samples with the slowest (0.80 mL/min) and fastest (140 mL/min) reactant addition rates are shown in Fig. 2.1. The difference between particle morphologies of the two samples is clear. The sample generated with a slow reactant addition consists of distinctly rod-shaped particles with a defined aspect ratio. The samples generated with a fast titration rate, on the other hand, are spherical and considerably smaller than the 0.80 mL/min sample particles. There is also a higher degree of agglomeration in the 140 mL/min sample particles, and in fact individual spherical particles can be hard to locate due to their extremely small size.

Faster reactant addition rates result in smaller HA particles due to greater amounts of local supersaturation. Crystallization is driven by the thermodynamics and kinetics of a system. When crystallization occurs in solution, the smallest possible particle size (critical size) is limited to the size at which the surface free energy of the particle is greater than the energy of the solution (Gibb's Thompson effect). Below the critical size the crystal nucleus is unstable and re-dissolves. In cases of local supersaturation, nucleation and growth occur simultaneously. A larger supersaturation, such as increasing the reactant addition rate, can reduce the critical

particle size and therefore increase the probability of nucleation compared to the probability of crystal growth. This mechanism explains why faster reactant addition rates yielded smaller size HA particles in the system tested.

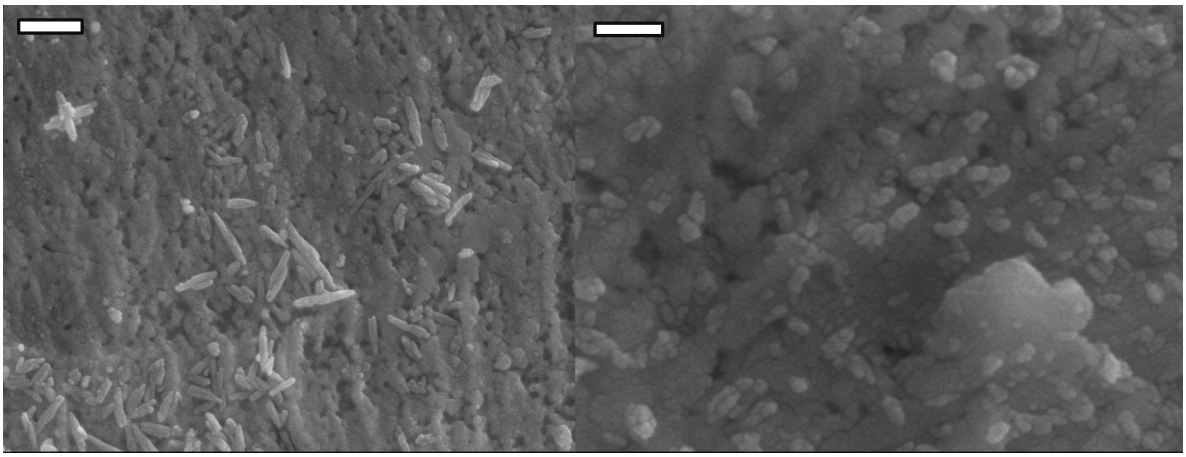

**Figure 2.1** FESEM micrographs of HA prepared using 0.8 mL/min. reactant addition rate (left) and 140 mL/min reactant addition rate (right). Note, the scale bar for 0.8mL/min is 500 nm, and the scale bar for 140 mL/min is 200 nm.

In addition to FESEM, XRD was employed to study the purity and crystal structure of the HA. In this study, the synthesized HA matched the reference peaks well at all reactant addition rates. This indicates that the titration rate does not affect the purity of the HA created, and is therefore a reliable method for HA morphology control. XRD spectra for several HA samples are shown in Fig. 2.2. With the fastest reactant addition rate, there is an apparent decrease in peak intensity and corresponding peak broadening. This can be attributed to a decreased HA crystallinity and local inhomogeneity from rapid addition of the phosphate containing solution into the calcium containing solution, as well as a particle size effect.

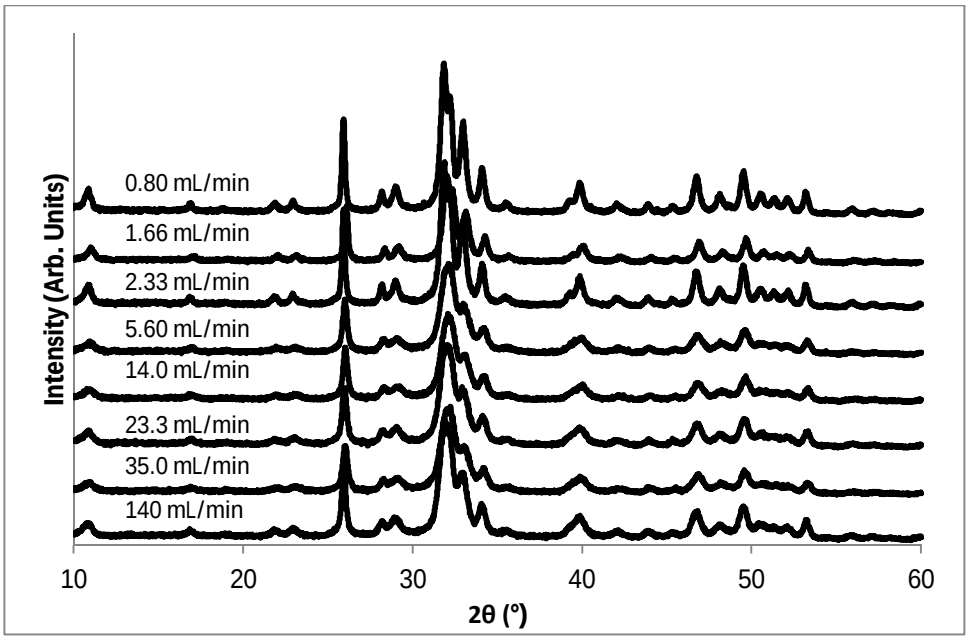


**Figure 2.2** XRD spectra for HA generated using various reactant addition rates ranging from 0.08 mL/min. to 140 mL/min.

*2.4. Conclusions*

By changing variables in a controlled manner, the effect of a single variable on the aspect ratio and size of HA particles generated via wet synthesis can be determined. In this study the variable examined was reactant addition rate, and it was found that as reactant addition rate decreases, particle size and aspect ratio increase. Furthermore, it was shown that the morphology could be tailored in such a way without generating additional calcium phosphate crystal phases. Thus, controlling reactant addition rate is a practical approach to control HA morphology allowing HA particle characteristics to be tailored to a specific application.

# Chapter 3

## Synthesis and Characterization of Iron Substituted Hydroxyapatite via a Simple Ion-Exchange Procedure

### *3.1. Introduction*

Bone fracture and bone related disorders are increasing in prevalence, largely due to an aging global population [87-89]. As a result, demand has increased for improved techniques and materials for bone repair and regeneration. Bone serves as the structural support system for the body and is a composite material with a complex hierarchical structure. The basic building block of natural bone is the mineralized collagen fibril, with the main mineral phase being hydroxyapatite (HA) [1, 2]. Due to its biocompatibility and bioactivity, synthetic HA is well suited to bone related biomedical applications [5].

HA, $Ca_{10}(PO_4)_6(OH)_2$, is a hexagonal material, from space group $P6_3/m$ [90]. A wide variety of substitutions can be made into the HA lattice by large number of anions, cations, and functional groups with examples including, but not limited to, $F^-$ [46, 47], $Fe^{2+/3+}$ [62-67], and $CO_3^{2-}$ [48]. The wide variety of these possible substitutions can be attributed to the fact that the apatite structure is both flexible and highly stable [44]. In the case of cationic metal ions, such as iron, there are two distinct calcium sites in the HA lattice where substitutions can occur [62]. Iron as a substituted cation may be of interest in bone related applications due to the fact it is present naturally in trace amounts in both teeth and bone [63]. Additionally, its presence provides iron substituted apatite (FeHA) with paramagnetic properties that can be applied clinical uses other than bone repair, such as drug delivery, medical imaging, or hyperthermia based cancer therapies [64, 68-72].

All previous aqueous iron substitutions in HA have been done during apatite synthesis or via controlled temperature and pH ion-exchange [62, 64-67, 56]. In these studies, iron was incorporated into hydroxyapatite during wet synthesis procedures, in which iron containing solutions were mixed with calcium and phosphate containing solutions at controlled temperatures and pH values. These values ranged from temperatures of 37°C [66] to 95°C [67], and pH values ranging from 8.5 [64] to 9.4 [66]. In addition, Li et al. incorporated iron into their apatite powders by employing an ion-exchange during the aging step of the wet synthesis process [56]. The pH and temperature were both well controlled and samples were aged for 2 hours at 98.5°C and an additional 24 hours of aging at room temperature. These procedures all resulted in a pure apatite crystal structure in the resulting as dried powder. A change to a hematite phase ($Fe_2O_3$) was observed after sintering at 1150°C by Morrisey et al. [65]. In cases where magnetic properties were examined, all resulting powders also showed a change from the diamagnetic properties of pure HA to para- or superpara-magnetic properties for iron incorporated HA [56, 64, 67]. Despite the success achieved by earlier studies, the objective of this work in this chapter was to achieve iron-substituted hydroxyapatite with magnetic properties using a simple and efficient procedure. The procedure discussed in this chapter is a room temperature ion-exchange effective with soaking times as short as 1 hour.

## *3.2 Materials and Methods*

### *3.2.1 Synthesis of Hydroxyapatite Powder*

Hydroxyapatite powder was prepared via a wet precipitation method based on previous work done by Kothapelli et al. [48]. Briefly, a volume of 200 mL ammonium phosphate (99+%, Acros) 2 g/dL aqueous solution was added dropwise at a moderate dropping rate under vigorous

stirring to 600 mL of an aqueous calcium nitrate tetrahydrate (99%, Fisher) solution of the same concentration at 75°C. An 80 mL volume of ammonium hydroxide (~30%, Fisher) was also added to the mixed solution to bring up the pH to 11-12. After 3 hours of stirring at 75°C, the HA particles were collected by filtration and washed thoroughly with deionized water. The collected HA precipitates were vacuum dried for 48 hours at room temperature and ground by mortar and pestle into a fine powder.

*3.2.2 Ion Substitution*

HA powder was subjected to a simple soaking procedure to achieve iron substitution for calcium in the HA crystal lattice. Initial tests were conducted using two distinct iron containing solutions: one was a dilute ferric chloride solution (40% w/v, Fisher) and the other was a dilute ferrous chloride solution (99%, Acros) in deionized water. Each solution had an iron concentration of 0.01 M. HA powder was soaked in the iron solutions, at an amount of 200 mL of solution per gram of HA, under moderate stirring for one hour, and then collected by filtration and washed thoroughly by deionized water. The powder was dried overnight and ground by mortar and pestle.

After initial EDX and magnetic characterizations to check for iron content in the resultant sample powders, further experiments were conducted using the ferric ($Fe^{3+}$) solution. HA was soaked in ferric solution under moderate stirring at room temperature for various lengths of time ranging from 1 hour to 24 hours, then collected, washed, dried and ground.

### *3.2.3 EDX Characterization*

An EDAX CDU/SUTW Leap Detector coupled to Philips ESEM 2020 was used to verify the presence of iron in the sample powders as well as qualitatively assess the effect that the ion-exchange procedure had on the Ca:P ratio of the powders. Sample powders were pressed onto carbon tape and affixed to sample holders for insertion into the microscope.

### *3.2.4 FESEM Characterization*

A JEOL JSM 6335F field emission scanning electron microscope (FESEM) was used to examine the morphology of sputter coated powder samples with an accelerating voltage of 10 kV. Sample powders were dispersed in ethanol and sonicated for 20 minutes to reduce agglomeration before being collected on copper microscopy grids. Samples were then sputter coated with gold palladium for 1 minute prior to imaging.

### *3.2.5 XRD Characterization*

A Bruker AXS D5005 X-ray diffractometer with a copper target, and voltage and current conditions of 40 kV and 40 mA, respectively, was used to examine the crystal structure of the FeHA powder samples. Conditions used were a 0.02° 2-theta step size and a scan speed of 1°/minute with a 2-theta range of 10-60 for broad-range XRD patterns, and 31.5-32° for short-range patterns.

### *3.2.6 FT-IR Characterization*

A Niclotet Magna 560 Fourier transform infrared spectrometer was used to compare the functional groups of pure HA and the FeHA samples. This characterization was carried out

using classic KBr pellet technique in transmission mode. Each FT-IR spectrum was an average of 32 scans with a resolution of 4.0 $cm^{-1}$ in the range 400-4000 $cm^{-1}$.

*3.2.7 VSM Characterization*

A vibrating sample magnetometer (VSM, connected with the Evercool Physical Properties Measurement System from Quantum Design) was used to measure magnetization at room temperature in a magnetic field range of 0-15 kOe.

*3.2.8 ICP-AES Characterization*

The elemental analyses of the materials were carried out by inductively coupled plasma atomic emission spectroscopy (ICP-AES, Thermo Jarrell Ash) using an ICAP 61E Trace Analyzer instrument. ICP-AES was calibrated by standard solutions for iron and the sample solutions were prepared by dissolving 25 mg of powder in 0.01 volume % HCl in DIW.

*3.2.9 EPR Characterization*

Electron paramagnetic resonance experiments were performed on a Bruker EMX X-band spectrometer at a temperature T = 100 K. Samples were loaded into quartz tubes and evacuated for 30 minutes prior to analysis.

*3.2.10 XPS Characterization*

A PHI Multiprobe with an X-ray photoelectron spectrometer was used to measure the binding energies in the FeHA powder. A 1 eV step size was used for survey experiments and 0.1 eV step size for higher resolution experiments focusing on iron peaks only. The hydrocarbon

peak in the C1s spectra was set to 284.6 eV as a reference for the binding energy scale for the samples.

*3.2.11 Degradation Study*

FeHA powder (1-hour soaking time), as well as HA, was uniaxially pressed into pellets using a bench top laboratory press (Carver Model C). For each pellet, 0.25 g of powder was pressed into a 13 mm pellet die well lubricated with stearic acid (97%, Acros) in acetone (99.9%, J.T. Baker) at a pressure of 100 MPa for 10 seconds. Un-sintered pellets were subjected to a dynamic (shaking) degradation study in 0.9% NaCl solution at 37°C and 50 rpm. The starting pH of the saline solution was 6.2.

For each powder type, 3 pellets were examined at each time point, 1 day, 1 week, 2 weeks, 3 weeks, and 4 weeks. The saline was collected and separated from the pellet for each time point using a pipette and placed into clean vials, and pH was measured using a pH meter (Accumet XL15 pH meter). The concentration of iron in the saline solution for each time point was measured using atomic absorption spectrometry (AAS) (Perkin-Elmer, 3100 AAS).

*3.2.12 TEM Sample Preparation*

FeHA powder samples were also subjected to transmission electron microscopy (TEM) observations. As the size of HA particles produced by the wet synthesis approach is at the nanometer level, it is difficult to study iron distribution within a single HA particle. As such, HA was synthesized using a urea decomposition procedure, which produces HA particles in the tens of micrometers range. A solution containing 7.88 g calcium nitrate in 200 DIW was adjusted to pH of 2 using nitric acid. This solution was mixed with 2.64 g ammonium phosphate in 200 mL

DIW (also adjusted to pH 2 with nitric acid). Additionally, 3.12 g of urea were added to the system (Fisher, 99+%). The mixture was stirred at 60 rpm at 95°C for 48 hours. The resulting precipitate was collected via centrifugation and washed thoroughly with DIW, dried, and ground by mortar and pestle.

The resulting HA powder was then soaked in 0.01M ferric chloride solution at room temperature under moderate stirring for 1 hour. The FeHA was collected by filtration and washed thoroughly by deionized water. The powder was dried overnight and ground by mortar and pestle.

### *3.2.13 TEM EDX Line Scan Characterization*

FeHA powder synthesized as described in the above section was dispersed on copper TEM grids. A Tecnai T12 S/TEM equipped with an EDAX EDX system was then used, with drift correction, to obtain line scans of iron content across FeHA particles to examine iron distribution in a single HA particle.

## *3.3 Results*

### *3.3.1 EDX Analysis of the Presence of Iron in the Soaked Powders*

EDX patterns were collected for pure HA, HA soaked in ferrous chloride, and HA soaked in ferric chloride. These spectra are shown in Fig. 3.1. Iron is present in a significant amount in the ferric chloride soaked HA sample (as shown in Fig. 1 c), but not in the ferrous chloride soaked sample (Fig. 1 b). There is no iron present in the pure HA control (Fig.1 a), as expected. In addition, the Ca:P ratios in the control HA and the ferrous chloride soaked HA samples are comparable, with Ca:P being greater than 1 (approximately 1.7 in each case), but the Ca:P ratio

in the ferric chloride soaked sample (FeHA) is greatly decreased. In the ferric chloride soaked HA, Ca:P is approximately 0.4, or in other words there is more P present in the powder than Ca. There is a small amount of iron present in the ferrous chloride soaked sample, as well as small amounts of chlorine present in both soaked samples. Additionally, there are carbon peaks of varying intensity in each of the EDX spectrum from the carbon tape used to fix the powders in place.

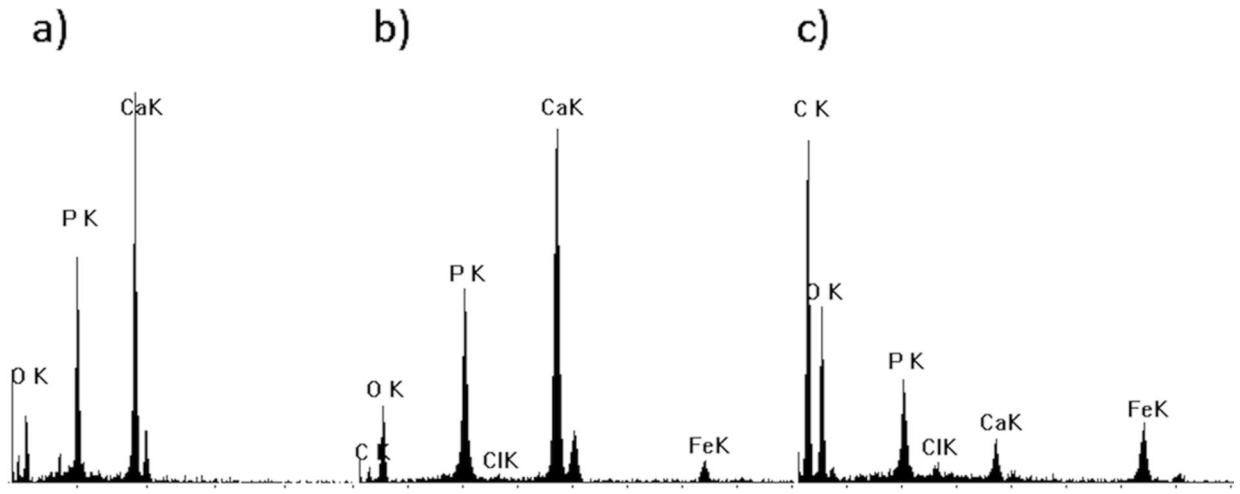


**Figure 3.1** EDX results for (a) pure HA, (b) samples soaked in ferrous chloride solution, and (c) samples soaked in ferric chloride solution.

*3.3.2 FESEM Analysis of Powder Morphology.*

Morphologies of pure HA and HA powder immersed in $FeCl_3$ for 1, 12 and 24 h are shown in Fig. 3.2. It was observed that the pure HA starting particles have a rod-like morphology with a length in the range 100-300 nm. The FeHA particles inherited a similar morphology and size from the pure HA particles. It seems that the soaking time does not have significant impact

on the resulting morphology of FeHA particles. All nanoparticles, pure HA and FeHA, are agglomerated even after sonication.

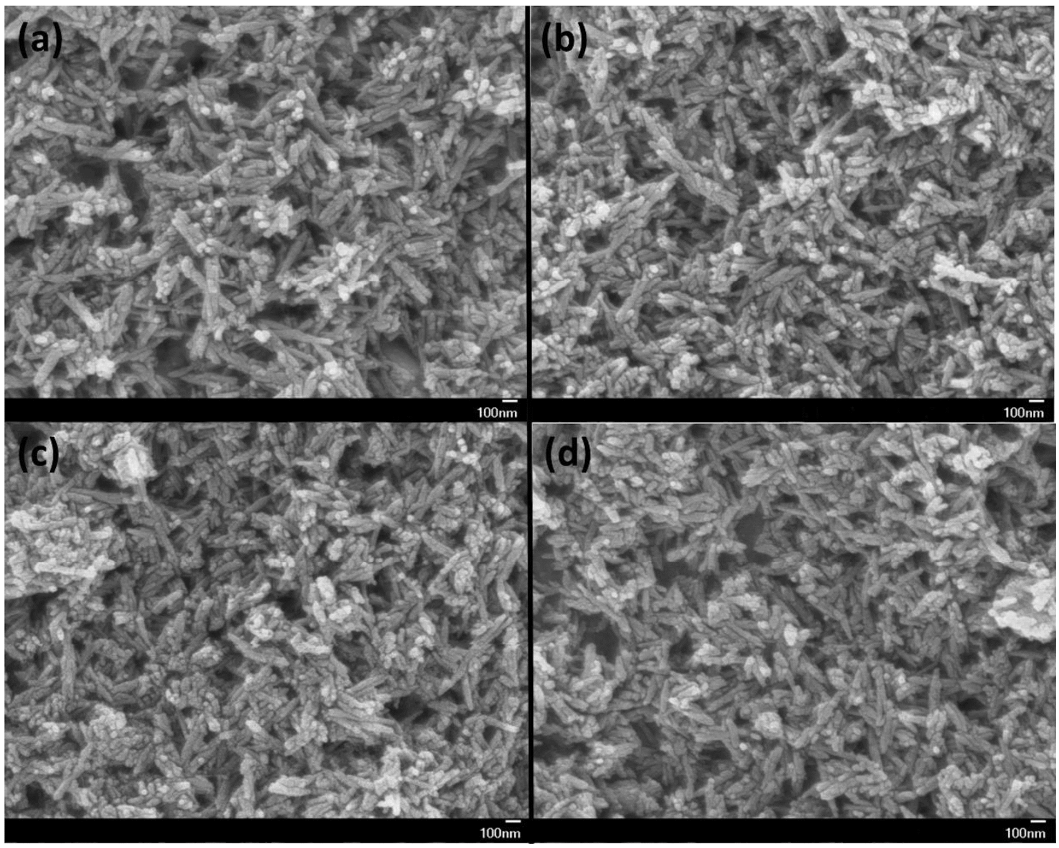


**Figure 3.2** FESEM micrographs of (a) HA, (b) FeHA with 1 hour soaking time, (c) FeHA with 12 hour soaking time, and (d) FeHA with 24 hour soaking time powders.

*3.3.3 XRD Analysis*

The XRD patterns of synthesized HA and FeHA (1, 12, and 24 hour soaking times) from 10-60° 2θ are shown in Fig. 3.3. All patterns are in agreement with the hexagonal HA reference pattern, JCPDS card number 9-432. No notable diffraction peaks appeared other than those attributed to HA. Additionally, no obvious changes in relative peak intensities between the various apatite peaks after ion exchange were observed. The pure HA starting powder is not

highly crystalline, due to the fact the powder was not calcined, and although the apatite crystal structure was maintained without any second phase detected, the FeHA sample showed peak broadening and decrease in intensity. This can be due to poor FeHA crystallinity as compared to HA.

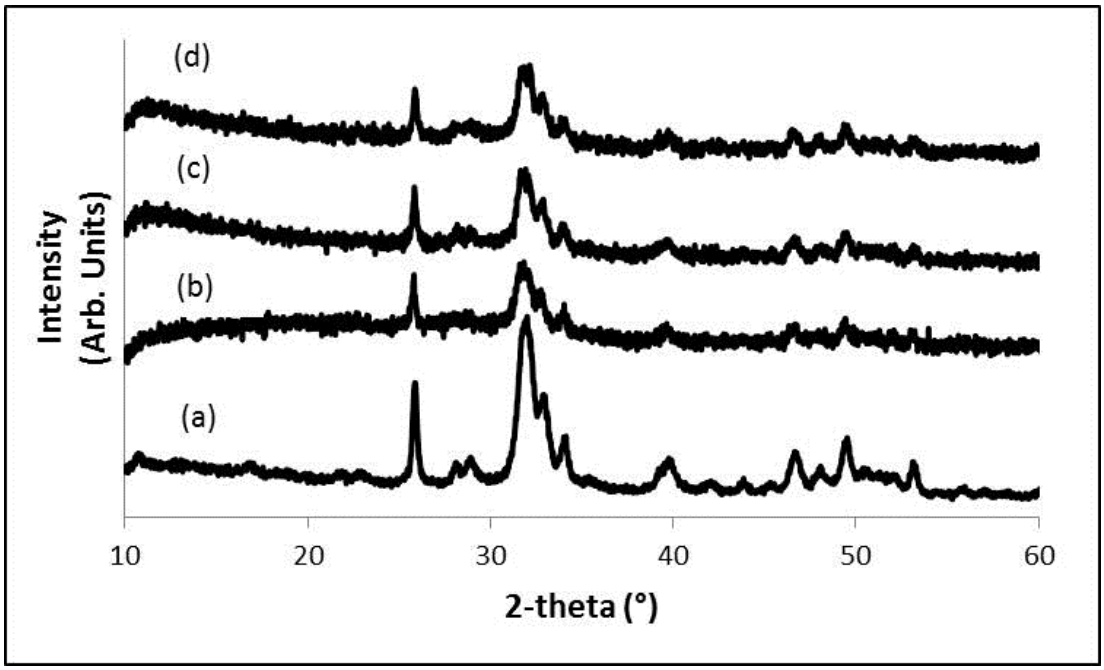


**Figure 3.3** XRD diffraction patterns of (a) HA synthesized by a wet precipitation method and FeHA obtained via (b) a 1-hour simple soaking procedure, (c) 12 hour simple soaking proceduring, and (d) 24 hour simple soaking procedure.

A short-range XRD study from 31.5-32° 2θ of the (211) peak that occurs at 31.8°, was conducted as a function of FeHA soaking time. These results are shown in Fig.3.4. With an increase in soaking time there is a drastic decrease in peak intensity, as well as a peak broadening, and a slight peak shift left.

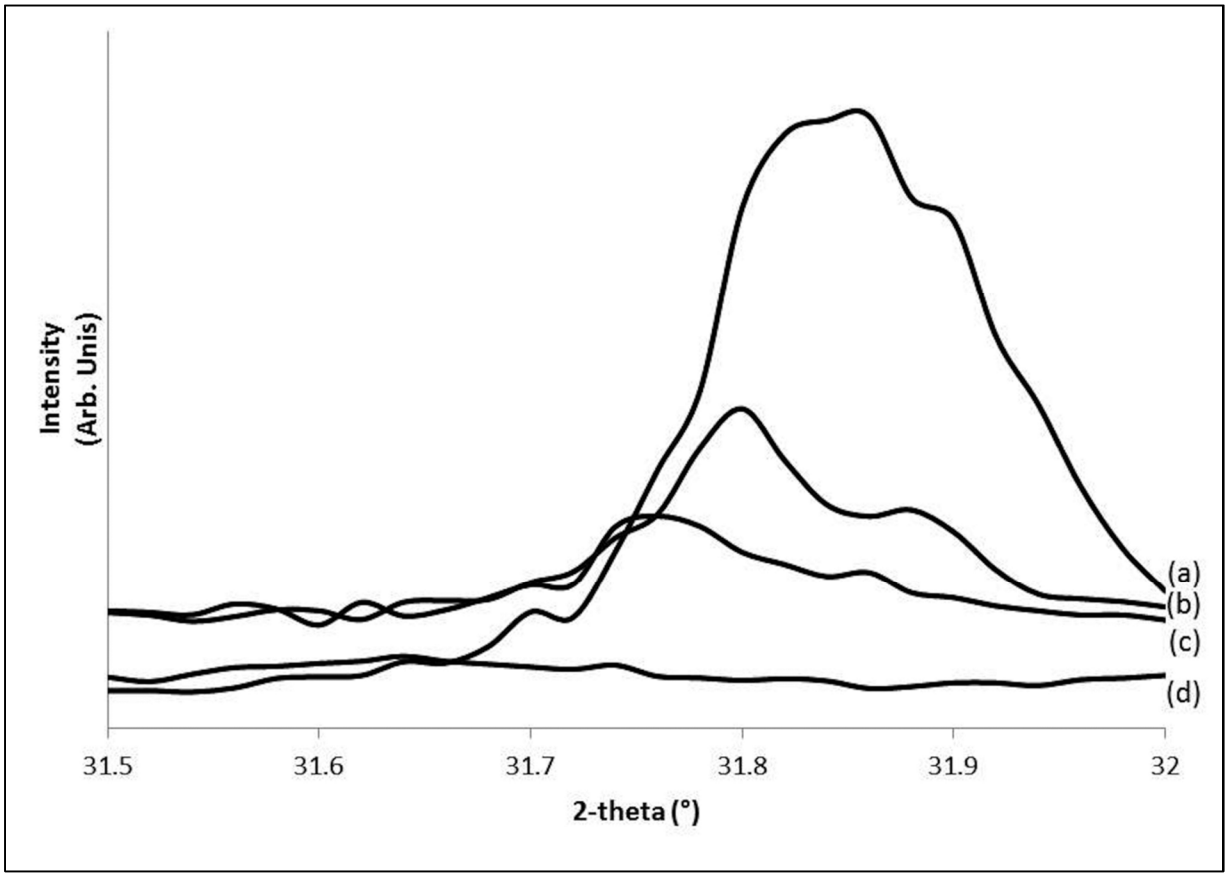


**Figure 3.4** Short angle range XRD patterns for (a) HA, (b) FeHA with 1 hour soaking, (c) FeHA with 4 hour soaking, and (d) FeHA with 24 hour soaking.

*3.3.4 FT-IR Analysis of the Molecular Structure of HA and FeHA*

Fourier transform infrared spectroscopy was conducted on pure HA control powder, as well as FeHA sample powders with 1, 12, and 24 hour soaking times. The FT-IR spectra, in Fig. 3.5, show that there is no significant difference between the HA and the FeHA samples. Each peak can be assigned to a characteristic peak of hydroxyapatite. Peaks between 660-520 $cm^{-1}$ as well as around 1040 $cm^{-1}$ can be attributed to phosphate groups. There are carbonate peaks between 1650-1300 $cm^{-1}$, and also an obvious hydroxyl bending mode around 3570 $cm^{-1}$. There are no peaks appearing in the FeHA sample spectra that cannot be identified as peaks

corresponding to functional groups found in pure HA. This further indicates that the FeHA maintained a similar structure to the pure HA. The only noticeable difference between HA and FeHA spectra is an increase in the hydroxyl peak at 3570 $cm^{-1}$.

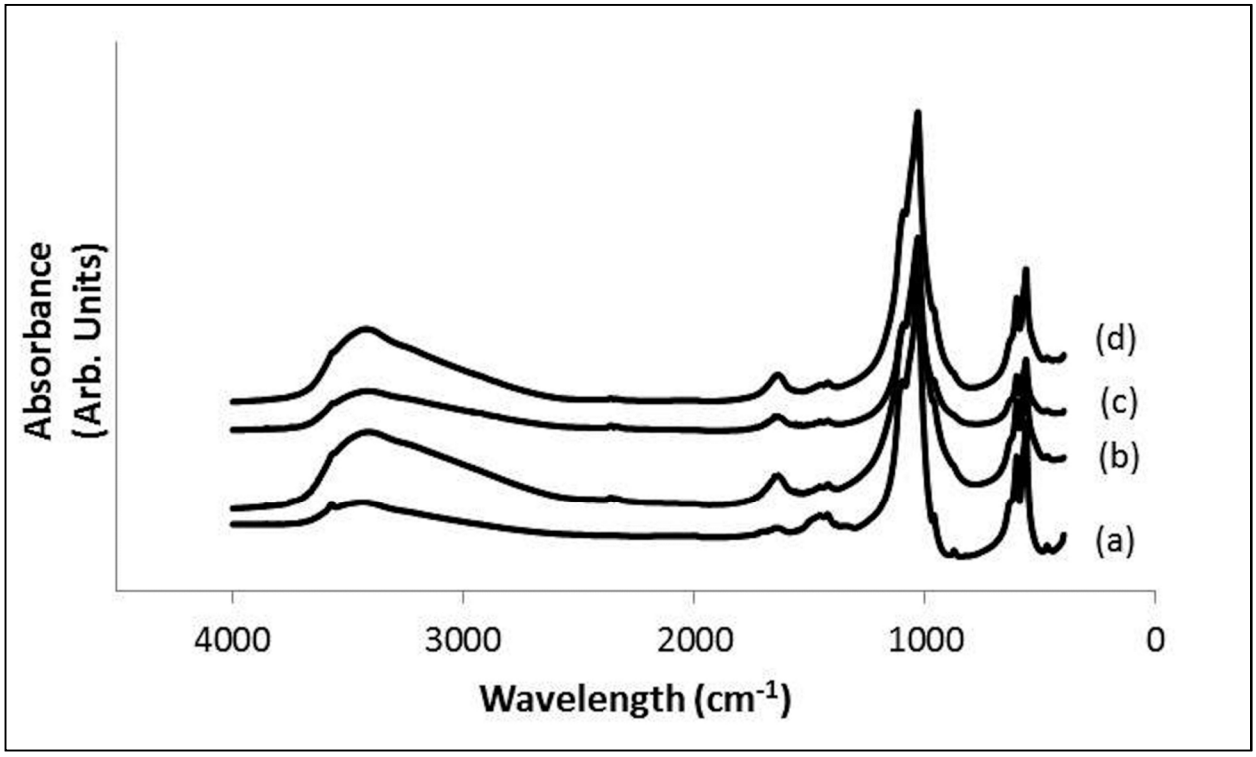


**Figure 3.5** FT-IR spectra of (a) HA, (b) FeHA with 1 hour soaking, (c) FeHA with 4 hour soaking, and (d) FeHA with 24 hour soaking.

*3.3.5 Magnetic Properties of FeHA by VSM Analysis*

VSM was used to measure the magnetization of HA, and both ferric and ferrous chloride soaked HA at room temperature in a 10 kOe field, as shown in Fig. 3.6. Both pure HA and HA soaked in ferrous chloride were shown to have diamagnetic properties by the negative slope of the magnetization-magnetic field curve. In the case of HA soaked in ferric chloride, the positive slope indicated paramagnetic properties of the powder.

Additionally, VSM measurements on FeHA at various soaking times were examined, and a selection of them is shown in Fig. 3.6. All samples soaked in ferric chloride showed paramagnetic properties. The FeHA samples whose magnetization curves are plotted in Figure 6 are representative of the magnetization behavior of ten distinct FeHA samples that were measured. Although all samples showed that iron substitution led to magnetic properties, there was no apparent pattern between soaking time and magnetic properties.

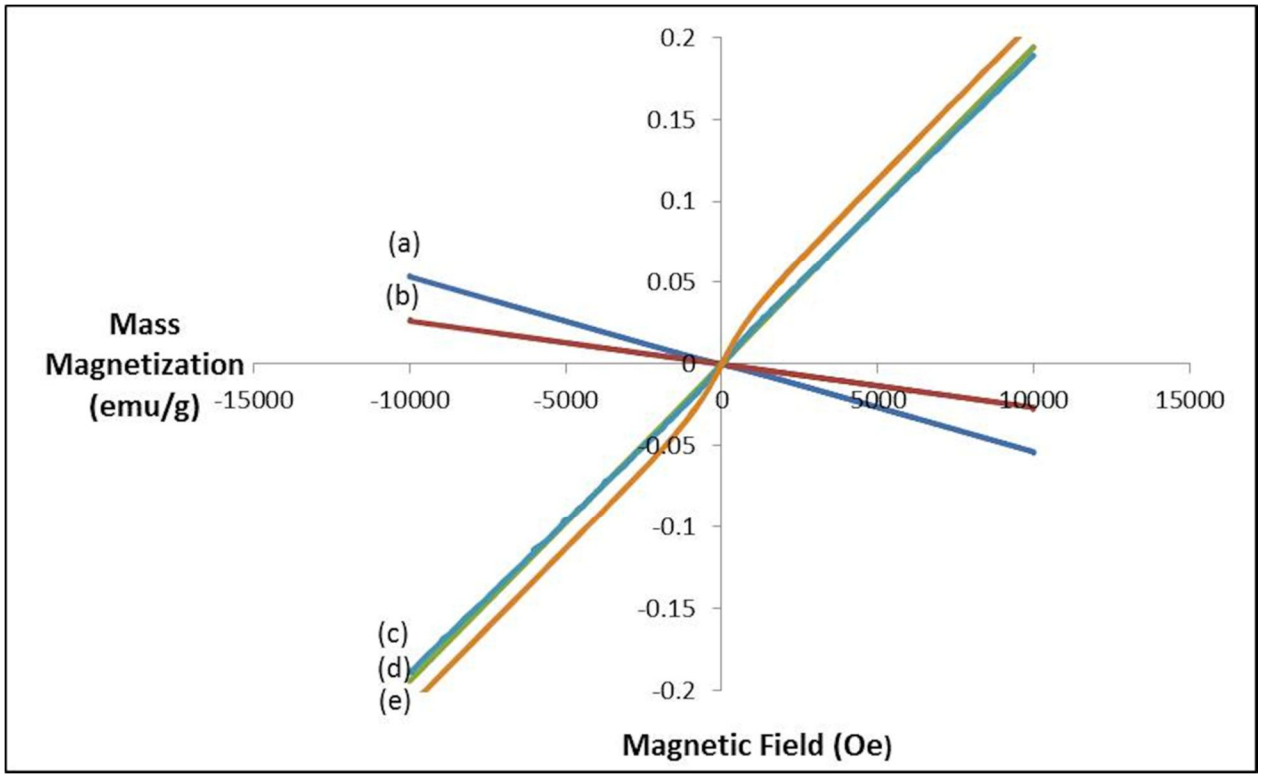


**Figure 3.6** Room temperature mass magnetization measurements of (a) HA, (b) ferrous chloride soaked HA, (c) 1 hour ferric chloride soaked HA (FeHA with 1 hour soaking), (d) FeHA with 12 hour soaking, and (e) FeHA with 24 hour soaking.

*3.3.6 Iron Quantification of FeHA by ICP-AES*

ICP was used to measure the concentration of iron in FeHA samples from 1 to 24 hours soaking time. In terms of concentration, iron content generally increased with increased soaking time. Results are summarized in Table 3.1. The iron concentration is expressed as g Fe/ g FeHA (total powder). For 1 hour soaking time, there are 0.064 g Fe/g FeHA. This number increased to 0.096 for 4 hours soaking, 0.103 for 12 hours, and 0.114 for 24 hours soaking.

**Table 3.1** ICP iron concentration measurements as a function of FeHA soaking time

| **ICP Elemental Analysis of Iron in FeHA Samples** | |
|---|---|
| **FeHA Soaking Time** | **Iron Concentration (g Fe/ g FeHA)** |
| 1 hr | .064 |
| 4 hr | .096 |
| 12 hr | .103 |
| 24 hr | .114 |

*3.3.7 EPR Analysis of FeHA*

Electron paramagnetic resonance spectroscopy scans were run on FeHA samples soaked for 1, 12, and 24 hours. All scans were run at 100 K. Results are shown in Fig. 3.7 (presented as the first derivative of the absorption spectra), and the g value for all three samples tested was 2.00. EPR spectra are specifically related to the number of unpaired electrons as well as the local environment of the paramagnetic species, so the g value would remain the same for each sample containing iron ions in the same configuration, regardless of the amount of the iron in each sample.

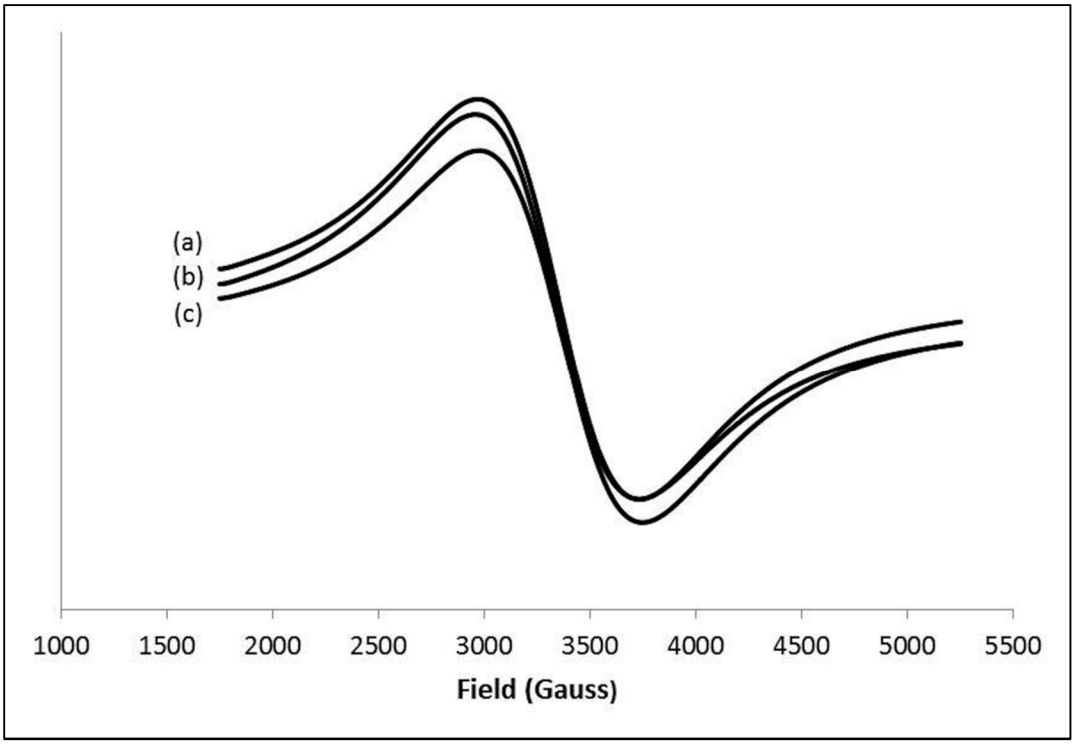


**Figure 3.7** EPR spectra for (a) FeHA 1 hour soaked sample, (b) FeHA 12 hour soaked sample, and (c) FeHA 24 hour soaked sample. g=2.00213 for all 3 spectra.

*3.3.8 XPS Characterization*

XPS was conducted on FeHA powder samples soaked for 1, 4, and 24 hours. For the 3 samples, surveys were run and the Fe/Ca ratio increased with soaking time, but the bonding remained the same. Fig. 3.8 shows high resolution spectra of FeHA powders. The binding energy for the 2p states of iron are located at 712.4 and 725.5 for Fe2p 3/2 and Fe2p 1/2 respectively for the 1 hour soaked sample (Figure 9a), 712.6 and 725.7 for the 12 hour soaked sample (Figure 9b), and 712.9 and 725.9 for the 24 hour soaked sample (Figure 9c). This corresponds to $FePO_4$ bonds, which have a 2p 3/2 binding energy of 712.8 eV, indicating that iron bonded to phosphate groups is predominant.

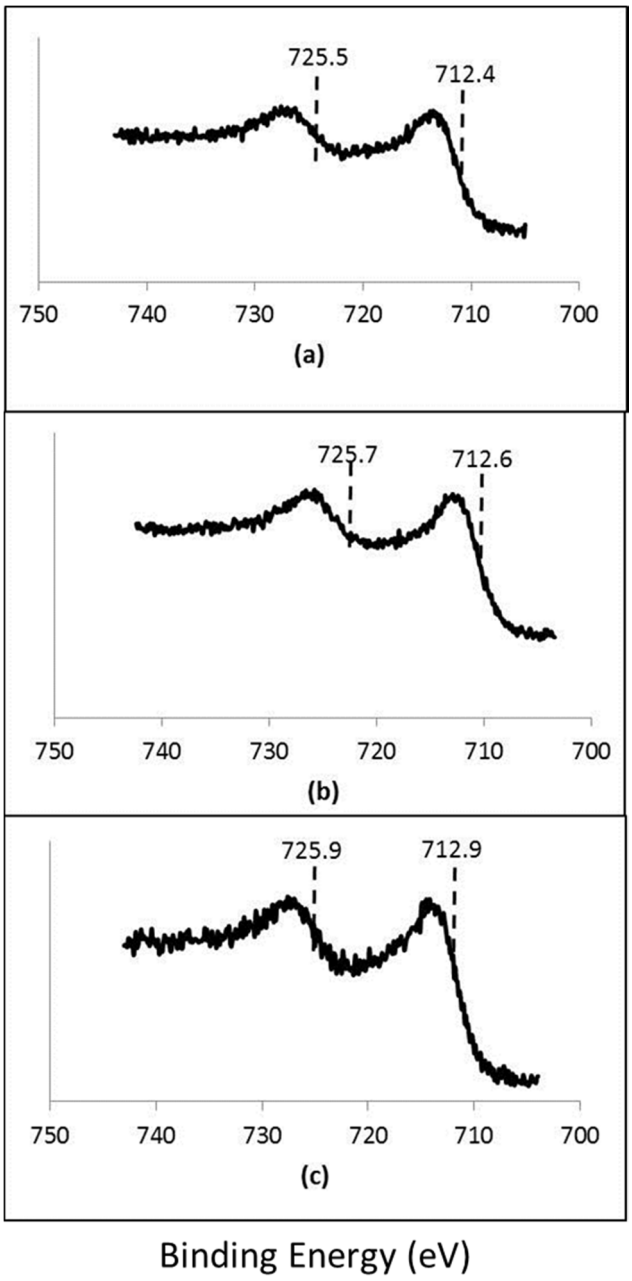


**Figure 3.8** XPS response of Fe 2p in FeHA (a) 1 hour soaked sample, (b) 12 hour soaked sample, and (c) 24 hour soaked sample.

*3.3.9 Degradation Study*

FeHA sample pellets and HA control pellets were soaked in saline solution at 37°C and 50 rpm in a shaking water bath for up to a month. Samples were removed at 1 day, 1 week, 2 weeks, 3 weeks, and 4 weeks and the remaining saline solution they had been soaking in were analyzed. The pH was measured at each time point. Fig. 3.9 is a plot of the average pH value of the soaking solution for each soaking time point.

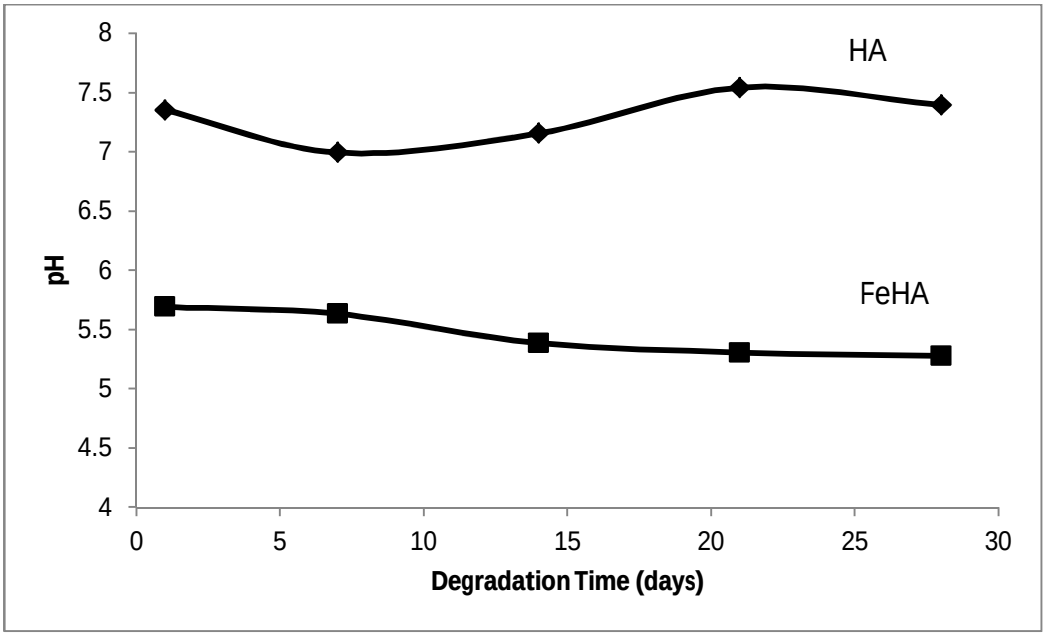


**Figure 3.9** pH as a function of pellet soaking time in a degradation study.

The pH curves for both pellet types remain relatively stable for the duration of the study. The pH of the soaking solution for HA fluctuates slightly between 7 and 7.5 from 1 day to 1 month. The pH for the FeHA soaking solution fluctuates between about 5.3 and 5.7 for the entire time period.

Iron ion concentration at each time point was measured using AAS. It was found that the concentration of free iron in solution at each time point tested was less than 0.1% of the total iron in pellet.

Visual inspection of the pellet morphology of the samples was conducted at each time point. For both sample types, pellets remained essentially intact through the 2 week soaking time point. At 3 and 4 weeks, some pellets breakage started to occur. At 3 weeks there were small pieces broken away from the HA pellets, and by 4 weeks both pellet types were breaking apart.

### *3.3.10 TEM EDX Line Scan*

FeHA synthesized by the urea decomposition method was examined using TEM due to the fact that the FeHA particles generated by wet synthesis and used in the rest of this study had dimensions that were too small to generate useful line scans in the TEM. A representative particle was imaged using TEM (Fig. 3.10a), and EDX was employed to measure iron content at a point near the particle center (point A) and a point near the particle edge (point B). The results showed about 0.2 atomic% iron at the center point, and 3 atomic% iron near the particle edge. An EDX line scan was the conducted across the particle (represented by the white line in Fig. 3.10a) and the results of the line scan (Fig. 3.10b) indicate that the levels of iron are much higher near the edges of the particle, and plateau to a much lower level near the center. Line scans were conducted on 5 particles, and the same pattern was seen repeatedly.

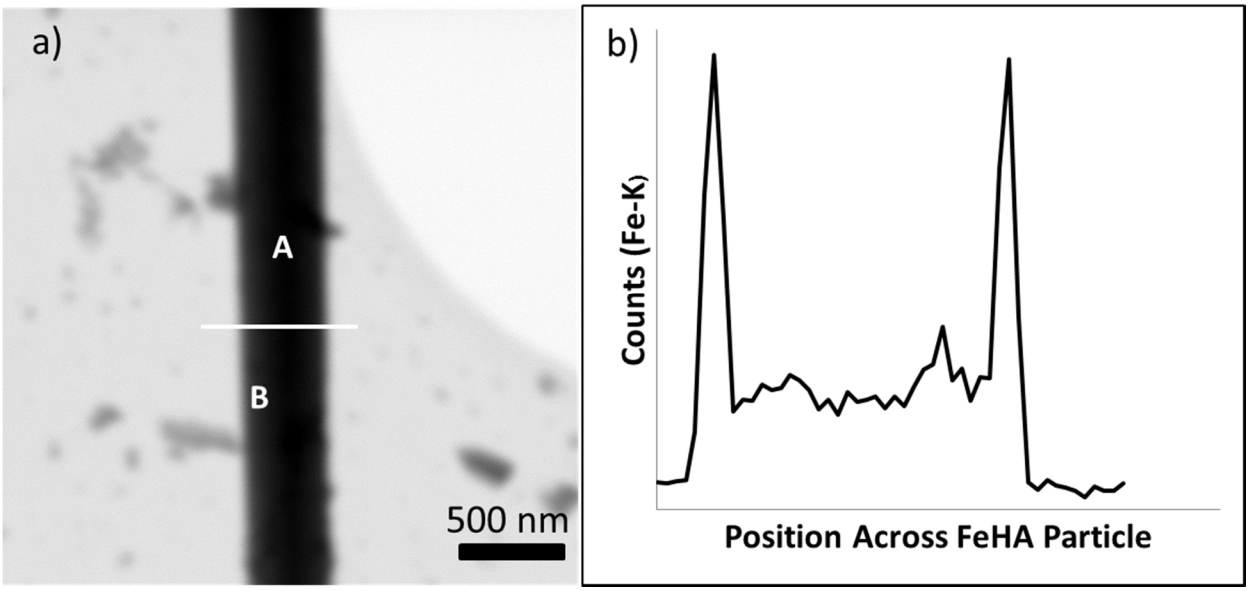


**Figure 3.10** A TEM micrograph (a) of a FeHA particle and the accompanying EDX line scan for iron (b).

*3.4 Discussion*

In this work, HA as well as FeHA were synthesized. The HA powder was white, whereas the FeHA powder samples were yellow. Based on EDX and VSM results, iron substitution occurred only in the ferric chloride soaked samples, and not in those samples soaked in ferrous chloride. This may be because at room temperature ferric ions in an aqueous environment are less thermodynamically stable than ferrous ions, and as such there would be a greater driving force for ferric ions to interact with the HA lattice than for ferrous ions. EDX showed a Ca:P ratio of less than 1 for the ferric chloride soaked powder. Stoichiometric HA has a Ca:P of 1.67, and this unusually low Ca:P ratio can likely be attributed to the fact that some of the calcium in that sample has been replaced by iron. The (Ca+Fe):P ratio of FeHA is about 1.0,

which is lower than the Ca:P ratio of the starting pure HA powder. If a one-for-one substitution was occurring between iron and calcium then the (Ca+Fe):P ratio would be expected to be equal to the starting Ca:P ratio. This observed change in ratio likely derives from the fact that a trivalent ion is replacing a divalent one. In order to compensate for this resulting lattice charge imbalance calcium vacancies may have been formed. Ferrous chloride soaked HA powder, on the other hand, maintained a similar Ca:P ratio as the pure HA control. The small amounts of iron present in the ferrous chloride soaked sample, as well as the small amounts of chlorine present in both ferrous and ferric soaked samples, can be explained by small amounts of ion adhesion to the powder surface from the aqueous iron chloride soaking solutions that was not removed by the powder rinsing step. In the case of chlorine, it is also possible that small amounts of substitution for hydroxyl groups occurred simultaneously with the iron substitutions. The carbon peaks in each of the EDX spectra are derived from the carbon tape used to affix the powders to SEM stubs. In addition to the differences in EDX spectra, the ferrous chloride soaked powder, like pure HA, had diamagnetic properties when measured using VSM, whereas the ferric chloride soaked power had paramagnetic properties. Therefore, $Fe^{3+}$ is more active in the exchange of $Ca^{2+}$ ions in the hydroxyapatite lattice than $Fe^{2+}$ at room temperature.

The goal of this study was to achieve a single-phase material after substitution without any formation of impurities or a second phase. Single phase is desirable because phase purity influences the bioactivity, solubility, and *in vivo* behavior of bioceramics [91].

A single-phase substituted powder was achieved, as demonstrated by the fact that no obvious differences were observed between HA and FeHA in either XRD or FT-IR data, shown in Figure 3 and Figure 5, respectively. A formation of a second phase would have resulted in extraneous peaks in both of these analysis types. However, XRD data did show broadened

diffraction patterns in FeHA as compared to HA (Fig. 3.4). This can be attributed to the fact that FeHA is more amorphous than HA. The increase of the amorphous character of the iron-substituted apatite in our study corresponds to results reported by Wang et al. [63] and Li et al. [56]. There was also a slight (211) peak shift left with increasing iron content, apparent in Fig. 4, indicating a change in lattice parameters when calcium is replaced by iron This lattice parameter distortion can be explained by the difference in radius between $Fe^{3+}$ ions (0.64 Å) and $Ca^{2+}$ ions (0.99 Å). This peak shift phenomena was also observed by Wang et al. [63]. Wang et al. reported not only a peak shift left, but also an increase in that shift with increasing iron content. This similar difference in our XRD data with an increase in soaking time suggests an increase in iron content in the powder. This idea of an increase in iron content was supported quantitatively by results of ICP measurements.

As with XRD, FT-IR similarly indicates that no second phase was formed, indicating the iron was incorporated into the system, and there was no significant change to the apatite structure. These results indicating that the HA crystal structure was maintained and no secondary iron containing phases were formed compare favorably with those observed by other groups working on iron substituted hydroxyapatites. For example, Li et al. replaced $Ca^{2+}$ with $Fe^{3+}$ ions in hydroxyapatite up to 20 wt%, which is significantly greater than the substitution amount we achieved (about 11 wt%), without revealing a change in crystal structure or formation of secondary iron-based compounds in XRD patterns [56].

Although FT-IR and XRD results provided information about crystal structure and phase purity, they do not help determine how and where the iron substitution occurs in the lattice. For this, EPR analysis was conducted to clarify the situation. EPR scans were run at 100 K, and a g value of 2.00 was obtained for each sample tested. Based on previous work done by other

groups, these results could indicate a number of iron location conditions [58, 62, 92-94]. EPR results related to $Fe^{3+}$ where g≈2 have been attributed to iron in cation-exchange sites (g=2.0), surface iron attachment (g=2.05), iron in bulk octahedral or tetrahedral sites (g≈2), iron attachment to the lattice in an iron-oxyhydroxide (FeOOH) phase (g=2.01), and iron present in hematite nanoparticles (g=2.1). In cases where g≈2 is attributed to a separate hematite phase, not only is the g value 2.1 as opposed to 2.0, but a hematite phase is readily identified in XRD [93]; therefore, we can eliminate the possibility that our material includes a hematite second phase. Iron present in the bulk apatite framework can be indicated by a g value of about 2, but this g value is typically also accompanied by a second peak corresponding to g=4.3 [92]. There is no g=4.3 peak in the EPR spectra from our FeHA samples, or this peak is severely suppressed, so most of the iron in our FeHA powder is not present in bulk lattice sites either. Thus, we have concluded from EPR results that of the possible locations for iron ions in our FeHA samples are iron in cation-exchange sites as well as FeOOH conjugated to the apatite lattice. When further considering XPS results that indicate iron-phosphate binding were formed in our FeHA, combined with EDX results that demonstrate a decrease in Ca:P ratio in substituted samples compared to HA control, the majority of the iron substitution has occurred in cation-exchange sites where $Fe^{3+}$ has replaced $Ca^{2+}$.

As is indicated by EDX and ICP results, an increase in soaking time generally leads to an increase in iron content; however, the magnetic susceptibility of the FeHA powder did not increase proportionally. Since a similar magnetic behavior and susceptibility was obtained for the HA soaked for 1 hour and 24 hours, one would choose one-hour-soaking at room temperature as a quick and efficient procedure to prepare FeHA with paramagnetic properties. Alternatively, increasing the initial iron concentration or raising the reaction temperature may result in

enhanced magnetic property of the resulting FeHA via a significant increase of iron content, but the effect that vigorous reaction conditions (e.g. high concentration or high temperature) might have on phase purity or crystallinity is unclear.

The degradation behavior of FeHA as compared to HA can be hypothesized to be similar. The trend of the pH curves for the soaking solution for each powder type was similar. The overall pH in the FeHA soaking solution was lower. This is likely a result of an initial iron burst release when the FeHA is initially introduced to the aqueous conditions. Direct measurement of the amount of iron released at each time point using AAS was shown to be incredibly low, below 0.1% of total iron content of the pellets for the duration of the study, despite the fact that the pellets were breaking apart by the end of 1 month of soaking. This suggests that direct measurement of iron release cannot be successfully measured using this technique. Due to the pH of the system (pH > 5, Fig. 3.9), it is likely that any iron ions would precipitate from solution as iron oxide, which are removed prior to AAS measurement. *In vivo* conditions would result in similar behavior, based on body pH.

The results from the TEM line scan provide insight into the mechanism that is occurring during ion exchange. The ion exchange procedure limits substitution to predominantly surface calcium sites. Ion exchange is a predominantly surface reaction because in aqueous conditions a hydrated layer of loosely bound mineral ions exists in HA, and these loosely bound ions can be easily exchanged [48]. In acidic conditions, the $Ca^{2+}$ ions dissociate from the apatite crystal lattice at the surface of the HA particle [46, 47], further facilitating an exchange between the $Ca^{2+}$ ions in the apatite lattice and the $Fe^{3+}$ ions in solution due to calcium-deficient HA being particularly subject to ionic substitutions [95]. Additionally, because the ion exchange procedure is diffusion driven, and it is being conducted at room temperature, there is not a high driving

force for the iron ions to penetrate into the apatite particles past the loosely bound surface layers. It is possible that increasing the soaking temperature could drive more iron into the particle, and increase the thickness of the iron substituted shell, but experiments would need to be conducted to verify this hypothesis.

### *3.5 Conclusion*

Using a ferric chloride solution and a simple soaking procedure, FeHA was prepared with no apparent formation of a second phase. This procedure was not successful when using a ferrous chloride solution. Iron is likely present in cation-exchange sites in the apatite lattice. As indicated by XRD, ICP, and EDX results, an increase in soaking time results in higher iron content. The substitution of $Fe^{3+}$ into the HA lattice results in FeHA powders with paramagnetic properties. This novel simplified room temperature soaking procedure can be applied in the future to synthesize magnetic apatite based nanoparticles for biomedical applications.

# Chapter 4

## A comparative study of the sintering behavior of pure and iron-substituted hydroxyapatite

### *4.1 Introduction*

Iron has been incorporated into the HA lattice during apatite synthesis, via controlled temperature and pH ion-exchange procedures, and via a simple room temperature ion exchange procedure with soaking time as short as 1 hour [62,64-67, 56, 97]. These procedures all resulted in powders with pure apatite crystal structure. All powders in which magnetic properties were measured also showed a change from the diamagnetism of pure HA to para- or superpara-magnetic properties for iron substituted HA [64, 67, 56, 97]. The change in magnetic properties allows for a wider range of clinical uses of HA.

Clinically, HA may be used in a variety of forms, including as a coating, as the reinforcement of a polymer-ceramic composite, and as a sintered ceramic. HA powder properties, such as crystallinity, surface area, and particle size, determine its effectiveness for specific applications. Additionally, powder properties and chemical composition affect HA sinterability [98]. During HA sintering reversible dehydroxylation occurs at all elevated temperatures yielding oxyhydroxyapatite, and occurs at a temperature generally above 1200°C [99, 100]. Sometimes, the dehydroxylation of HA can occur as low as 800°C when impurities are present in the powder [100]. During the dehydroxylation process, HA decomposes to tricalcium phosphate (TCP) and CaO. This decomposition creates strain due to volume changes associated with the formation of new phases, and lowers the mechanical integrity of the sintered body [100].

Although some systematic studies regarding the sintering behavior of substituted apatites have been conducted, such as the work done by Kim et al. [101] and Qiu et al. [102], to the best of the author's knowledge there has been little work conducted on the sintering behavior of FeHA. Wang et al. did report that iron containing HA nanoparticles calcined at temperatures well below 1000°C showed decomposition [63]. Additionally, work done by Morrissey et al. and Gross et al. [65, 66] sintered FeHA with a pure apatite structure in air at 1150°C. After sintering at this temperature β-TCP and hematite phases were present [65, 66] and the pellets displayed a brown to red color change accompanying the formation of the hematite phase [66]. The objective of the work presented in this chapter was to provide an evaluation of the biocompatibility of FeHA powder, as well as a systematic study of the sintering behavior and corresponding mechanical properties at a series of temperatures, to determine the appropriateness of FeHA for biomedical applications.

## *4.2 Materials and methods*

### *4.2.1 Hydroxyapatite and Iron-Substituted Hydroxyapatite Synthesis*

Hydroxyapatite powder was prepared via a wet precipitation procedure in which an aqueous solution of 2 g/dL ammonium phosphate (99+%, Acros) was added dropwise at a moderate dropping rate of about 75 drops per minute under vigorous stirring to a 2 g/dL aqueous calcium nitrate tetrahydrate (99%, Fisher) solution at 75°C. Ammonium hydroxide (~30%, Fisher) was also added to the mixed solution to bring up the pH to 11-12. After 3 hours of stirring at 75°C, the HA particles were collected by filtration and washed thoroughly with deionized water. The collected HA precipitates were dried at 90°C for 12-16 hours and ground

by mortar and pestle into a fine powder. This resulting powder was then milled (SPEX 8000 Mixer/Mill) for 10 minutes in a steel canister with alumina milling balls.

Iron-substituted hydroxyapatite (FeHA) was produced using a simple ion exchange procedure [97]. HA powder, prepared as described above, was soaked in dilute ferric chloride solution (40% w/v, Fisher), at a concentration of 5 g/L, under moderate stirring for one hour, and then collected by filtration and washed thoroughly by deionized water. The powder was dried overnight and ground by mortar and pestle, and then SPEX milled for 10 minutes.

### *4.2.2 Pellet Preparation and Sintering*

Milled HA and FeHA powders were uniaxially pressed into pellets using a bench top laboratory press (Carver Model C). For each pellet, 0.35 g of powder was pressed into a 13 mm pellet die well lubricated with stearic acid (97%, Acros) in acetone (99.9%, J.T. Baker) at a pressure of 150 MPa for 10 seconds. This yielded pellets with a thickness of approximately 1.63 mm for HA and 1.60 mm for FeHA.

Pellets were sintered at a selection of temperatures (900, 1000, 1100, 1200, and 1300°C for HA samples, and 600, 700, 900, 1000, and 1100°C for FeHA samples) and soaked at peak temperature for 2 hours in a chamber furnace (MXI model Z14) in air. Lower sintering temperatures were selected for the FeHA samples because initial results for samples run at the same temperatures as pure HA indicated that decomposition began for FeHA at temperature below 900°C. Samples were heated to the soaking temperature at a ramp rate of 5°C/min and allowed to cool naturally within the furnace to room temperature. A total of 10 pellets of each type of powder were sintered for each temperature point investigated.

*4.2.3 Starting Powder Characterization*

FeHA powder synthesized using the procedure described above was thoroughly characterized and reported in the previous chapter [97]. The SPEX milled pure HA and FeHA powders were also examined via a JEOL JSM 6335F field emission scanning electron microscope (FESEM) prior to pressing into pellets. Powder was dispersed in ethanol, sonicated for 20 minutes to reduce agglomeration, dried on a copper transmission electron microscopy (TEM) grid, and sputter coated with gold palladium for 1 minute prior to imaging with an accelerating voltage of 10 kV. Sintered HA and FeHA pellets were then characterized using a variety of techniques.

*4.2.4 Density and Biaxial Flexural Strength*

Density measurements were performed on green and sintered pellets using an Ohaus digital balance accurate to 1 mg and a caliper (Mitutoyo) accurate to 0.01 mm. Three diameter and three thickness measurements were taken for each pellet and the respective averages were used when calculating pellet density. A Tinius Olsen (150KS model) was used to determine the pellet biaxial flexure strength (modulus of rupture) on 13 mm diameter pellets using a 1000 N load cell at a crosshead speed of 0.01 mm/minute and a pin-on-disc test fixture set up per ASTM F 394 [103]. The modulus of rupture (MOR) was calculated based on the following equations:

$$S = -0.2387\, P(X-Y)/d^2 \qquad (1)$$

where S = maximum center tensile stress (MPa), P = total load causing fracture (N),

$$X = (1+\nu)\ln[(B/C)^2] + [(1-\nu)/2](B/C)^2, \qquad (2)$$

$$Y = (1+\nu)[1+\ln[(A/C)^2]] + (1-\nu)(A/C)^2, \qquad (3)$$

where ν = Poisson's ratio, 0.27, A = radius of support circle (mm), B = radius of loaded area or pin tip (mm), C = radius of specimen (mm), and d = specimen thickness at point of fracture (mm).

*4.2.5 XRD Characterization*

As-prepared HA and FeHA, and those sintered at different temperatures were examined for phase purity and crystal structure using a Bruker D2 Phaser X-ray diffractometer (XRD) with a copper target, and voltage and current conditions of 40 kV and 40 mA, respectively. Conditions used were a 0.02° 2-theta step size and a scan speed of 4°/min with a 2-theta range of 10-60.

*4.2.6 FESEM Characterization*

Field emission scanning electron microscopy (FESEM) was used to examine the polished surface morphology and cross-section morphology of sintered pellets with an accelerating voltage of 10 kV. To observe the surface morphology of the pellets, the samples were polished using 1200/P4000 grit sandpaper for 3 minutes at 150 rpm, and then for an additional 20 minutes at 100 rpm using polishing cloth and 1 μm diamond paste. Polished pellets were then sputter coated with gold palladium for 1 minute prior to imaging. Pellet cross-sections were left unpolished and sputter coated with gold palladium for 1 minute prior to imaging.

*4.2.7 Cell Culture Studies*

Mouse calvaria 3T3-E1 cells were used to assess the biocompatibility of iron substituted hydroxyapatite (FeHA). Cells were grown in alpha modified eagle's medium (α-MEM)

supplemented with 10 % fetal bovine serum (Cellgro, FBS) and 1 % penicillin-streptomycin under an atmosphere of 5 % $CO_2$ at 37 ºC. At 90 % confluence, cells were harvested and seeded at a density of 2 x $10^4$ cells per well in a 24 well plate. Four hours were allotted for cell attachment after which the medium was changed to medium containing particles dispersed at concentrations of 20 µg/ml or 50 µg/ml HA or FeHA. Powders were sterilized by immersion in 70 % ethanol for 30 minutes while under sonication. The powders were collected by centrifugation and rinsed with sterile filtered DIW three times and re-dispersed in supplemented α-MEM.

Cellular proliferation was assessed at 1, 3 and 7 days via alamar blue assay. In brief, cells were rinsed with phosphate buffer saline and the medium was refreshed with 1 ml of powder-free medium. Alamar blue was added at $1/10^{th}$ the medium volume and incubated at 37 ºC for 4 hours. Aliquots, 200 µl, were taken from each specimen in triplicates and the absorbance was measured at 570 and 600 nm. The percent reduction in alamar blue was calculated by:

$$\textit{Percent Reduced} = (A_{570} - R_o A_{600})*100$$

*4.3 Results*

*4.3.1 Starting Powder Characterization*

As was reported in our previous work, using a ferric chloride solution and a simple soaking procedure a phase pure FeHA material can be achieved in which iron substitutes into cation-exchange sites in the apatite crystal lattice replacing calcium ions. This material was thoroughly characterized using methods including XRD, energy dispersive X-ray spectroscopy (EDX), inductively couple plasma atomic emission spectroscopy (ICP-AES), Fourier transform infrared spectroscopy (FT-IR), and vibrating sample magnetometer (VSM) and superconductive

quantum interference device (SQUID) analysis [97]. These previous results showed that after iron substitution the powder retained characteristic apatite crystal structure and functional groups, but the iron doped samples displayed paramagnetic properties, as opposed to the diamagnetism of pure HA. The effect of soaking time on iron content was also examined, and collectively X-ray diffraction and inductively coupled plasma atomic emission spectroscopy results suggested that an increase in soaking time led to an increase in iron content in the sample powder. An increase in iron content resulted in a decrease in sample crystallinity and a decrease in crystal lattice parameters. For a 1-hour soaking, such as used in this study, there were 0.064 g Fe/g FeHA, as measured by ICP-AES [97].

In this study, the starting powder was SPEX milled, and then characterized using FESEM. The FESEM images of the SPEX milled pure HA and FeHA samples in Fig. 4.1 indicate that after SPEX milling pure HA for 10 minutes there is a wide particle size distribution ranging from about 30-300 nm length rod shaped particles. After ion exchange and an additional 10 minutes of SPEX milling the resulting particle morphology is mostly spherical shaped particles less than 100 nm in diameter.

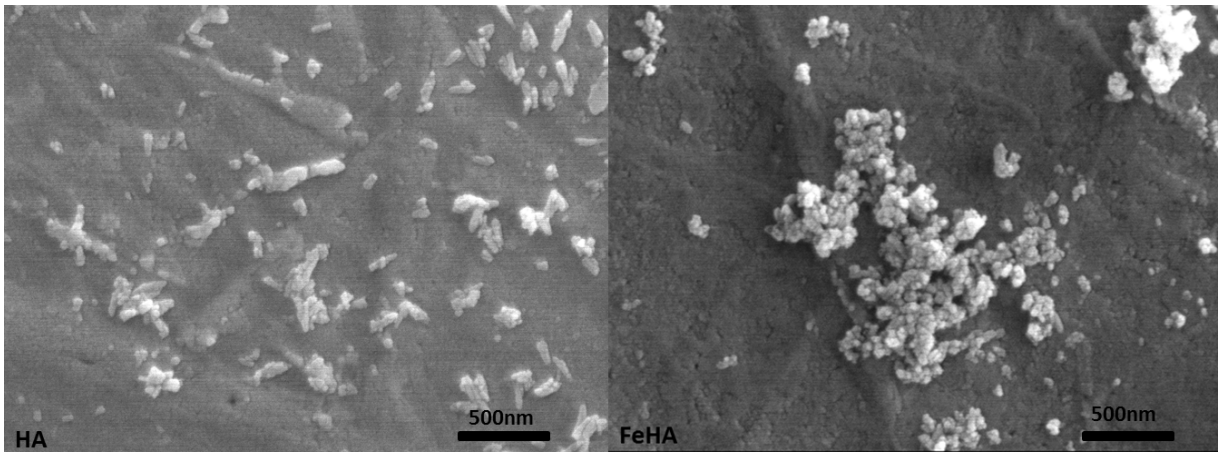


**Figure 4.1** FESEM micrographs of SPEX milled HA and FeHA powders.

*4.3.2 Density and Biaxial Flexural Strength*

Both green and sintered density measurements were performed on HA and FeHA pellet samples. Ten pellets per sintering temperature were measured for both types of powders, and the densities were recorded as the average values of these measurements. Both green and sintered densities are listed in Table 4.1, and Fig. 4.2 shows the sintered densities of both pellet types (HA and FeHA) as a function of sintering temperature.

**Table 4.1** Diameter, thickness, and density measurements of sample pellets before and after sintering, and MOR of sintered pellets

| Sample | Avg. Green Diameter (mm) | Avg. Green Thickness (mm) | Avg. Green Density ($g/cm^3$) | Avg. Sintered Diameter (mm) | Avg. Sintered Thickness (mm) | Avg. Sintered Density ($g/cm^3$) | Avg. Sintered MOR (MPa) |
|---|---|---|---|---|---|---|---|
| **HA 900°C** | 12.81 | 1.63 | 1.65 | 10.66 | 1.43 | 2.50 | 36.50 |
| **HA 1000°C** | | | | 10.33 | 1.38 | 2.73 | 56.50 |
| **HA 1100°C** | | | | 10.23 | 1.34 | 2.86 | 54.34 |
| **HA 1200°C** | | | | 10.17 | 1.33 | 2.92 | 50.41 |
| **HA 1300°C** | | | | 10.21 | 1.37 | 2.80 | 29.13 |
| **FeHA 600°C** | 12.78 | 1.60 | 1.71 | 12.38 | 1.56 | 1.70 | 7.38 |
| **FeHA 700°C** | | | | 12.30 | 1.51 | 1.70 | 7.85 |
| **FeHA 900°C** | | | | 12.00 | 1.47 | 1.78 | 8.92 |
| **FeHA 1000°C** | | | | 10.93 | 1.43 | 2.15 | 16.87 |
| **FeHA 1100°C** | | | | 10.91 | 2.94 | 1.06 | 4.43 |

The average green density of HA pellets was 1.65 $g/cm^3$ and the average green density of FeHA pellets was 1.71 $g/cm^3$. Table 4.1 summarizes the thickness, diameter, and density measurements of the HA and FeHA pellets sintered at different temperatures. For HA, the

sintered densities increased with sintering temperature up to a maximum density of 2.92 g/cm$^3$ at 1200°C, and then dropped at 1300°C. The peak density achieved was 93% the theoretical density of HA. For FeHA, sintered densities also increased with sintering temperature up to a point, before dropping. The highest density, 2.15 g/cm$^3$, was achieved at 1000°C. There is a decrease in diameter with an increase in sintering temperature for every sample measured with the exception of the HA pellets sintered at 1300°C, and also a decrease in thickness compared to the green pellets for every sample measured with the exception of the HA pellets sintered at 1300°C and the FeHA pellets sintered at 1100°C. The FeHA pellets sintered at 1100°C experience a greater than 100% increase in thickness as compared to the FeHA pellets sintered at 1000°C.

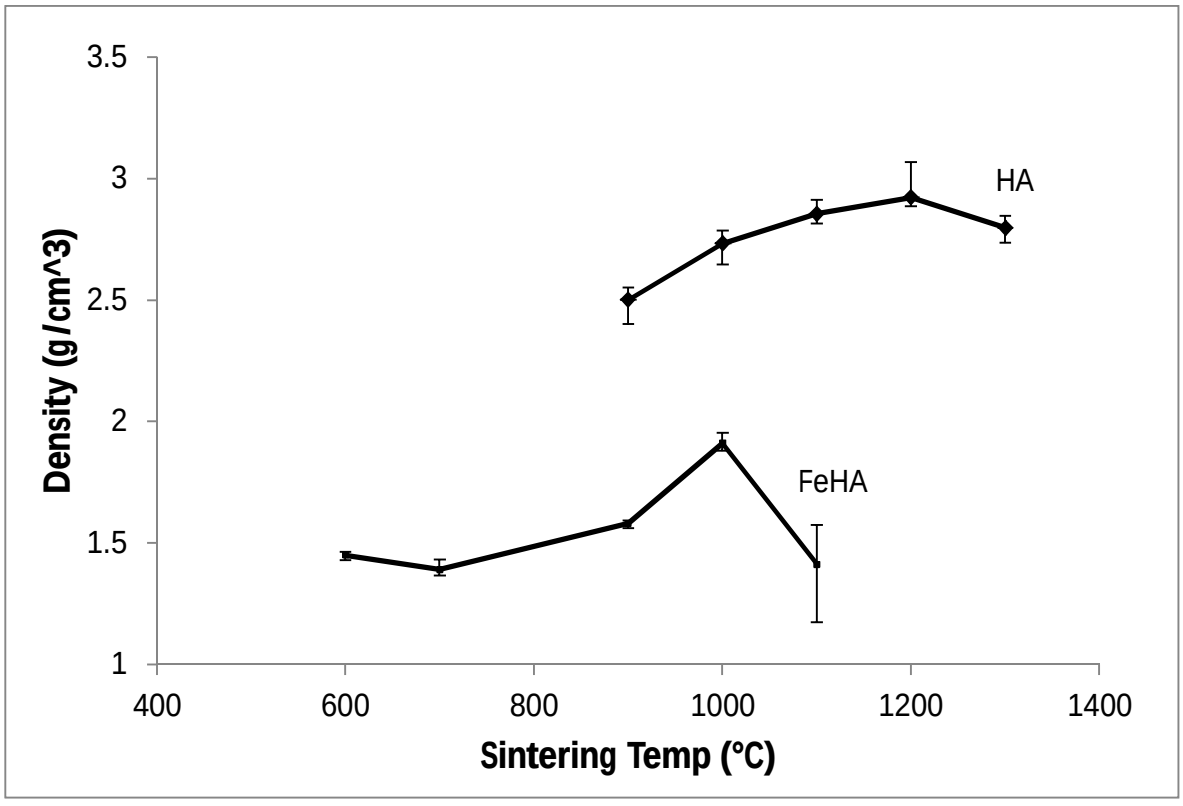


**Figure 4.2** Post-sintered density of HA and FeHA sample pellets.

After pellet densities were measured, the pellets were subjected to a modulus of rupture (MOR) test to study mechanical properties of the sintered pellets. The results of the MOR test are summarized in Table 4.1 and Fig. 4.3. The values are presented as averages plus/minus standard deviations.

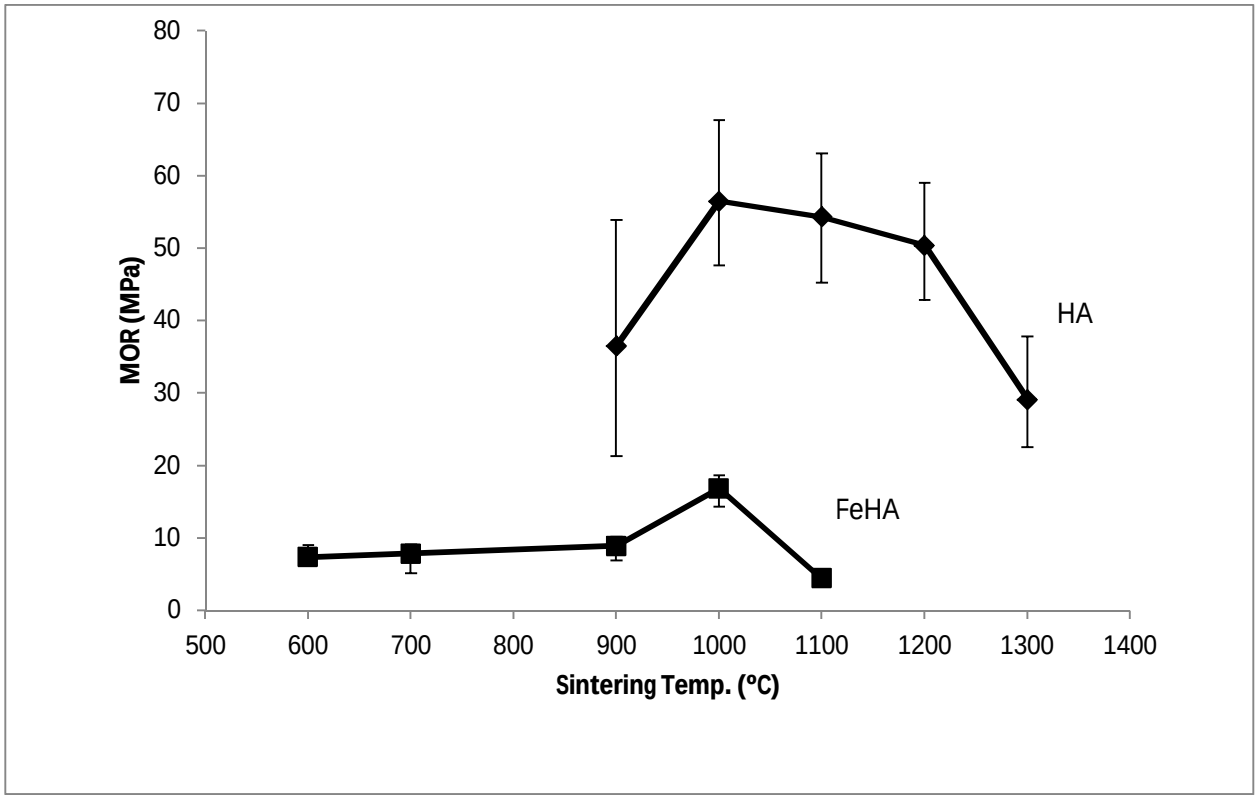


**Figure 4. 3** Modulus of rupture averages for sintered HA and FeHA pellets.

The MOR of the sintered HA samples ranged from the lowest value of 29.13 MPa for pellets sintered at 1300°C to a peak value of 56.50 MPa for pellets sintered at 1000°C. An ANOVA F-test analysis was conducted on the mean MOR values resulting from 6 measurements per each of the 5 temperature points considered. This analysis resulted in an F-value (10.9)

larger than $F_{crit}$ (2.76), thus there is a significant difference between the MOR values for the HA pellets sintered at different temperatures. The MOR of the FeHA sintered samples ranged from the lowest value of 4.43 MPa for pellets sintered at 1100°C to a peak value of 16.87 MPa for pellets sintered at 1000°C (as shown in Fig.4.3). An ANOVA analysis of these sample groups resulted in an F-value of 79.6 compared to an $F_{crit}$ of 2.76, thus there is also statistical significance between the MOR values for the FeHA pellets sintered at different temperatures. In addition to the MOR as a function of sintering temperature displayed in Fig. 4.3, Fig. 4.4 displays the MOR values for each pellet tested as a function of pellet density. Results for pure HA samples are shown in Fig. 4.4a, and FeHA pellet results are displayed in Fig. 4.4b.

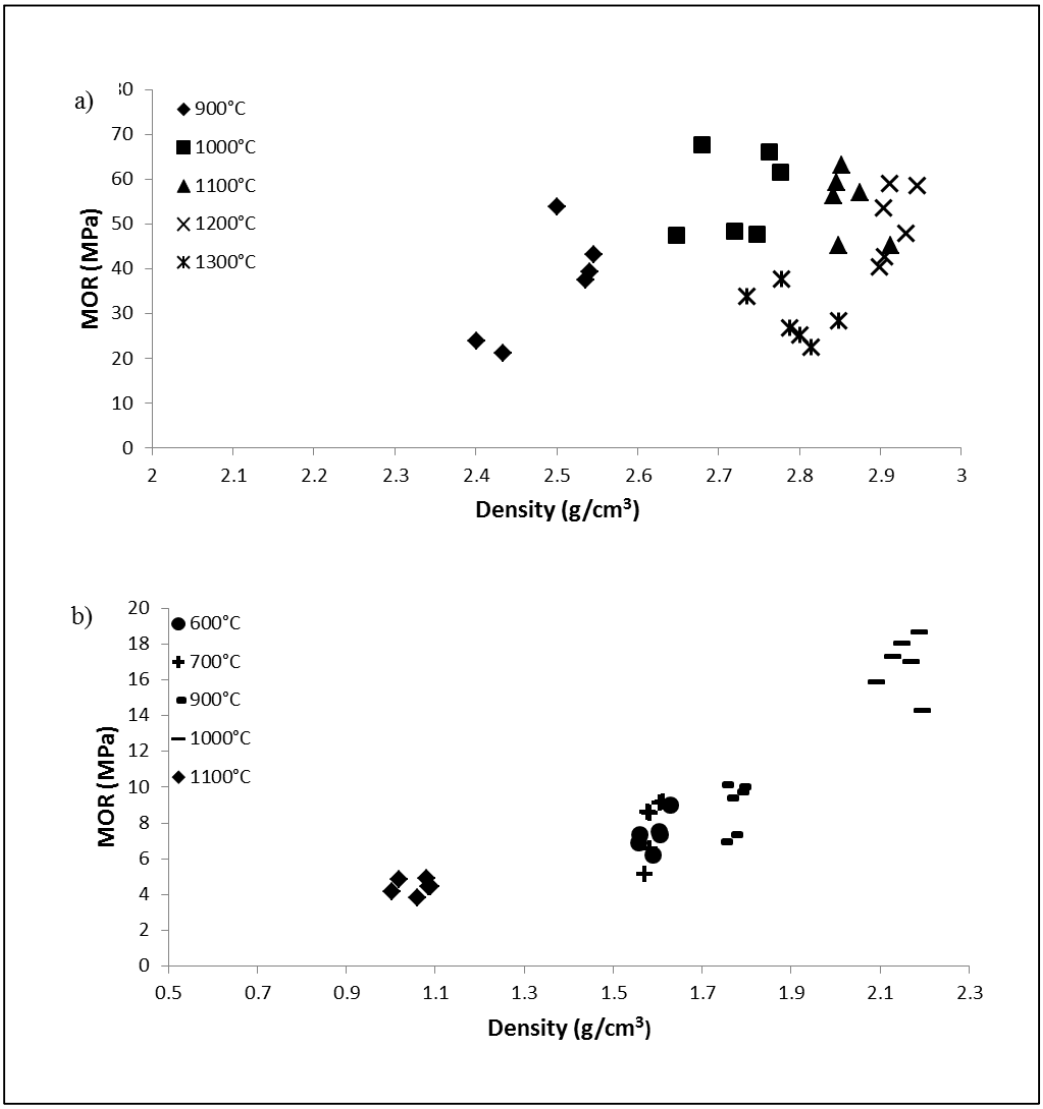


**Figure 4.4** MOR as a function of density for (a) HA pellets and (b) FeHA pellets.

*4.3.3 XRD Characterization*

XRD analysis was used to examine the phase purity and crystal structure of the sintered pellets. The resulting XRD spectra for pure HA and FeHA samples are shown in Fig. 4.5 and Fig. 4.6, respectively.

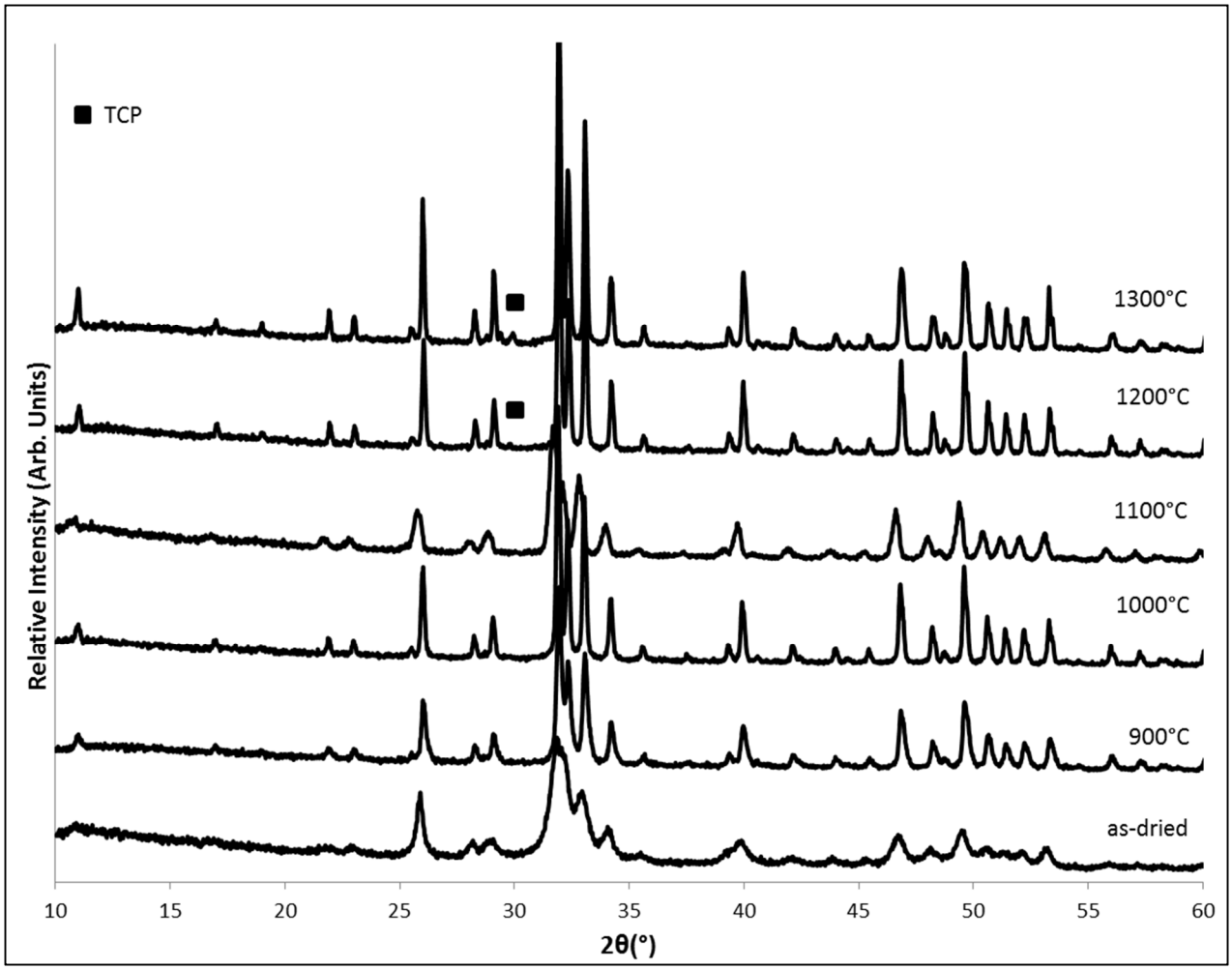


**Figure 4.5** XRD spectra for as-dried HA compared to HA sintered at 900, 1000, 1100, 1200, and 1300°C.

As is demonstrated clearly in Fig. 4.5, the peaks present in each of the sintered samples are identical to those present in the un-sintered HA control spectrum. These peaks match well with the HA JCPD reference card 9-432. The figure shows that there is a small extraneous peak that appears around 30° starting at 1200°C, which would match with the β-TCP peak at 29.68° 2θ.

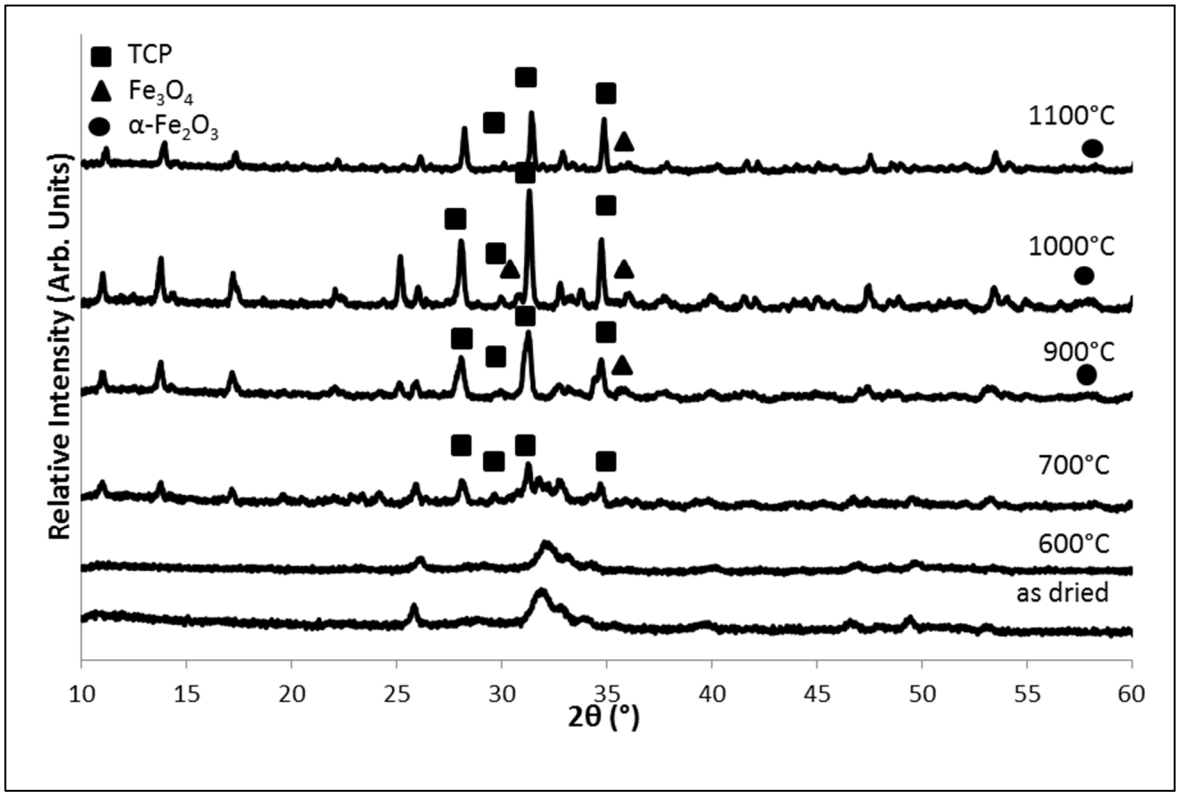


**Figure 4.6** XRD spectra for FeHA compared to FeHA sintered at 600, 700, 900, 1000, and 1100°C.

Fig. 4.6 shows that un-sintered FeHA results in pure apatite peaks matching with JCPD 9-432, although the broad peaks indicate that FeHA is more amorphous than un-substituted HA. FeHA sintered at 600°C also results in pure apatite peaks, but samples sintered at 700°C and above demonstrate the emergence of extraneous peaks, most notably at about 27.8°, 30.1°, 31.1° and 34.5° 2θ. These peaks can be matched to β-TCP, which has significant characteristic peaks at 27.79°, 29.68°, 31.05° and 34.4° 2θ, indicating that these samples are no longer phase pure hydroxyapatite. Another notable extraneous peak which begins to emerge in FeHA samples sintered at temperatures above 600°C, and becomes quite noticeable at 900°C, is at about 35.5° 2θ. This peak is about one-third to one-half the relative intensity of the TCP peak at 34.5° 2θ, and can be assigned to an emerging iron oxide phase. In both HA and FeHA samples, sintering

resulted in sharper XRD peaks, indicating an increase in crystallinity compared to the green pellets.

*4.3.4 FESEM Characterization*

Unpolished fracture surfaces of the sintered pellets were imaged using FESEM allowing the microporosity of these samples and the extent to which the samples have been sintered to be examined. Fig. 4.7 contains the micrographs of the HA pellet cross-sections sintered at different temperatures. It is apparent that at 900°C the pressed HA particles have not started to sinter yet. At 1000°C sintering has just started, as evidenced by the consolidation of packed power particles to bulk material, and there is a system of interconnected pores at the nanometer scale. The amount of sintering is increased at 1100°C, in which some areas are fully densified while some retain the interconnected porosity. The samples sintered at 1200°C are shown to be highly dense with discreet nanometer size pores. At 1300°C, as in the 1200°C, the HA particles seem fully sintered, but discreet pores around micron in size start to appear.

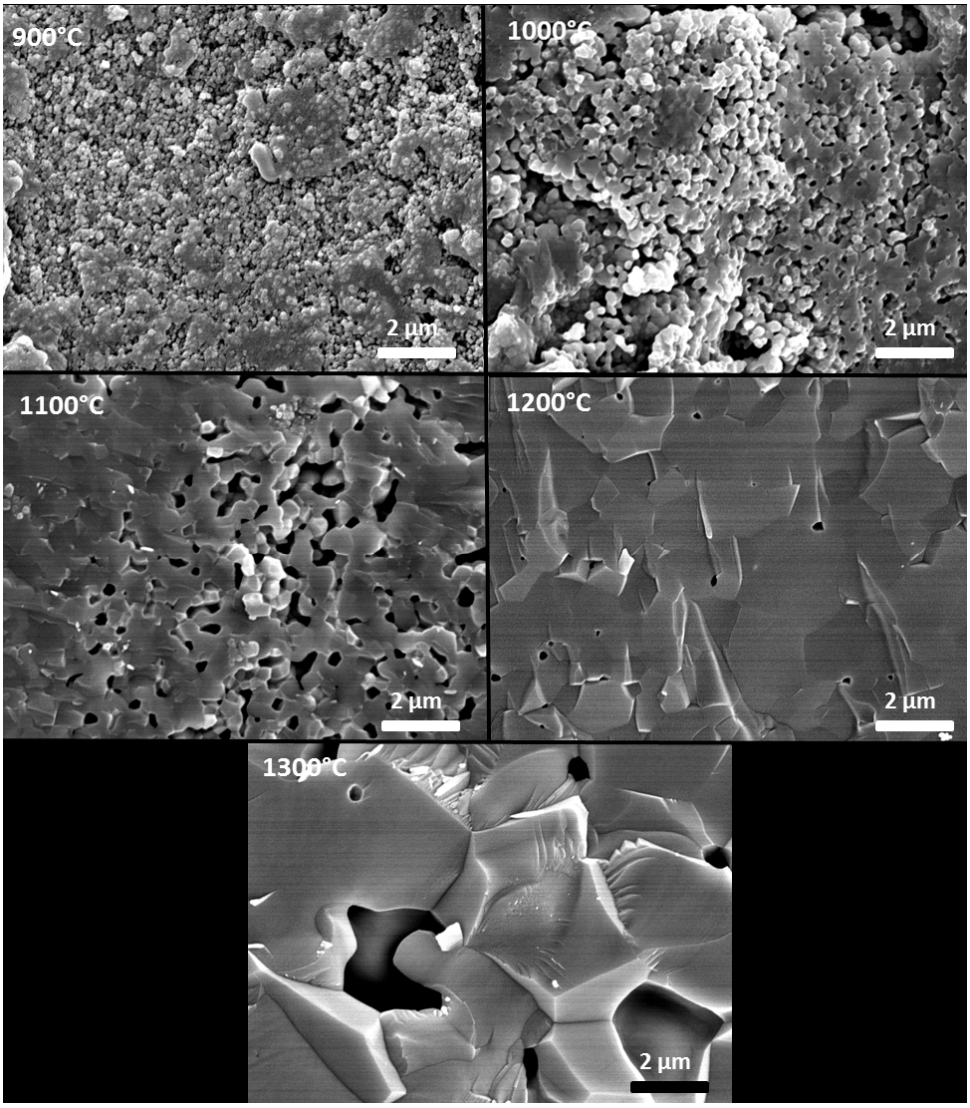


**Figure 4.7** Cross sections of HA pellets sintered at 900, 1000, 1100, 1200, and 1300°C.

Fig. 4.8 contains the micrographs of the FeHA pellet cross-sections sintered at different temperatures. At 600 and 700°C, sintering has not begun in FeHA pellets, and the samples retain the interconnected microporosity seen in the HA samples sintered at 900°C. At 900°C sintering has begun but the interconnected microporosity is preserved and no area is fully sintered/densified. At 1000°C, the FeHA particles are essentially fully sintered and there are dense regions interspersed with micron scale pores. The level of porosity is greater than that

seen in the HA sintered at 1200 and 1300°C. The micrograph of the FeHA sintered at 1100°C was taken on one of the walls in the pellets. This group of samples is fully dense and contains no microporosity.

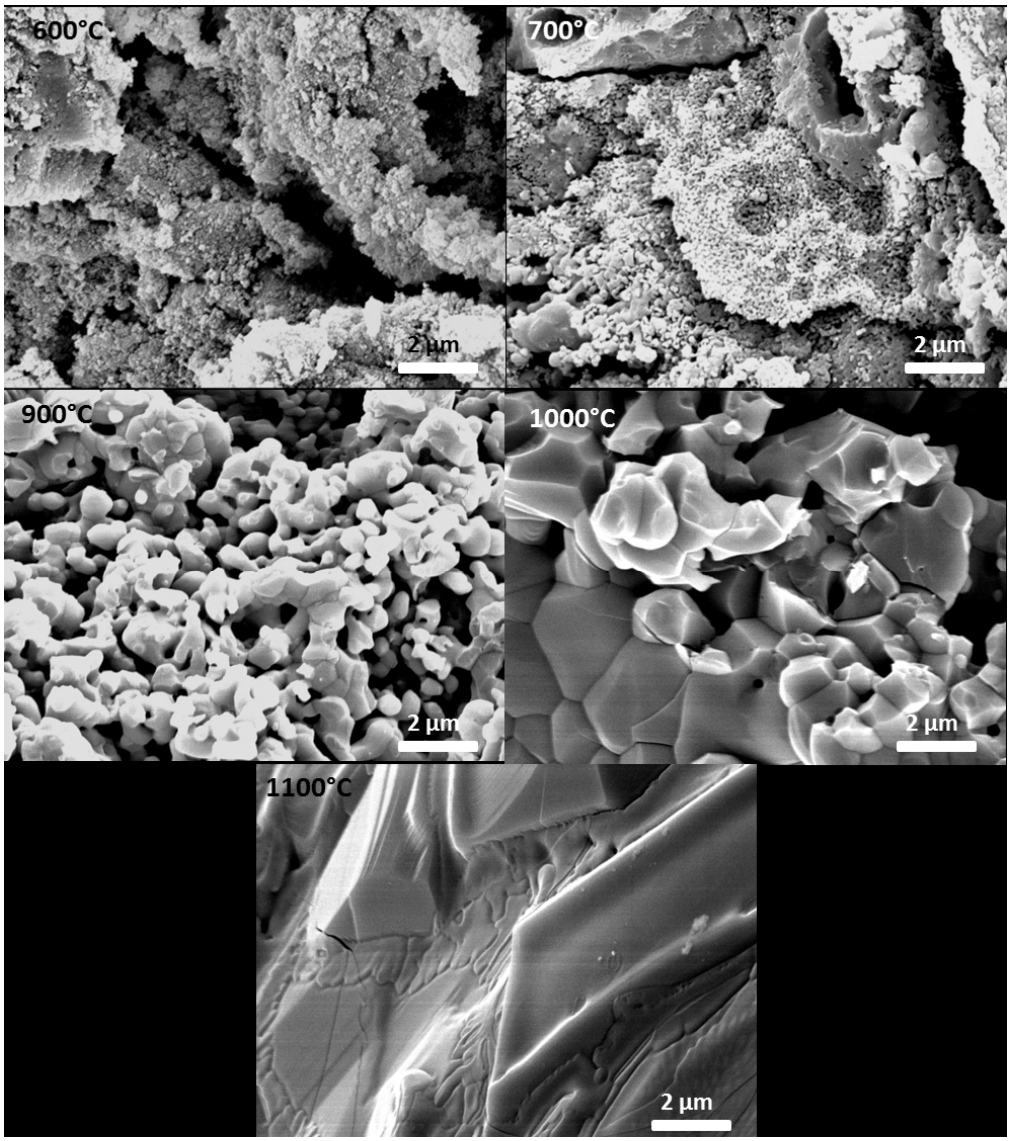


**Figure 4.8** Cross sections of FeHA pellets sintered at 600, 700, 900, 1000, and 1100°C.

FESEM images were also taken to examine the microstructure and porosity of the polished surface of the sintered pellets. The FESEM micrographs in Fig. 4.9 depict that after sintering at each temperature point from 900-1300°C, the resulting microstructure of HA was dense pellets with pores in the micron range. At all sintering temperatures from 900°C up to 1300°C pores were comparable in size, up to about 10 μm. Pellets sintered at 900, 1000, and 1100°C show no obvious differences in microstructure or porosity. Pellets sintered at 1200°C have increased porosity as compared to the pellets sintered at lower temperatures. Pore number was greatest in the pellets sintered at 1300°C.

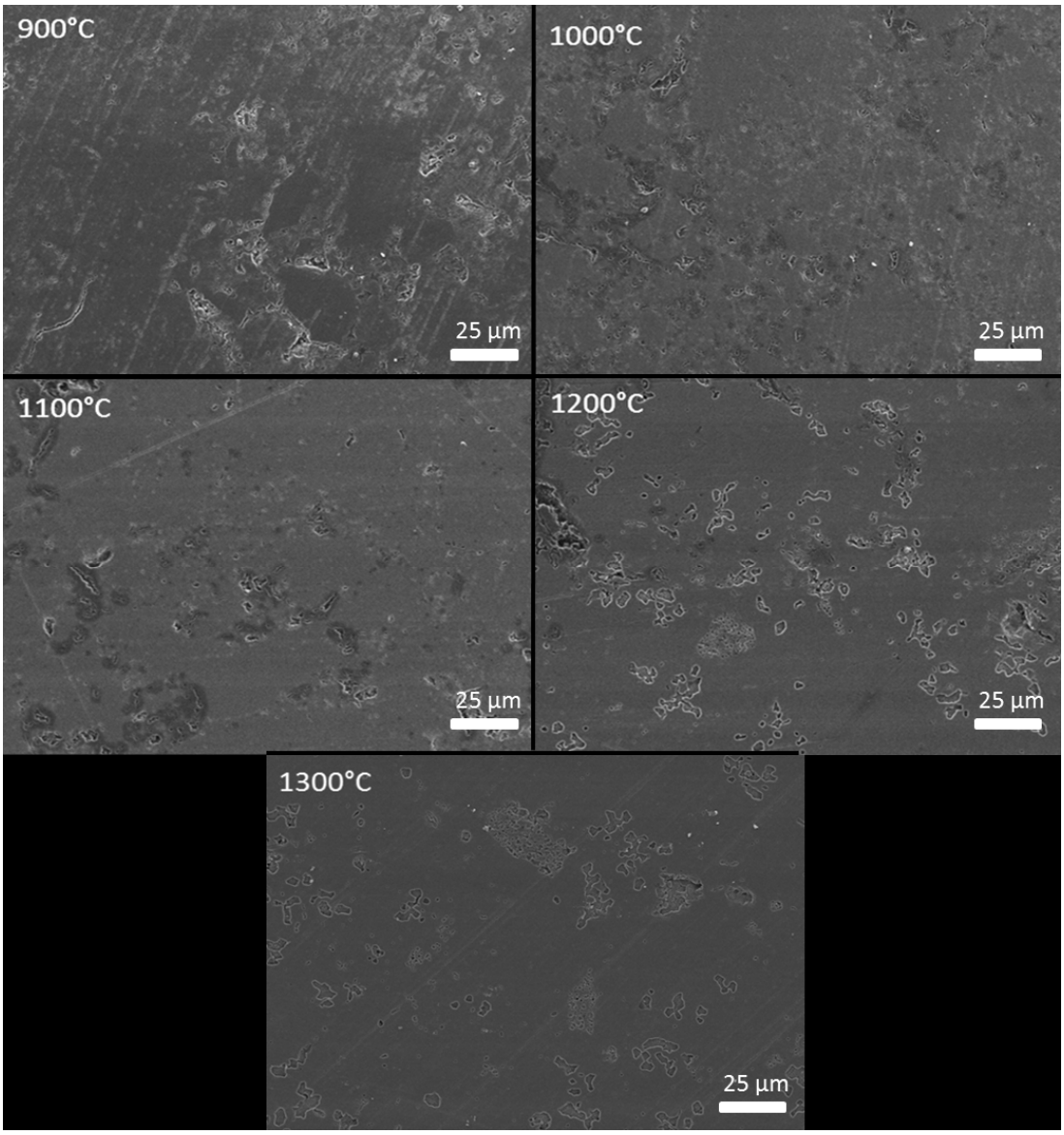


**Figure 4.9** FESEM micrographs of polished HA pellets sintered at 900, 1000, 1100, 1200, and 1300°C.

The FESEM micrographs in Fig. 4.10 depict the polished FeHA pellets sintered at temperatures from 600-1100°C. The pellets sintered at 600 and 700°C exhibit many pores, indicating they are hardly densified. In the pellets sintered at 900 and 1000°C, they are relatively denser but still with many pores. The bottom two micrographs in Fig. 4.10 show the microstructure of the FeHA pellets sintered at 1100°C, which is drastically different from any of

the other microstructures observed at lower sintering temperatures. The pores in these pellets are at least an order of magnitude larger than the pores seen in the FeHA samples sintered at lower temperatures. The pores are separated by dense walls that are tens of microns thick. The micrograph in which the outer shell of the FeHA pellet sintered at 1100°C was left intact shows that the shell structure of these samples is essentially completely dense.

The FeHA sintered pellets exhibit distinctly different morphologies than the HA sintered pellets. The FeHA samples sintered at 600 and 700°C are less dense than any of the sintered HA samples. FeHA pellets sintered at 900 and 1000°C have similar microstructures to those seen in the HA pellets sintered at 1100 and 1200°C, respectively. These samples are dense but with pores in the micron size range; however, the numbers of pores in these samples are higher than those in the HA samples sintered at 1100 and 1200°C or FeHA pellets sintered at lower temperatures (e.g. 600 or 700°C). The microstructure observed in the FeHA samples sintered at 1100°C is not only drastically different from any other FeHA samples, but it is significantly different from any microstructures observed in the HA samples sintered at any temperature as well.

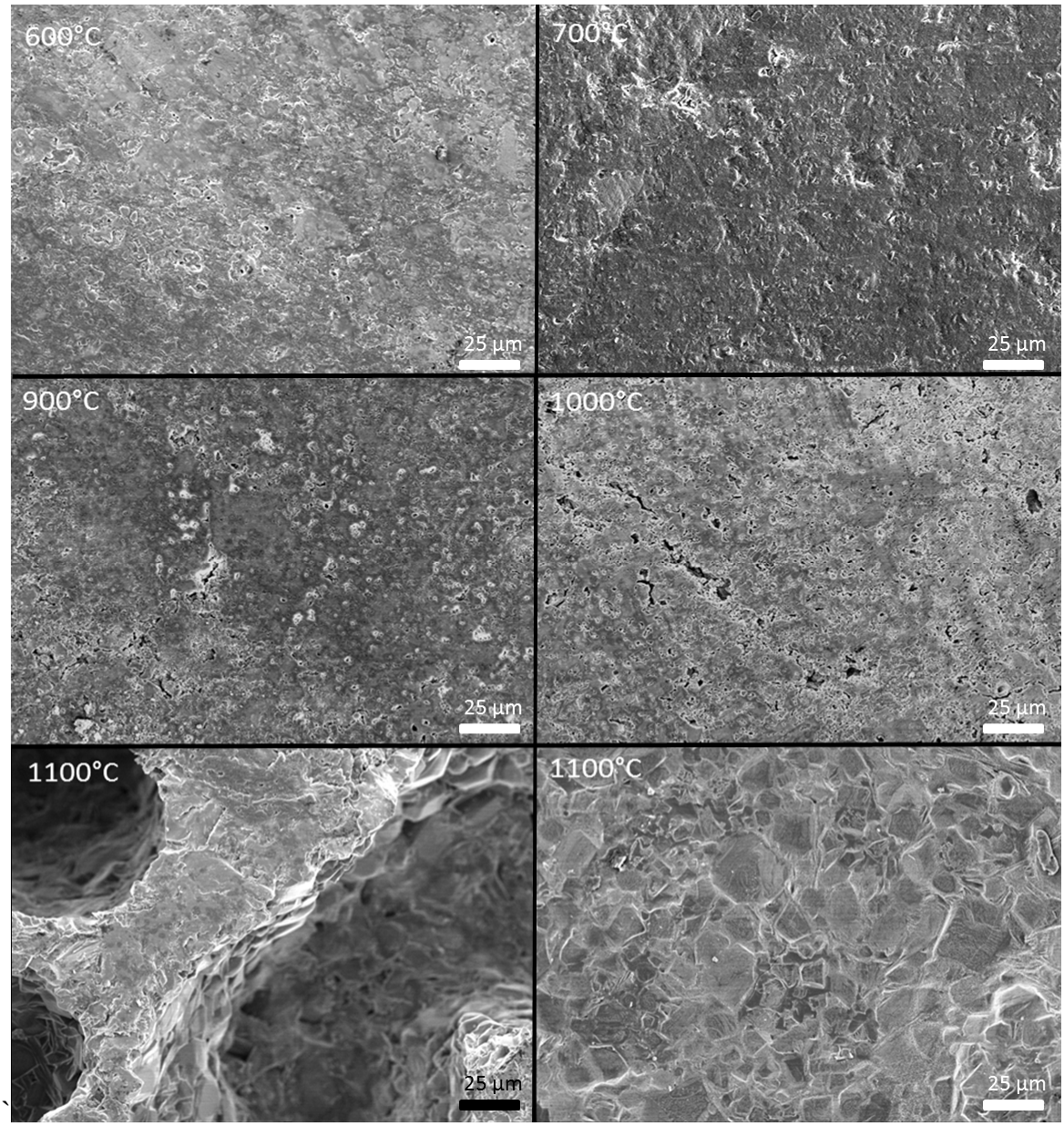


**Figure 4.10** FESEM micrographs of polished FeHA pellets sintered at 600, 700, 900, 1000, and 1100°C (bottom left), and a micrograph of an unpolished FeHA pellet sintered at 1100°C with its outer shell intact (bottom right).

Fig. 4.11, which consists of a micrograph of a cross-section of a FeHA pellet sintered at 1100°C, further examines the unique structure of this particular sample group. It is apparent that the pellet consists of a dense shell of a few hundred microns thick enclosing a porous core. The

microstructure of this core consists of pores that are hundreds of microns large separated by walls that are tens of microns thick. The pores are not interconnected.

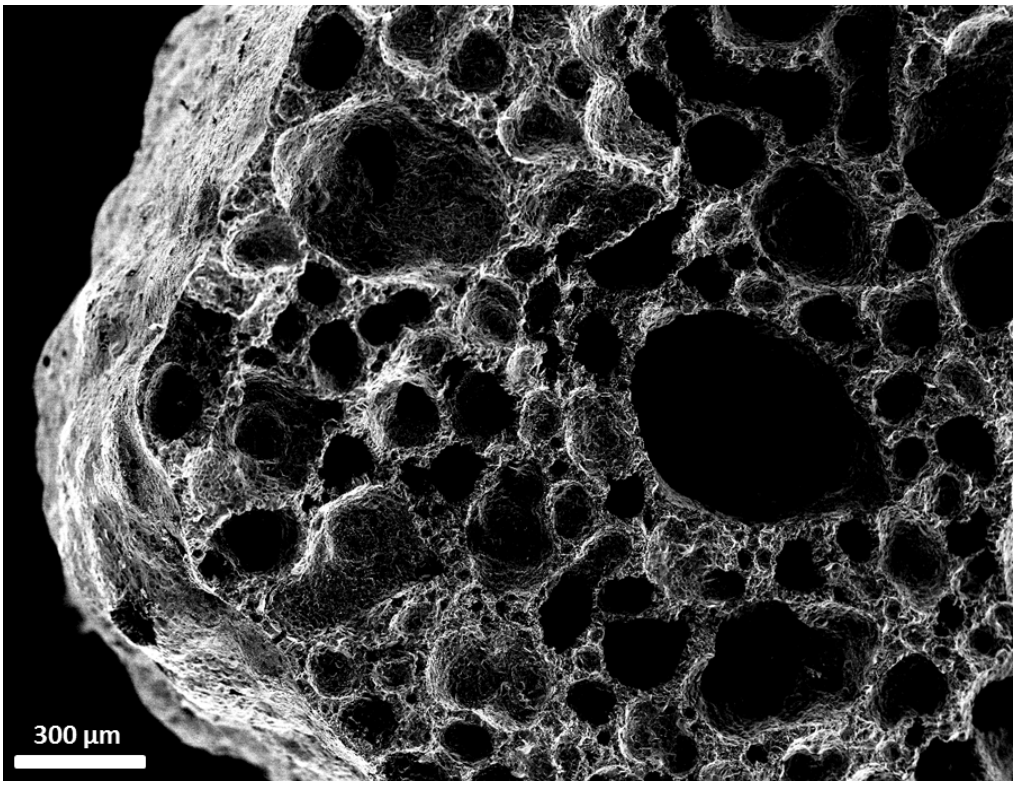


**Figure 4.11** Cross-section of FeHA pellet sintered at 1100°C showing dense outer shell and highly porous interior of pellet.

*4.3.5 Cell Culture Study*

Biocompatibility of FeHA was assessed by monitoring the proliferation of MC3T3-E1 cells over the course of a week with the alamar blue assay. Alamar blue monitors the metabolic activity of cells, which can be related to the number of cells present. Healthy cells readily take up and reduce the active ingredient resazurin and reduce it to resorufin; damaged cells can reduce resazurin but at a slower rate. Fig. 4.12 illustrates the biocompatibility of FeHA relative to HA. Cell proliferation is inhibited from 1 to 3 days at higher administered dosages of sample powder,

for both HA and FeHA. Over the course of 7 days cell viability with FeHA was comparable to HA when applied at the same dosage, and the viability of cells exposed to higher dosages of HA recovered to be comparable to the viability of cells exposed to lower HA dosages.

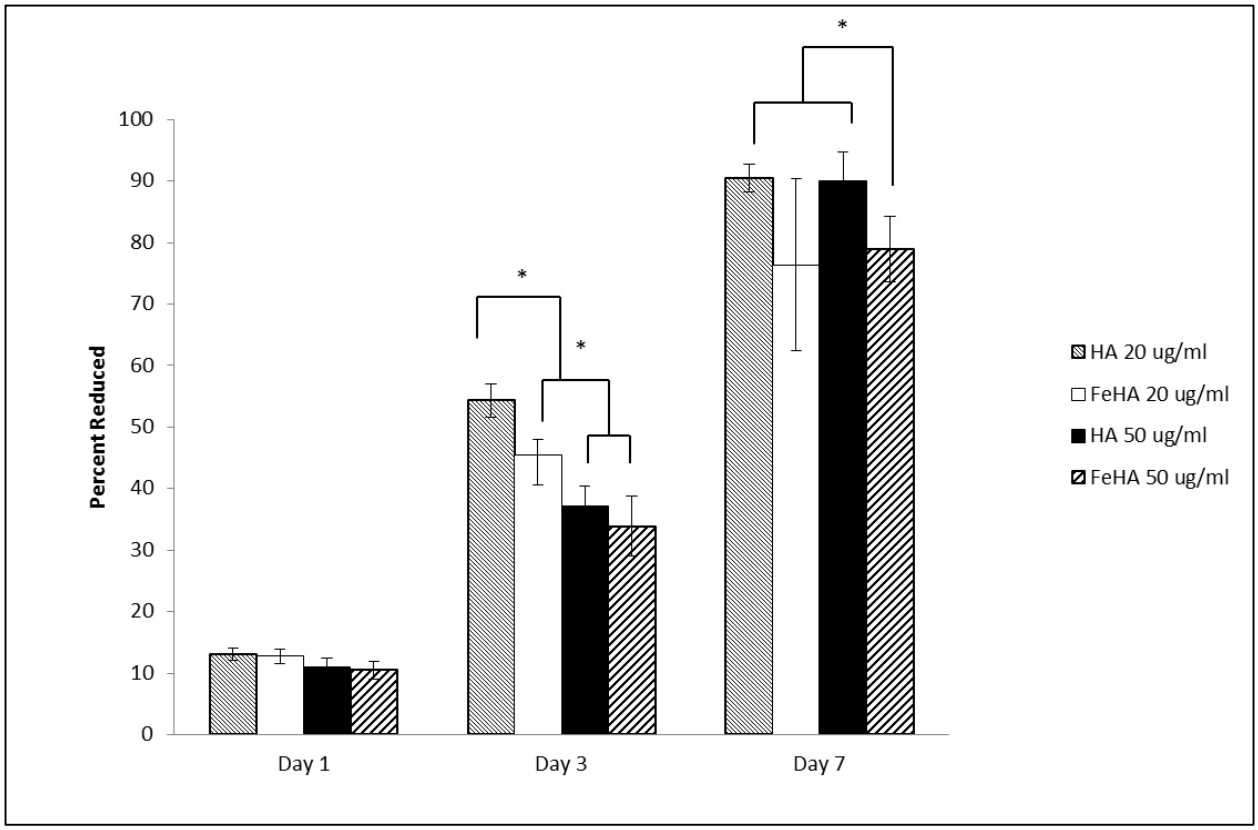


**Figure 4.12** Alamar blue cell culture assay results at 1, 3, and 7 day time points.

*4.4 Discussion*

In general, HA can be sintered up to 1200°C or above before it is decomposed to TCP and CaO [99, 100]. In this chapter, HA was sintered from 900°C up to 1300°C. Ion substitution was also used to synthesize FeHA, an iron substituted material which maintains an apatite crystal structure but with paramagnetic properties [2]. FeHA was sintered from 600°C up to 1100°C. The HA pellets underwent shrinkage (from an average diameter of 12.81 mm for the green

pellets down to an average diameter of 10.17 mm for pellets sintered at 1200°C) but otherwise retained their white appearance with flat top and bottom surfaces. The FeHA pellets, on the other hand, underwent an obvious visual change upon sintering. As is seen in Fig. 4.13, the un-sintered FeHA pellets were yellow. After being sintered at 600°C the FeHA was darkened, but remained yellow. The pellets sintered at 700°C developed a muddy brown color, which became redder up to 1000°C. Despite the distinct color changes present at the aforementioned temperatures the pellets retained the typical flat top and bottom surfaces that was seen in all of the pure HA samples, with shrinkage from 12.78 mm in diameter of the green pellets to 10.93 mm in the pellets sintered at 1000°C. However, the samples sintered at 1100°C changed drastically in appearance. These samples displayed a shiny outer shell with a dark metallic brown color. Upon breaking the pellets open, the inside was a matte dark brown color, with large pores visible to the naked eye. Additionally, although the pellet diameter shrank dramatically, the thickness increased significantly. As a combination of these two facts, the final density of the pellets actually dropped significantly compared to those sintered at 1000°C. It was also observed that both the top and bottom surfaces of the pellets became bumpy, as opposed to the flat surfaces that were observed at lower sintering temperatures for FeHA samples.

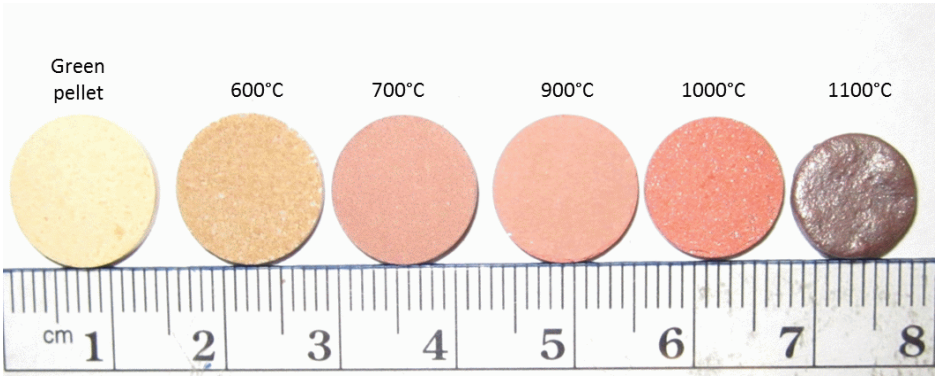


**Figure 4.13** Photograph of FeHA pellets sintered at various temperatures.

In addition to obvious visual differences between the pure HA pellets and the FeHA pellets, densification behavior and mechanical properties were also significantly different between the two material types. The initial green density for the FeHA pellets was higher than that of the pure HA pellets, 1.71 g /cm3 as compared to 1.65 g/cm$^3$, as the starting FeHA powder was finer and easier to pack. Despite this higher initial density, the sintered densities of the FeHA pellets were considerably lower than those of the HA pellets. Although a lower density is to be expected at lower sintering temperatures since densification typically increases with sintering temperature prior to the onset of decomposition [104], even when comparing FeHA and HA samples sintered at the same temperature the FeHA pellet densities are much lower. At their peak density, the HA pellets attain a density of 2.92 g/cm$^3$ sintered at 1200°C, which is 93% of the theoretical density of HA (3.156 g/cm$^3$). The density of FeHA on the other hand, never approaches the theoretical density of HA. It peaks at 2.15 g/cm$^3$, or 68% theoretical density, after sintering at 1000°C before decreasing drastically at higher temperatures.

The MOR of the FeHA pellets are also considerably lower than that of the HA pellets, which is unsurprising considering the lower densities observed for the FeHA pellets. The HA pellets achieve a high MOR value of 56.50 MPa, which compares favorably to the mechanical properties of bulk HA achieved by others in the literature [105, 106] as well as the mechanical properties of natural bone, which has flexural modulus values ranging from 35 to 283 MPa, depending on factors such as patient age, overall health, and location in the body [107].

The MOR is displayed as a function of sintering temperature in Fig. 4.2, and as a function of density in Fig. 4.3 as well as Table 1. It is shown in Fig. 4.2 that the MOR roughly plateaus between 1000 and 1100°C, with a slight decrease at 1200°C and a significant decrease (along

with a decrease in density) at 1300°C. This may be due to the start of decomposition of HA to TCP at high temperatures (e.g. 1200 and 1300°C). The poor mechanical properties of the FeHA pellets may also be partially explained by decomposition of the HA to TCP and the formation of an iron oxide phase, as phase transformations induce volume changes and the resultant stresses decrease the mechanical integrity of the sintered body.

The FESEM images of polished sintered HA pellets (Fig. 4.6) show a dramatic increase in porosity at 1300°C, corresponding to the decrease in density shown in Fig. 4.1 and Table 1. The size of the micropores for the HA pellets sintered at 1300°C are also larger than those seen in the pellets sintered at 1200°C. This may be due to increased HA decomposition occurring at the higher temperature. Initially, sintering causes the close of pores and concurrently dehydroxylation results in the formation of an internal vapor pressure that exceeds the mechanical strength of the solid. This results in the formation of blowholes. At higher temperatures with the onset of decomposition a large amount of irreversible dehydroxylation occurs concurrently with decomposition, of which water vapor is a product, leading to a collapse of the hydrated HA structure, and a large increase in blowhole area [108].

The FeHA pellets were shown to have increased porosity from 900-1000°C (Fig. 4.10) followed by a dramatic change in structure at 1100°C, corresponding with dramatic decreases in density and MOR at this temperature. At 1100°C the walls separating the large discreet pores in the FeHA pellet are seen to be fully dense with no microporosity. A dramatic phase change between 1000 and 1100°C may account for the drastic microstructural change observed. No such drastic change was seen at any of the studied temperature points in the HA pellets. The core/shell structure seen in Fig. 4.11, in which the pellets have a thin fully dense outer shell and a highly porous interior core, can likely be explained by the fact that the outside surface of the

pellet is abundant in oxygen, forming a thick iron oxide layer which becomes the dense outer shell of the pellet. Then, as decomposition releases significant amounts of gas, the gas is trapped inside the pellet due to the dense shell, resulting in large pores observed in the FeHA pellets sintered at 1100°C.

It is clear from visual inspection, as well as density and mechanical property measurements, that the FeHA pellets have significantly different sintering behavior than the pure HA pellets. This is likely caused by the presence of iron ions in the HA lattice causing reduced stability of the apatite crystal lattice and initiation of decomposition and formation of second phases at significantly lower temperatures than those which induce decomposition in pure HA. XRD analysis has confirmed this hypothesis.

A single-phase HA was achieved at sintering temperatures up to 1200°C, which was indicated by no extraneous peaks being present in the relative XRD spectra (Fig. 4.5). Thermal stability up 1200 °C is typical in pure HA [98, 99]. Decomposition to β-TCP began at around 1200°C, as indicated by the emergence of a peak at 30° 2θ. The onset of decomposition explains the decrease in density and MOR in the HA pellets sintered at 1200 and 1300°C. The FeHA pellets were shown to be considerably less thermally stable than HA, and decomposition and the emergence of second phases started at temperatures as low as 700°C (Fig. 4.6). In FeHA sintered at 700°C and above, extraneous peaks indicating the presence of TCP emerge at about 27.8°, 30.2°, 31.1° and 34.5° 2θ. There is also an extraneous peak observed at 35.5° with a relative intensity about one-third to one-half that of the β-TCP peak seen at 34.5° 2θ. The TCP reference peak at 34.4° has a relative intensity of 65, but HA and β-TCP peaks in the area of 35.5° (35.51° and 35.02°, respectively) each have low relative intensities of 6. The possibility should be investigated, therefore, that the peak located at 35.5° may come from a different

second phase, most likely an iron oxide phase. In fact, magnetite ($Fe_3O_4$), maghemite ($\gamma$-$Fe_2O_3$), and hematite ($\alpha$-$Fe_2O_3$) are possibilities. Magnetite and maghemite each have a significant peak around 30° which may be overlapping with the β-TCP peak at that location. Additionally, the mineral magnetite has a peak at 35.45° with a relative intensity of 100 according to JCPD reference card 19-629 and maghemite has a peak at 35.66° with a relative intensity of 100 (JCPD 39-1346), either of which could potentially account for the extraneous peak seen at 35.5° in the spectra of the FeHA samples sintered above 700°C. Careful examination of the FeHA pellet spectra in Fig. 4.5 shows that in pellets sintered at 900°C and above a small peak is present at about 57.0° 2θ. Additionally, there is a small but obvious peak at 33.5° which is most prevalent in the FeHA sample sintered at 1000°C. Magnetite has a reference peak with a relative intensity of 30 at 56.99° and hematite has a reference peak with a relative intensity of 100 at 33.31° 2θ, therefore the sintered FeHA pellets likely contain a mixture of calcium phosphate (HA and TCP), $\alpha$-$Fe_2O_3$ and $Fe_3O_4$ phases. The presence of the iron oxide phases would account for the color change seen in the sintered FeHA pellets as well. Hematite is often a red color whereas magnetite is a dark color. Based on the change in pellet appearance, as well as the XRD data we can conclude that FeHA pellets sintered at temperatures below 700°C in air contain pure apatite phase (and have a resultant yellow color due to the presence of iron ions), and samples sintered at higher temperatures undergo various phase transformations. Pellets sintered from 700-900°C contain a mixture of calcium phosphate phases (HA and TCP) and iron oxides, mostly in the form of hematite (resulting in reddish colored pellets) pellets sintered at 1000°C contain calcium phosphate phases and a mixture of hematite and magnetite, and samples sintered at 1100°C mostly contain a mixture of calcium phosphate phases and magnetite ($Fe_3O_4$) (resulting in dark brown colored pellets).

The incorporation of iron ions into the hydroxyapatite lattice results in a FeHA material that is less stable than pure HA, as proven by their difference in sintering behavior. The FeHA selected for use in this study was soaked in the ion exchange solution for 1 hour, and as such had the lowest iron content of the powders studied in the author's previous work [97]. Because increasing iron content results in decreased lattice parameters and crystallinity, it can be hypothesized that with an increase in iron content, the differences in sintering behavior as compared to the pure HA would be even more dramatic. The low sinterability and low MOR of FeHA as compared to pure HA makes the FeHA unsuitable for bulk applications. It can, however, be useful in applications which call for biocompatible nanoparticles in a powder form. Cell culture studies indicated that there was no significant limitation in cell viability after 1 week of exposure to FeHA when compared to pure HA. The initial decrease in cell viability at days 1 and 3 may be due to the fact that although HA is biocompatible, some recent studies have shown that calcium phosphates can have an inhibitory effect on osteoblast *in vitro* [109-111]. Although *in vitro c*ell culture studies are useful tools for initial-stage biological screening of biomaterials, behavior *in vivo* is completely different. Results from an *in vitro* degradation study (Chapter 3) suggest solubility of both FeHA and HA is minimal after 1 week, which was the maximum time point considered in the cell culture study presented in this work, and as such the different material solubilities should have a minimal influence on cell proliferation after 1 week. The lower thermal stability of the FeHA material suggests that it may degrade in the body faster than pure HA. A faster degradation rate than that experienced by pure HA may be a desirable trait, depending on the specific application. Possible applications which may call for a shorter *in vivo* dwell time may include use as a drug delivery vehicle or for cancer hyperthermia.

*4.5 Conclusion*

This chapter successfully examined the sintering behavior of magnetic, biodegradable FeHA nanoparticles in a systematic and thorough manner. HA was sintered to a maximum density of 2.92 g/cm$^3$ and a peak MOR of 56.50 MPa. It did not begin to decompose until 1200°C. Sintering FeHA at temperatures as low as 700°C caused its decomposition into a multi-phase material containing HA, TCP, hematite, and magnetite. The maximum density and MOR achieved by FeHA were 2.15 g/cm$^3$ and 16.87 MPa, respectively. It was discovered, through the use of density measurements, mechanical testing, FESEM, and XRD analysis, that FeHA has lower thermal stability than pure HA thus, it is expected that FeHA will degrade faster in vivo than pure HA. This fact, combined with material biocompatibility and the paramagnetic properties of FeHA suggest that it is suitable for applications which require fast biodegradable magnetic nanoparticles.

# Chapter 5

## Synthesis and Characterization of Cobalt-Substituted Hydroxyapatite Powders

### *5.1 Introduction*

Among the HA properties that can be modified by substitutions are magnetic properties. Pure HA is diamagnetic, but the substitution or incorporation of metal ions with magnetic properties can yield HA with paramagnetic properties. Currently, the most commonly applied method to yield HA with paramagnetic properties is the fabrication of iron-substituted apatite [62-67]. Another possible substitution that may result in paramagnetic properties is the substitution of cobalt ions for calcium ions in the HA crystal lattice. There have been limited studies recently on the substitution of cobalt into the HA lattice. Stojanovic et al. and Veselinovic et al. synthesized CoHA via hydrothermal treatment where $Co^{2+}$ substituted for $Ca^{2+}$ up to about 12 atomic % [112, 113]. Careful analysis was conducted on the crystal structure of the resulting material, but limited results were reported regarding the effect that cobalt substitution had on other material properties. Tank et al. used a surfactant mediated wet synthesis approach to substitute cobalt into HA up to about 3.7 wt %. At that level, the formation of a secondary brushite phase was evident, although there was no evidence of this phase at lower substitution levels [114]. Moseke et al. also synthesized HA in the presence of cobalt, in order to examine the effect of metal ions on phase composition and crystallinity of HA and predict the effect that metal ions leaching from biomedical implants would have on biomineralization and bone remodeling [115]. Jia et al. formed mineralized collagen composites by soaking collagen type I in a simulated body fluid containing $Co^{2+}$ and were able to form HA coating on collagen with no evidence of secondary phase formation [116]. The main objectives

of this chapter were to synthesize cobalt substituted HA (CoHA) powder and characterize the effects that this substitution had on materials properties including morphology, crystal structure, and magnetic properties.

Cobalt is an essential trace element naturally found in the human body. It is essential to animal nutrition and is contained in vitamin $B_{12}$ [117]. On average, an individual intakes about 300 μg of cobalt daily from food and fluids [118]. An average 70 kg human has a total body burden of about 1.5 mg of cobalt, distributed in such a way that the majority of the cobalt is found in the liver. Excess cobalt is excreted mainly via the kidneys [118]. Although cobalt is naturally present in the human body, and the body is equipped to excrete moderate amounts of excess cobalt, too many cobalt ions are potentially toxic [119]. A degradation study was conducted in this chapter to predict whether the amount of cobalt released from CoHA would be excessive, or if the rate of cobalt release was low enough to partially address and alleviate toxicity concerns.

## *5.2 Materials and Methods*

### *5.2.1 Synthesis of Hydroxyapatite Powder*

Hydroxyapatite powder was prepared via a wet precipitation method based on work done by Kothapalli et al. [36]. A 200 mL ammonium phosphate (99+%, Acros) solution at a concentration of 2 g/dL was added dropwise under vigorous stirring to 600 mL of an aqueous calcium nitrate tetrahydrate (99%, Fisher) solution of the same concentration at 75°C. An 80 mL volume of ammonium hydroxide (~30%, Fisher) was also added. After 3 hours of stirring at 75°C, the HA particles were collected by filtration and washed with deionized water until the

filtrate became neutral. The collected HA was dried at 90°C for 12-16 hours and ground manually into powder.

### *5.2.2 Ion Substitution*

Cobalt was incorporated into HA in this study using two different approaches. In the first case, cobalt was substituted into the lattice via a simple ion exchange procedure. In the second case, cobalt was incorporated during HA powder synthesis. In both cobalt substitution methods, the cobalt source used was cobalt (II) chloride hexahydrate (>95%, Acros).

#### *5.2.2.1 Co Substitution via Ion Exchange*

HA powder was subjected to a simple soaking procedure to achieve cobalt substitution for calcium in the HA crystal lattice. HA powder was soaked in a cobalt chloride solution at a concentration of 0.02 M under moderate stirring for one hour at room temperature, and then collected by filtration and washed by deionized water. The resulting powder was dried and ground manually.

#### *5.2.2.2 Co Substitution During HA Synthesis*

Cobalt was incorporated during HA synthesis using the synthesis procedure as described above. A quantity of cobalt (II) chloride that would allow for 10 wt% substitution was added to the phosphate containing solution. The rest of the synthesis was conducted exactly as described in section 2.1. The cobalt (II) chloride hexahydrate (>95%, Acros) was added to a 200 mL ammonium phosphate (99+%, Acros) 2 g/dL aqueous solution. This solution was then added dropwise under vigorous stirring to 600 mL of an aqueous 2 g/dL calcium nitrate tetrahydrate

(99%, Fisher) solution at 75°C. An 80 mL volume of ammonium hydroxide (~30%, Fisher) was also added. After 3 hours of stirring at 75°C, the CoHA particles were collected by filtration and washed with deionized water until the filtrate became neutral. The collected CoHA was dried at 90 °C for 12-16 hours and ground by hand into a powder.

### *5.2.3 EDX Characterization*

Energy dispersive X-ray spectroscopy (EDX) was used to verify the presence of cobalt in the sample powders. A Thermo Noran EDS detector coupled to a JEOL JSM 6335 field emission scanning electron microscope (FESEM) was used for chemical analysis. Powder samples were attached to a microscope stub with carbon tape, and then inserted into the microscope chamber as is for analysis.

### *5.2.4 FESEM Characterization*

A JEOL JSM 6335F field emission scanning electron microscope was used to examine the morphology of sputter coated powder samples with an accelerating voltage of 10 kV. Sample powders were dispersed in ethanol and sonicated for 20 minutes to reduce agglomeration before being collected on copper microscopy grids. Samples were then sputter coated for 1 minute prior to imaging. Image-J software was used to measure particle width and length for each powder type. A total of 20 particles for each sample type were measured.

### *5.2.5 XRD Characterization*

Powder samples of HA, CoHA via ion exchange and CoHA via wet synthesis were examined using a Bruker D2 Phaser X-ray diffractometer with a copper target, and voltage and

current conditions of 40 kV and 40 mA, respectively. Conditions used were a 0.02° 2-theta step size and a scan speed of 4°/min with a 2-theta range of 10-90.

### *5.2.6 FT-IR Characterization*

A Niclotet Magna 560 Fourier Transform Infrared (FT-IR) Spectrometer was used to compare the functional groups of pure HA and the CoHA samples. This characterization was carried out using classic KBr pellet technique in a transmission mode. Each FT-IR spectrum was the average of 32 scans with a resolution of 4.0 $cm^{-1}$ in the range of 4000-400 $cm^{-1}$.

### *5.2.7 XPS Characterization*

X-ray photoelectron spectroscopy (XPS) was employed using a VG X-ray Photoelectron Spectrometer with Al Kα radiation source operating at 10-11 kV and 150 watts. Survey spectra from 1100-0 eV were acquired with a pass energy of 100 kV and a step size of 1 eV. High resolution XPS spectrums were acquired for the Co 2p peaks using a pass energy of 50 kV and a step size of 0.1 eV. To account for sample charging, spectra were calibrated by setting the adventitious carbon peak to 284.7 eV. High resolution XPS spectra were de-convoluted with CasaXPS software.

### *5.2.8 SQUID Characterization*

Powder sample magnetization measurements were carried out for magnetic fields – 50 kOe < H < + 50 kOe at 300 K. Measurements were conducted using a Quantum Design MPMS-5 superconducting quantum interference device (SQUID) magnetometer.

*5.2.9 Cobalt Quantification*

Cobalt content in each of the respective powder types (pure HA, CoHA synthesized via ion exchange, and CoHA synthesized directly via wet synthesis) was quantified using a colorimetric method with nitroso-R salt (Acros, pure), which forms a red colored compound with cobalt under appropriate conditions. The powders were dissolved in HCl and mixed with nitroso-R in the presence of a sodium citrate buffer (Fisher, 99+%), and then the concentration of cobalt in the solution was determined using a standard curve of known concentrations developed using a plate reader (Biotek MQX200) to measure absorbance at 500 nm.

*5.2.10 Degradation Study*

CoHA powders of both types, as well as HA, were uniaxially pressed into pellets using a bench top laboratory press (Carver Model C). For each pellet, 0.25 g of powder was pressed into a 13 mm pellet die well lubricated with stearic acid (97%, Acros) in acetone (99.9%, J.T. Baker) at a pressure of 100 MPa for 10 seconds. Un-sintered CoHA pellets were subjected to a dynamic (shaking) degradation study in simulated body fluid (SBF) at 37°C and 50 rpm. The simulated body fluid prepared for this test was 1xSBF. Table 5.1 lists the ion concentrations of different reagents in SBF, which are compared with those in human blood plasma [120]. However, the composition of this SBF is slightly different from the commonly used SBF. In our study, phosphate containing salt was removed in order to prevent formation of a calcium phosphate coating on the CoHA pellets, as the purpose of the study was to determine degradation behavior and not the effect of the substitution on biomineralization. Reagents were added in order; NaCl (Fisher, >95%), $MgCl_2$-$6H_2O$ (Fisher, 99.9%), HEPES buffer (Fisher, 99%), $CaCl_2$ (Fisher, >95%), and $NaHCO_3$ (Fisher, 99%), ensuring that the previous reagent was completely dissolved

before adding the next. The pH of the SBF was adjusted to 7.4 prior to immersing each pellet into 10 mL of SBF for the degradation study.

**Table 5.1** Comparison of ion concentrations of different elements in SBF and human blood plasma

| **Ion** | **Concentration in 1xSBF (mM)** | **Concentration in blood plasma (mM)** |
|---|---|---|
| $Na^+$ | 109.5 | 142 |
| $Mg^{2+}$ | 1.5 | 1.5 |
| $Ca^{2+}$ | 2.5 | 2.5 |
| $Cl^-$ | 110.0 | 103.0 |
| $HCO_3^-$ | 17.5 | 27.0 |
| $K^+$ | 0 | 5.0 |
| $SO_4^{2-}$ | 0 | 0.5 |
| $HPO_4^{2-}$ | 0 | 1.0 |

A total of 18 pellets of each powder type were used for this experiment, with 3 pellets of each type examined at each time point, 1 day, 3 days, 1 week, 2 weeks, 3 weeks and 4 weeks. The SBF was collected and separated from the pellet for each time point using a pipette and placed into clean vials, and pH and cobalt content were measured using a pH meter (Accumet XL15 pH meter) and spectrophotometry (Biotek MQX200) with nitroso-R, respectively. Absorbance of each collected sample solution was measured in duplicate at a wavelength of 500 nm. A standard curve, prepared from known concentrations of cobalt chloride in SBF, was used to calculate the concentration of cobalt released from the pellets at each time point. The

degraded pellets were sputter coated for 1 minute with gold palladium and their surface morphologies were examined via FESEM using 10 kV accelerating voltage.

*5.3 Results*

*5.3.1 EDX Characterization*

The presence of cobalt in each of the CoHA sample powder types was confirmed using EDX. EDX spectra of CoHA via ion exchange and via wet synthesis are shown in Fig. 5.1. EDX confirmed that there is cobalt present in small amounts (about 5 atomic % or less) in both CoHA powder samples.

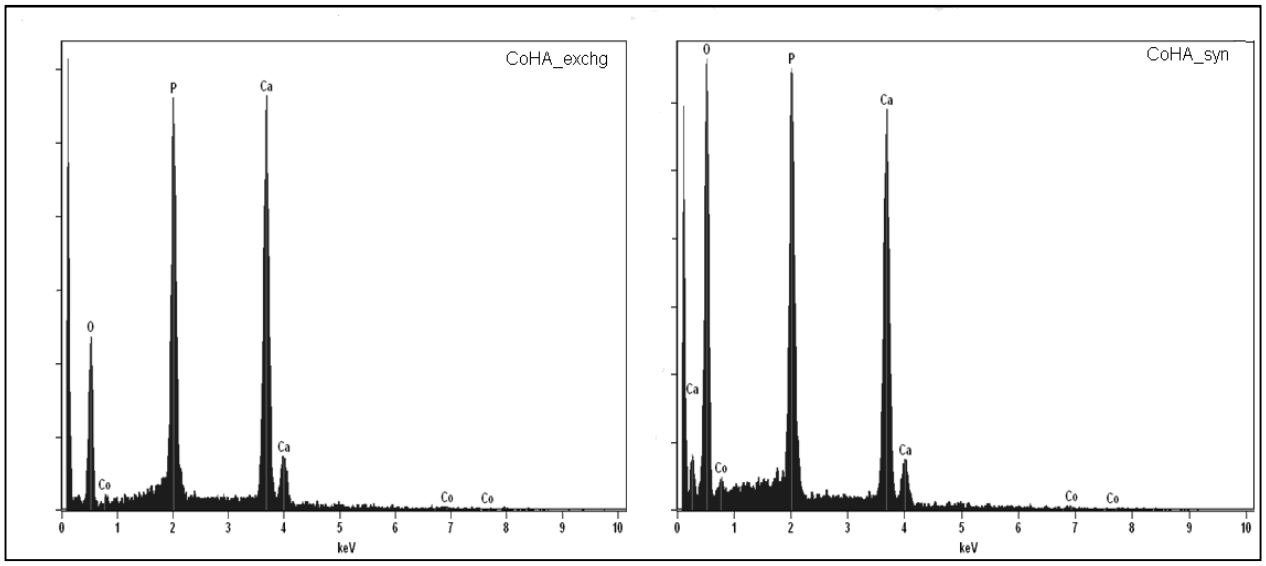


**Figure 5.1** EDX spectra of CoHA via ion exchange (left), and CoHA via wet synthesis (right).

*5.3.2 FESEM Analysis of Powder Morphology.*

FESEM imaging was used to compare the particle morphology of HA, CoHA via ion exchange, and CoHA via wet synthesis. Representative micrographs of each powder type are

shown in Fig. 5.2. All three powder types consist of rod-shaped particles, largely with lengths of about 100-400 nm, and widths of about 25-60 nm. Image-J measurements of each powder type are summarized in Table 5.2. HA has the largest average length, at 284 nm. There is also the greatest deviation between lengths for HA compared to the CoHA powders. CoHA via ion exchange and CoHA via wet synthesis have similar average lengths, of 205 nm and 209 nm, respectively. Average widths are all comparable, at 45, 47, and 44 nm for HA, CoHA via ion exchange, and CoHA via wet synthesis. All HA and CoHA nanoparticle types are agglomerated even after sonication.

**Table 5.2** Image-J measurements of HA and CoHA powder sizes

| Powder type | Length measurements (nm) | | Width measurements (nm) | |
|---|---|---|---|---|
| HA | Mean | 284 | Mean | 45 |
| | STD | 96 | STD | 9 |
| | Min. | 79 | Min. | 26 |
| | Max. | 440 | Max. | 60 |
| CoHA via ion exchange | Mean | 205 | Mean | 47 |
| | STD | 56 | STD | 13 |
| | Min. | 138 | Min. | 24 |
| | Max. | 342 | Max. | 62 |
| CoHA via wet synthesis | Mean | 209 | Mean | 44 |
| | STD | 71 | STD | 13 |
| | Min. | 108 | Min. | 24 |
| | Max. | 347 | Max. | 63 |

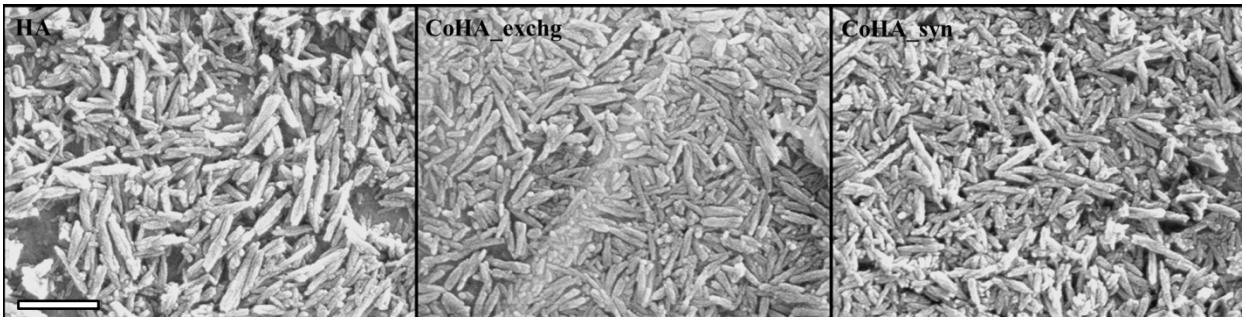


**Figure 5.2** FESEM micrographs of HA, CoHA via ion exchange, and CoHA via wet synthesis. The scale bar represents 500 nm.

*5.3.3 XRD Pattern Analysis and Comparison of HA and CoHA*

The XRD patterns of synthesized HA and CoHA synthesized via both ion exchange and wet synthesis from 10-90° 2θ are shown in Fig. 5.3. All patterns are in agreement with the hexagonal HA reference pattern, JCPDS card number 9-432. There are no notable diffraction peaks present in any of the spectra that are not attributed to HA, and no obvious changes in relative peak intensities between the various apatite peaks after ion exchange were observed. Since none of the three powders are calcined, we see poor crystallinity in all three powder samples. Although the apatite crystal structure was maintained without any second phase detected, the CoHA samples showed peak broadening and decrease in intensity, occurring to a greater extent in the CoHA sample synthesized via wet synthesis as compared to the CoHA synthesized via ion exchange. According to the XRD spectra neither CoHA sample powder type contained any obvious second phases.

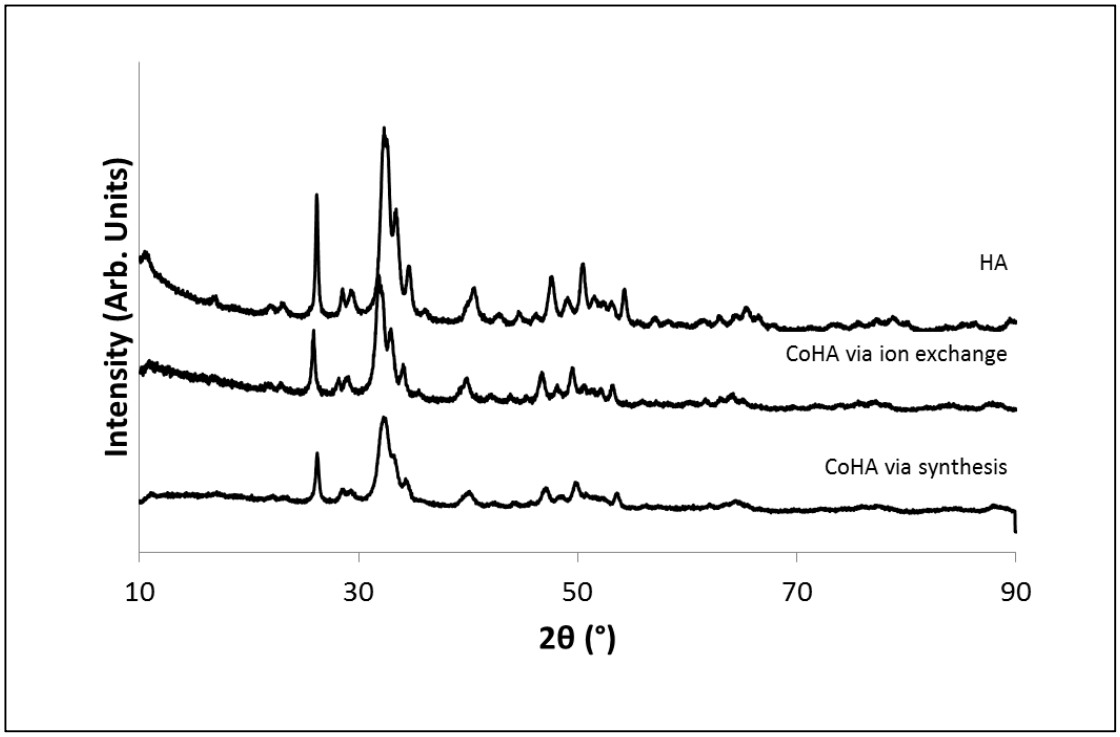


**Figure 5.3** XRD spectra for HA, CoHA synthesized via ion exchange, and CoHA synthesized via wet synthesis.

*5.3.4 FT-IR Analysis of the Molecular Structure of HA and CoHA*

Fourier transform infrared spectroscopy was conducted on pure HA control powder, as well as both CoHA powder types. The FT-IR spectra, in Fig. 5.4, show that there is no significant difference between the HA and the CoHA via wet synthesis samples. Each peak can be assigned to a characteristic peak of hydroxyapatite. Peaks between 660-520 $cm^{-1}$ as well as around 1040 $cm^{-1}$ are attributed to phosphate groups. There are carbonate peaks between 1650-1300 $cm^{-1}$, and also an obvious hydroxyl bending mode around 3570 $cm^{-1}$. There are no peaks appearing in the CoHA sample spectra that cannot be identified as peaks corresponding to functional groups found in pure HA. This further indicates that the CoHA via wet synthesis sample type maintained a similar structure to the pure HA. The CoHA synthesized via ion

exchange, on the other hand, has a small extraneous doublet peak between 2400 and 2300 $cm^{-1}$. $CO_2$ has a characteristic absorption doublet around 2350 $cm^{-1}$ that may be the source of the extraneous peak in the CoHA via ion exchange spectra.

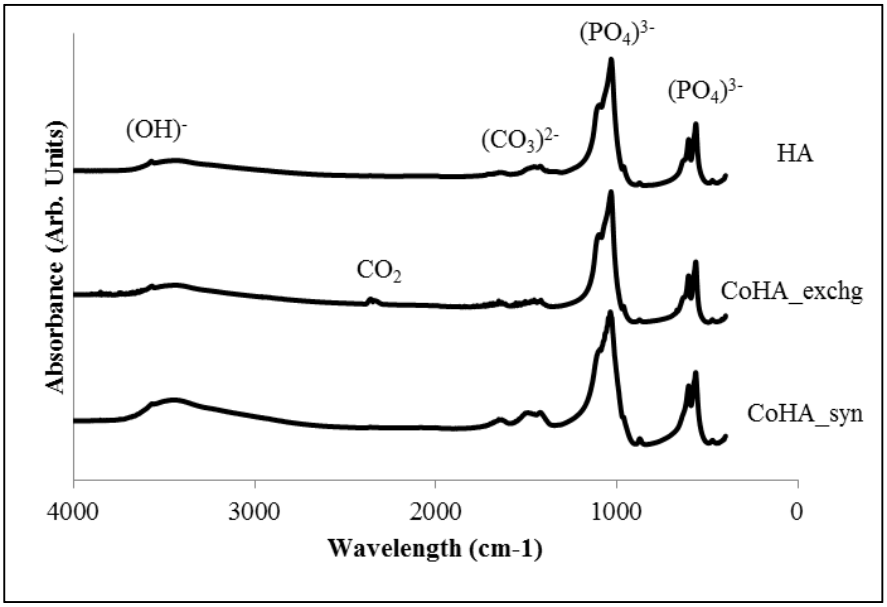


**Figure 5.4** FT-IR spectra for HA, CoHA synthesized via ion exchange, and CoHA synthesized via wet synthesis. Labels on the HA spectrum also apply to the identical peaks in the CoHA spectra.

*5.3.5 XPS Characterization*

The survey scans revealed the presence of C, O, Ca, Co and P in both CoHA via wet synthesis and CoHA via ion exchange. High resolution spectra of the Co 2p peaks (Fig. 5.5) revealed multiple peaks for CoHA prepared by ion exchange and wet synthesis. For CoHA via wet synthesis peaks are observed around 782.93, 788.20, 799.14, and 804.89 eV. The peaks at 782.93 and 799.14 are the 2p peaks pairs from spin orbit splitting, 2p 3/2 and 2p 1/2, these positions correspond well with $Co^{2+}$ in the HA lattice which has been previously observed in the

range of 782.3-783 eV [121]. The spin orbit splitting of the peaks is 16.2 eV which is characteristic of $Co^{2+}$ [121]. The peaks at 788.20 and 804.89 are also 2p peak pairs from spin orbit splitting but are a shakeup satellite of $Co^{2+}$. The strong nature of the shakeup satellite can be attributed to the $Co^{2+}$ oxidation state with paramagnetic properties [122]. The CoHA via ion exchange spectrum has observed peaks similar to CoHA synthesis with peaks observed at 781.56, 787.34, 797.33, and 803.47 eV. The peak pairs at 781.56 and 797.33 are attributed to $Co^{2+}$ in the HA lattice; the spin orbit splitting of 15.7 eV is further indication of the $Co^{2+}$ oxidation state.

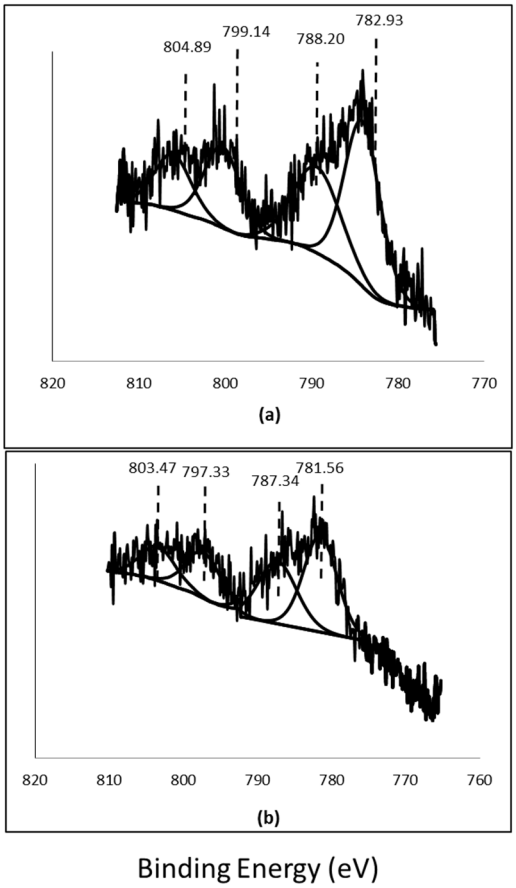


**Figure 5.5** XPS response of Co 2p in CoHA (a) via wet synthesis and (b) via ion exchange.

*5.3.6 Magnetic Properties of CoHA by SQUID Analysis*

The magnetization of CoHA via ion exchange and wet synthesis were measured at 300 K between -50 and 50 kOe magnetic fields as shown in Fig. 5.6. Both CoHA sample types were shown to have paramagnetic properties by the positive slope of the magnetization-magnetic field curve. This is in contrast to pure HA, which has diamagnetic properties [97].

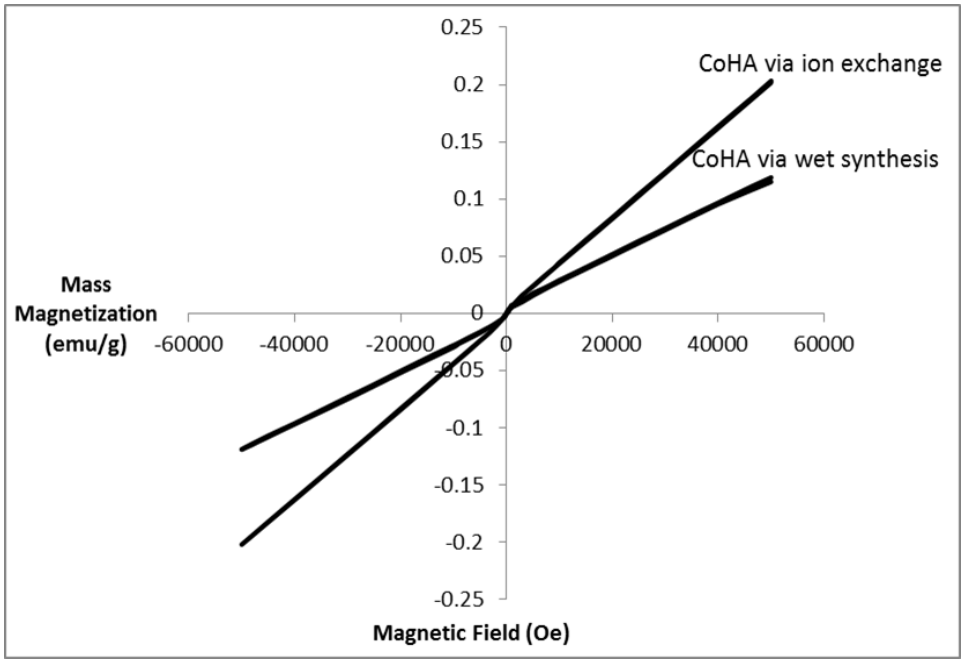


**Figure 5.6** Mass magnetization measurements of HA, CoHA via ion exchange, and CoHA via wet synthesis.

*5.3.7 Co Quantification*

The cobalt concentration in SBF was measured using spectrophotometry, and is expressed as g Co/ g CoHA. The cobalt concentration is higher in the CoHA powder obtained

via wet synthesis than the powder obtained via ion exchange, and the values are 0.063 g Co/ g CoHA and 0.045 g Co/ g CoHA, respectively.

*5.3.8 Degradation Study*

CoHA sample pellets and HA control pellets were soaked in 1xSBF at 37°C and 50 rpm in a shaking water bath for up to a month. Samples were removed at 1 day, 3 days, and one week intervals from 1 to 4 weeks and the SBF they had been soaking in were analyzed. Both the pH and the concentration of cobalt present in the SBF were measured at each time point. Cobalt concentration was immeasurably low for all time points for HA samples. Fig. 5.7 is a plot of the average pH for each soaking time point.

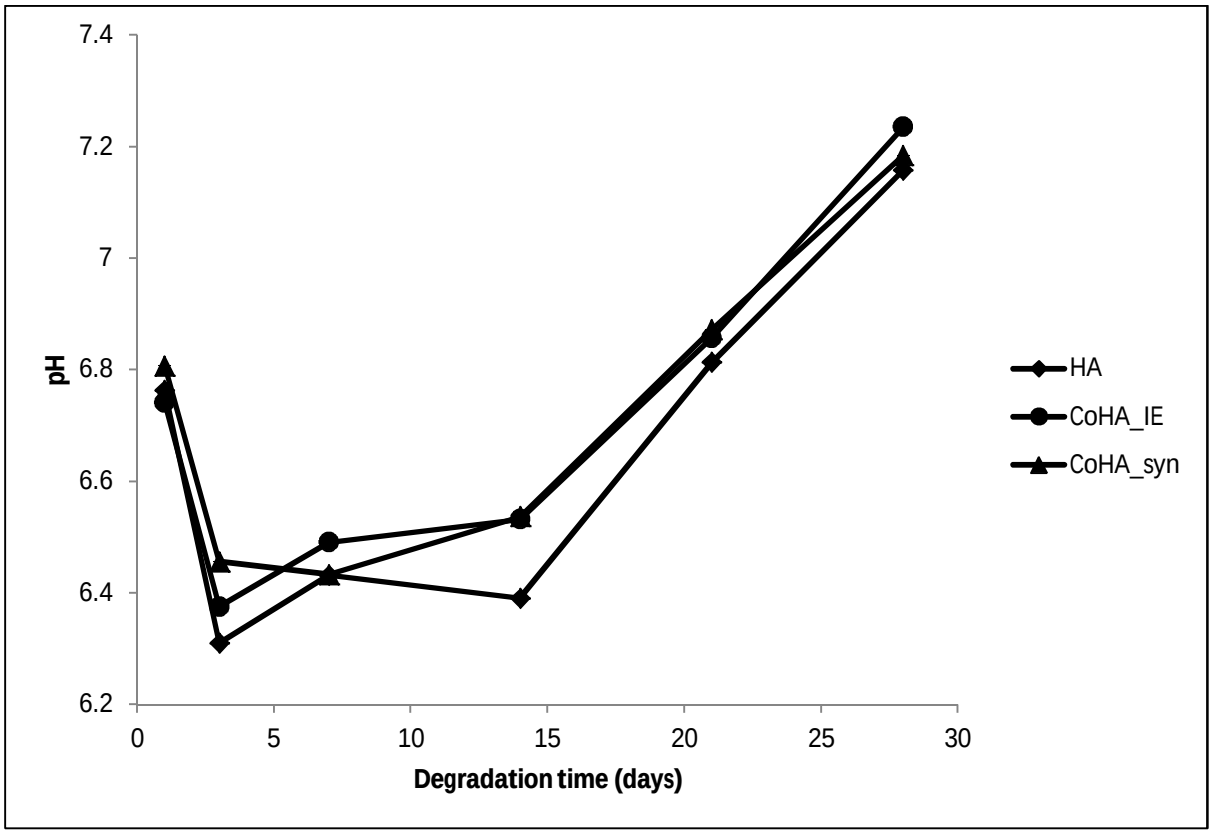


**Figure 5.7** pH as a function of pellet soaking time in a degradation study.

Initially, pH decreased sharply from 7.4 to 6.76, 6.74, and 6.81 for HA, CoHA via ion exchange, and CoHA via wet synthesis. At day 3 the pH of the SBF further decreased to 6.31, 6.38, and 6.46. After 1 week the pH of the SBF had an average value of 6.43 for HA pellets, 6.49 for ion exchange pellets and 6.43 for CoHA pellets synthesized via wet synthesis. At two weeks, the average pH values remained roughly the same for the three sample groups, at 6.39, 6.53, and 6.54, respectively. At 3 and 4 weeks of soaking, pH has a steadily increasing trend. For HA pellets, the pH increased to 6.81 at 3 weeks and then further increased to 7.16 at 4 weeks. For CoHA via ion exchange and via wet synthesis the pH increased to 6.86 then 7.23, and 6.87 then 7.18.

In Fig. 5.8, cobalt ion concentration in the SBF is plotted as a function of soaking time. The concentration of cobalt in the SBF was measured and is reported in terms of cobalt released per gram of CoHA sample powder. SBF was also collected from HA degradation samples and measured for cobalt content, but the resulting cobalt concentration was essentially zero, below the range that could be measured using this test (about 10 μg/mL). The amount of cobalt ions accumulated in the SBF over the course of the one-month degradation study ranged from hundreds (in the case of CoHA via wet synthesis after 1 day) to thousands of micrograms per gram of powder. At every time point there was less cobalt ion accumulation in the SBF containing CoHA via wet synthesis than the SBF containing CoHA via ion exchange. The degradation of CoHA via synthesis resulted in an increase in cobalt content in SBF from about 920 μg/ g CoHA after 1 day of soaking to about 2130 μg/ g CoHA at 2 weeks. The total amount of ionic cobalt accumulated in the SBF then decreased at 3 and 4 weeks of degradation down to about 1024 μg/ g CoHA at 4 weeks. CoHA via ion exchange increased from about 1630 μg/ g

CoHA at day 1 to a peak value of about 3662 µg/ g CoHA at 3 weeks. Cobalt content in the SBF then decreased to about 1838 µg/ g CoHA after 4 weeks of CoHA degradation in SBF.

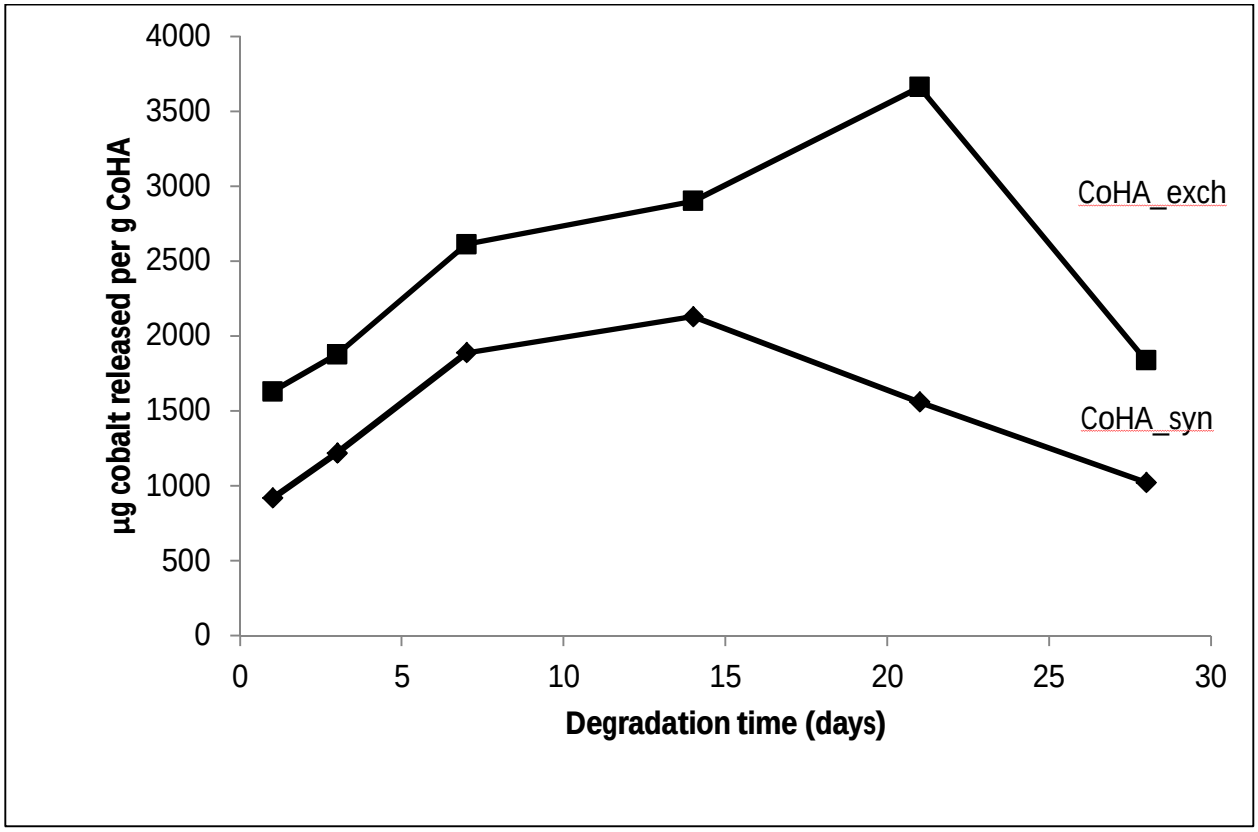


**Figure 5.8** Cobalt concentration in SBF collected during a degradation study.

Pellet morphology pre- and post-degradation was examined. CoHA via wet synthesis was selected as representative, and the morphology change over a 4 week degradation study is shown in Fig. 5.9. All three pellet types displayed comparable morphology changes over the course of the degradation study. Prior to degradation, all pellets were smooth, with HA pellets being white and CoHA bright purple. Through one week of degradation, pellet appearance remains the same. After 2 and 3 weeks the pellets have begun to break apart, with severe breakage occurring by 4 weeks of soaking. The intensity of the purple color in the CoHA pellets also decreases from 2 to 4 weeks. FESEM micrographs in Fig. 5.9 show a homogenous, clean

surface before degradation. After 4 weeks of degradation, the pellet surface is less homogenous. There are areas of pitting and a large amount of detached debris on the surface of the pellets.

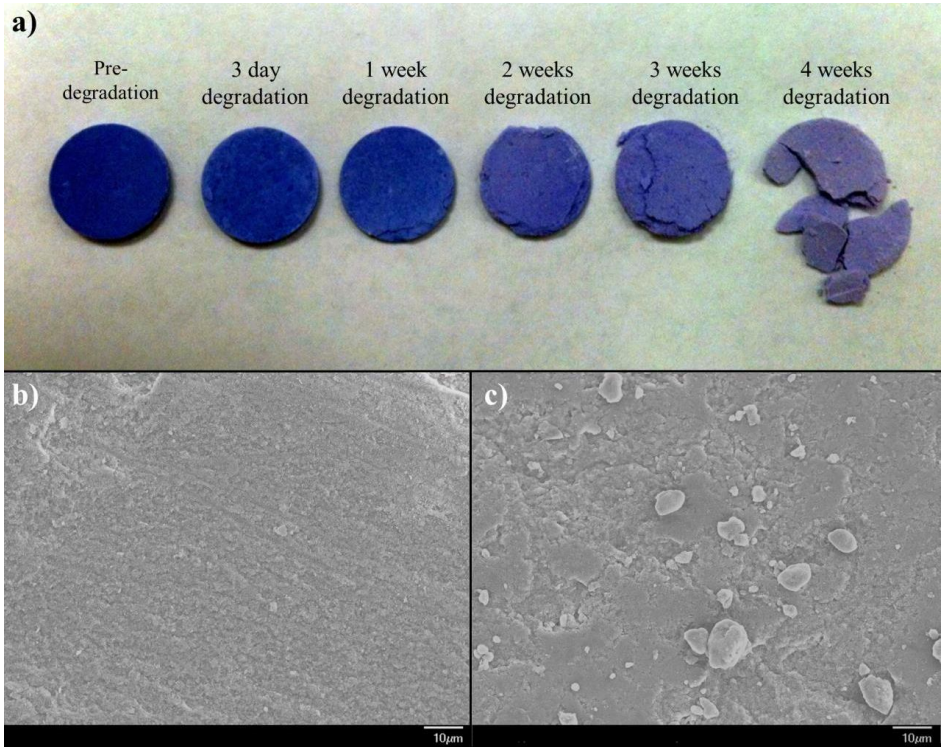


**Figure 5.9** Photograph of CoHA via wet synthesis pellets after degradation (a) and FESEM micrograph of CoHA via wet synthesis pellet morphology before degradation (b) and after 4 weeks (c) of degradation.

*5.4 Discussion*

CoHA is not a widely studied material. It has previously been synthesized via a hydrothermal procedure by Stojanovic et al. and Veselinovic et al. as a material with great potential in both catalytic and biomedical applications [112, 113]. Preliminary studies in osteoporotic alveolar bone tissue in the lower jaw of female Wistar rats have shown positive results in osteoporotic bone tissue regeneration. CoHA with 12 wt% cobalt resulted in improved

tissue regeneration compared to pure HA [123]. However, despite the success of this study, the scope of research on CoHA available in the literature is limited. As a material with paramagnetic properties, CoHA may be applied to a wide range of biomedical applications, and therefore further study of CoHA and detailed characterization of its properties is worthwhile.

In this chapter, HA and CoHA were synthesized. CoHA was synthesized via two distinct methods. In both cases, CoHA via ion exchange and via wet synthesis, the resulting powder was purple, whereas pure HA power was white. Based on EDX results, cobalt was present in small quantities in both CoHA powder types. Cobalt levels were quantified as being about 0.063 g/ g Co in CoHA via wet synthesis and 0.045 g/ g Co in CoHA via ion exchange. The CoHA via wet synthesis contained a greater amount of cobalt than that synthesized via ion exchange, even though a higher initial concentration of cobalt is used in the ion exchange procedure. There may be greater cobalt content in the powder synthesized via wet synthesis, as opposed to ion exchange, because the ion exchange procedure limits substitution to predominantly surface calcium sites, as opposed to potential bulk substitutions that may be occurring during wet synthesis. Ion exchange is a predominantly surface reaction because in aqueous conditions a hydrated layer of loosely bound mineral ions exists in HA, and these loosely bound ions can be easily exchanged [48]. Additionally, in acidic conditions, the $Ca^{2+}$ ions dissociate from the apatite crystal lattice at the surface of the HA particle [46, 47], further facilitating an exchange between the $Ca^{2+}$ ions in the apatite lattice and the $Co^{2+}$ ions in solution due to calcium deficient HA being particularly subject to ionic substitutions [95]. The combined loosely bound and calcium deficient nature of the outer layer of HA particles in acidic aqueous conditions make it highly likely that the majority of $Co^{2+}$ will substitute into the surface regions of HA in ion exchange. Evidence was presented supporting this mechanism for ion exchange being limited to

surface and near surface lattice sites in FeHA (Chapter 3), and the concept can be applied to CoHA as well.

The goal of this study was to achieve a single-phase CoHA after substitution without any formation of impurities or a cobalt-oxide second phase. Single phase is desirable because phase purity influences the bioactivity and *in vivo* behavior of bioceramics [91]. In addition to obtaining an apatite structured material, it was also desirable to synthesize a material with paramagnetic properties.

XRD results indicate that a single-phase substituted powder was achieved due to the fact that no obvious differences were observed between HA and CoHA spectra, shown in Fig. 5.3. A formation of a second phase would have resulted in extraneous peaks in an XRD analysis. However, XRD data did show broadened diffraction patterns in CoHA as compared to HA. This peak broadening and decrease in intensity is more severe in the CoHA via wet synthesis than in the CoHA via ion exchange. A decrease in peak intensity and an increase in peak broadening indicate a material with more amorphous character. A more amorphous substituted HA versus the pure HA is consistent with results seen in previous work done with FeHA [97]. The CoHA via wet synthesis may be more amorphous than the CoHA via ion exchange due to the higher amount of cobalt present in the material. This also mimics the trend seen in our previous work with FeHA [97]. XPS spectra confirmed that $Co^{2+}$ was successfully incorporated into the HA lattice in both CoHA via wet synthesis and CoHA via ion exchange.

FT-IR results also indicate, by the absence of extraneous peaks, that there was no second phase formation in the CoHA via wet synthesis sample. The CoHA material synthesized via ion exchange, however, shows an extraneous doublet peak around 2350 $cm^{-1}$ that is not present in the pure HA or HA via wet synthesis spectra. A doublet around 2350 $cm^{-1}$ can be attributed to

$CO_2$ adsorption. An explanation for why there would be increased $CO_2$ adsorption in the CoHA via ion exchange powder as compared to the other powder tested is that the amount of $CO_2$ adsorbed by HA differs with varying surface compositions [124]. Since the ion exchange procedure in a slightly acidic cobalt chloride environment likely occurs via a mechanism that results in predominantly surface substitutions [46, 47], the surface composition of this material potentially has a significantly different surface composition than HA or CoHA via wet synthesis, and thus lends itself to a greater amount of $CO_2$ adsorption. The acidic environment in which the ion exchange procedure occurs also provides an explanation for why the size of the CoHA via ion exchange particles are smaller than those of the starting pure HA particles, decreasing from an average length of 284 nm to an average length of 205 nm. HA dissolves in aqueous acidic solutions, and as such the acidic nature of the cobalt chloride soaking solution may result in partial apatite dissolution and decreased particle size. Fig. 5.10 shows a pH curve of the ion exchange procedure for preparation of CoHA. At time=0, the initial pH of the cobalt chloride solution is 5.817. At time=1 minute, once HA is added to the system, the pH increases to 6.172. This pH jump may be caused by the partial dissolution of HA and the resulting release of hydroxyl groups into the solution. For the rest of the 1 hour soaking time the pH remains roughly constant between 6.04 and 6.07.

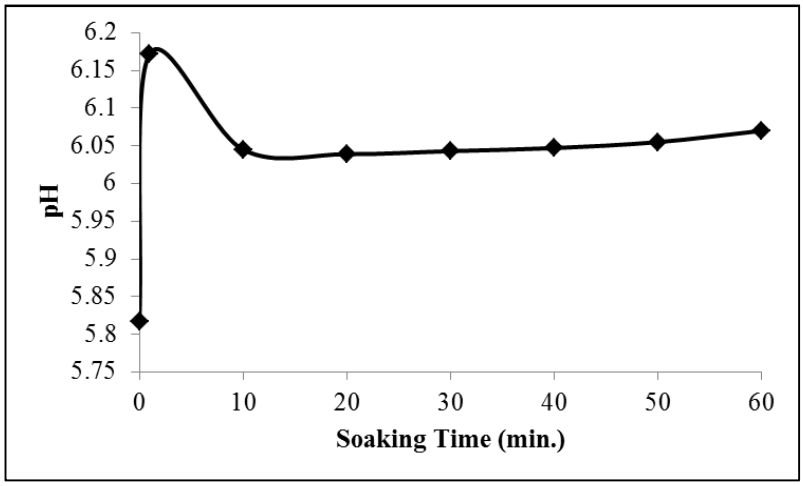


**Figure 5.10** pH curve of the one-hour cobalt ion exchange procedure at room temperature.

SQUID measurements prove that a material with an apatite crystal structure and a small amount of cobalt substituted into the lattice will yield a paramagnetic material. The magnetic susceptibilities for both CoHA materials, determined by taking the slope of the magnetization plot, are on the same order of magnitude, with susceptibilities of $4x10^{-6}$ emu/(g*Oe) for the CoHA via ion exchange and $2x10^{-6}$ emu/(g*Oe) for the CoHA via wet synthesis. The presence of cobalt gives each material paramagnetic properties, but there seems to be no distinct pattern between the total cobalt content and the magnetization.

The preceding characterizations determined that cobalt substituted HA with magnetic properties can be achieved, but in order to use such a material in biomedical applications toxicity concerns need to be addressed. The results from the degradation study that was conducted indicate that very small amount of cobalt is released after allowing CoHA to degrade for 4 weeks. The pH of the surrounding environment initially decreases during early time points of degradation. This pH decrease over the first 3 days of the study is likely due to the fact that the pellets were pressed in a stearic acid lubricated die. As the residual stearic acid is released from the pellet surfaces to the SBF the pH of the SBF changes accordingly. Typically, the apatite will

be used in powder form for applications such as drug delivery, cancer hyperthermia, or as a MRI contrast agent, in which case stearic acid would not be added. In applications in which the apatite is used in bulk form, it would be sintered, in which case the stearic acid be coated onto the surface of the pellet but will have burned off. Therefore, the pH change of CoHA used for a biomedical application might be much smaller in reality than the values presented here. The increase seen at time points after 2 weeks likely results from the release of hydroxide groups as the bulk apatite material begins to degrade. Significantly, the overall pH profile for the CoHA materials mimics the pH profile for the pure HA, indicating that the small amounts of cobalt present in the sample materials are not high enough to greatly affect the degradation behavior of the apatite or cause local acidic conditions. The amount of cobalt ions released into the SBF was measured quantitatively, and found to be low. The quantification of cobalt in SBF revealed some interesting behavior. Although the CoHA via wet synthesis has higher total initial cobalt content, the amount of cobalt released into the SBF is greater in the CoHA via ion exchange samples. This is likely due to the fact that a higher percentage of cobalt ions are located on the surface of the CoHA via ion exchange and are released more rapidly than bulk substituted cobalt (such as in CoHA via wet synthesis), which requires degradation of an entire CoHA particle to release the majority of its cobalt content. Furthermore, after 2 weeks soaking time for CoHA via synthesis and 3 weeks for CoHA via ion exchange, the amount of cobalt accumulated in the SBF decreases despite the decreased intensity of the purple pellets, as seen in Fig. 5.9, indicating continued cobalt release with time. The apparent decrease in cobalt in the SBF is probably a result of simultaneous HA degradation. As the HA degrades it releases hydroxide groups, resulting in the increase in pH seen in Fig. 5.7. It also releases phosphate groups, which will easily react with cobalt ions to form cobalt phosphate precipitates. These precipitates will thus

fall out of solution, decreasing the amount of loose cobalt ions in SBF. This behavior makes it difficult to determine exactly how much cobalt would be released from our sample powders after a month, but it is also reflective of conditions in the human body.

In the case of CoHA via ion exchange, it seems there is an early "burst release" of cobalt, with day 1 cobalt levels being about 1631 μg/ g CoHA. After 3 days, however, only about an additional 250 μg of cobalt is present in this SBF per gram of CoHA. After this burst release, the release of cobalt is on the order of 100 μg/ day/ g CoHA. This means that in a one month time period less than 10% of the total cobalt content in the pellet will be released. CoHA via wet synthesis has a similar behavior pattern, but the initial burst release is about 919 μg/ g CoHA, an order of magnitude lower than that of the CoHA via ion exchange.

An average person intakes about 300 μg of cobalt per day and a 70 kg adult has a total body burden of about 1.5 mg cobalt [118]. Furthermore, excess cobalt, in reasonable levels, can be excreted by the kidneys. Therefore, this rate of cobalt release should be low enough for the body to be able to clear with minimal toxic effect, assuming a CoHA dose comparable to the 250 mg used in this study. This is a reasonable dose assumption to make for potential biomedical applications. For example, in cancer hyperthermia it is expected that 5-10 mg of material per $cm^3$ of tumor tissue will be a therapeutically effective dose [68]. The dose of CoHA used in this study would, therefore, be enough to treat a 25 $cm^3$ tumor.

### *5.5 Conclusions*

Using a cobalt chloride solution and a simple soaking procedure, we were able to prepare CoHA with no apparent formation of a second phase, as verified by XRD and FT-IR characterization. Incorporation of cobalt during the HA wet synthesis procedure was also

accomplished. In the case of CoHA via ion exchange, the cobalt likely occupies calcium sites at and near the apatite particle surface. For CoHA via wet synthesis cobalt may be present in bulk calcium sites. The substitution of small amounts of $Co^{2+}$ into the HA lattice results in CoHA powders with paramagnetic properties. As indicated by degradation study results, the amount of cobalt released from these CoHA particles should not result in a high concern of toxicity. After further study, CoHA may be an attractive apatite based magnetic material to be applied to future biomedical applications.

# Chapter 6

## A comparative study of the sintering and cell behavior of pure and cobalt-substituted hydroxyapatite

### *6.1 Introduction*

Biomaterials are widely studied for applications related to traditional medical devices, diagnostic products, smart drug delivery systems, and tissue engineering and regenerative medicine systems. Biomaterials research takes advantage of developments in traditional materials science fields, but is also concerned with the biocompatibility and biofunctionality of candidate biomaterials [125]. The ceramic class of biomaterials has been studied in the past particularly for use in applications in bone augmentation and replacement [5, 125]. Ceramic powder properties, such as crystallinity, surface area, and particle size, determine their effectiveness for specific applications. Additionally, powder properties and chemical composition affect material sinterability [98]. A study of a ceramic's sintering behavior can provide insight into material stability and bulk mechanical properties, thereby determining which applications are appropriate for the material.

Previous chapters have dealt with the substitutions of both iron and cobalt into the HA lattice. A sintering study was also presented for FeHA, in order to illuminate information regarding the stability and mechanical properties of FeHA, and thus predict what types of applications the material may be used for.

There have been limited studies recently on the substitution of cobalt into the HA lattice where careful analysis was conducted on the crystal structure of the resulting material, but limited results were reported regarding the effect that cobalt substitution had on other material

properties including sintering behavior [112, 113]. The objective of this chapter is to provide a systematic study of the sintering behavior and corresponding mechanical properties at a series of temperatures, to determine the appropriateness of CoHA for various types of biomedical applications. *In vitro* biocompatibility was also assessed via cell culture.

## *6.2 Materials and Methods*

### *6.2.1 Hydroxyapatite and Cobalt-substituted Hydroxyapatite Synthesis*

Hydroxyapatite powder was prepared via a wet precipitation procedure in which an aqueous solution of 2 g/dL ammonium phosphate (99+%, Acros) was added dropwise at a moderate dropping rate of about 75 drops per minute under vigorous stirring to a 2 g/dL aqueous calcium nitrate tetrahydrate (99%, Fisher) solution at 75°C. Ammonium hydroxide (~30%, Fisher) was also added to the phosphate containing solution to bring up the pH to 11-12. After 3 hours of stirring at 75°C, the HA particles were collected by filtration and washed thoroughly with deionized water. The collected HA precipitates were dried at 90°C for 12-16 hours and ground by mortar and pestle into a fine powder.

Cobalt was incorporated during HA synthesis using the synthesis procedure as described above. A quantity of cobalt (II) chloride that would allow for 10% substitution was added to the phosphate-containing solution. The rest of the synthesis was conducted exactly as described for pure HA. The CoHA powder obtained via wet synthesis that was to be used for cell culture was then sterilized with 70% ethanol and used as is. The resulting powders to be used for the sintering study were milled (SPEX 8000 Mixer/Mill) for 10 minutes in a steel canister with alumina milling balls.

Cobalt was also incorporated via ion exchange for use in the cell culture study. HA powder was subjected to a simple soaking procedure to achieve cobalt substitution for calcium in the HA crystal lattice. HA powder was soaked in a cobalt chloride solution at a concentration of 0.02 M under moderate stirring for one hour at room temperature, and then collected by filtration and washed by deionized water. The resulting powder was dried and ground manually, and the sterilized with 70% ethanol.

*6.2.2 Pellet Preparation and Sintering*

Milled HA and CoHA powders were uniaxially pressed into pellets using a bench top laboratory press (Carver Model C). For each pellet, 0.35 g of powder was pressed into a 13 mm pellet die well lubricated with stearic acid (97%, Acros) in acetone (99.9%, J.T. Baker) at a pressure of 150 MPa for 10 seconds. The resultant HA pellets had a thickness of approximately 1.63 mm and the CoHA pellets had a thickness of 1.80 mm.

Pellets were sintered at a selection of temperatures for each sample type using a ramp rate of 5°C per minute and soaked at peak temperature for 2 hours in a chamber furnace (CM, 1610FL). The sintering temperatures used were 900, 1000, 1100, 1200, and 1300°C for the HA samples, and 700, 800, 900, 1000, 1100 and 1200°C for the CoHA samples. Lower sintering temperatures were selected for the CoHA samples after preliminary results for samples run at the same temperatures as pure HA indicated that decomposition began for CoHA at temperatures below 900°C. A total of 10 pellets of each type of powder were sintered for each temperature point investigated.

*6.2.3 Starting Powder Characterization*

The starting powder was characterized in Chapter 5 using energy dispersive X-ray spectroscopy (EDX) to verify the presence of cobalt in the sample powders. A Thermo Noran EDS detector coupled to a JEOL JSM 6335 field emission scanning electron microscope (FESEM) was used for chemical analysis. Powder samples of HA and CoHA were examined using a Bruker D2 Phaser X-ray diffractometer with a copper target, and voltage and current conditions of 40 kV and 40 mA, respectively. Conditions used were a 0.02° 2-theta step size and a scan speed of 4 °/min with a 2-theta range of 10-90. XRD was used to analyze sample crystal structure. Additionally, a Niclotet Magna 560 Fourier Transform Infrared (FT-IR) Spectometer was used to compare the functional groups of pure HA and the CoHA samples. This characterization was carried out using classic KBr pellet technique in a transmission mode. Each FT-IR spectrum was the average of 32 scans with a resolution of 4.0 $cm^{-1}$ in the range of 400-4000 $cm^{-1}$. CoHA powder magnetic properties were analyzed using a Quantum Design MPMS-5 superconducting quantum interference device (SQUID) magnetometer. Powder sample magnetization measurements were carried out for magnetic fields – 50 kOe < H < + 50 kOe at 300 K.

*6.2.4 Density and Biaxial Flexural Strength*

Density measurements were performed on green and sintered pellets using an Ohaus digital balance accurate to 1 mg and a caliper (Mitutoyo) accurate to 0.01 mm. Three diameter and three thickness measurements were taken for each of the 10 pellets sintered at each temperature and the respective averages were used when calculating pellet density. A Tinius Olsen (150KS model) was used to determine the pellet biaxial flexure strength (modulus of

rupture) on 13 mm diameter pellets (n=8) using a 1000 N load cell at a crosshead speed of 0.01 mm/minute and a pin-on-disc test fixture set up per ASTM F 394 [103]. The modulus of rupture (MOR) was calculated based on the following equations:

$$S = -0.2387\ P(X-Y)/d^2 \quad (1)$$

where S = maximum center tensile stress (MPa), P = total load causing fracture (N),

$$X = (1+\nu)\ \ln[(B/C)^2] + [(1-\nu)/2](B/C)^2, \quad (2)$$

$$Y = (1+\nu)[1+\ln[(A/C)^2]] + (1-\nu)(A/C)^2, \quad (3)$$

where $\nu$ = Poisson's ratio, 0.27, A = radius of support circle (mm), B = radius of loaded area or pin tip (mm), C = radius of specimen (mm), and d = specimen thickness at point of fracture (mm).

### *6.2.5 XRD Characterization*

As-prepared HA and CoHA, and those sintered at different temperatures were examined for phase purity and crystal structure using a Bruker D2 Phaser X-ray diffractometer (XRD) with a copper target, and voltage and current conditions of 40 kV and 40 mA, respectively. Conditions used were a 0.02° 2-theta step size and a scan speed of 4°/min with a 2-theta range of 10-60.

### *6.2.6 FESEM Characterization*

Field emission scanning electron microscopy (FESEM) was used to examine the cross-section morphology of sintered pellets with an accelerating voltage of 10 kV. Ruptured pellets from the MOR test were used for FESEM imaging. Pellet cross-sections were left unpolished and sputter coated with gold palladium for 1 minute prior to imaging at 10,000x.

*6.2.7 Cell Culture Study*

The biocompatibility of CoHA was assessed through cell proliferation and damage to cell membranes. Proliferation was monitored through the reduction of a tetrazolium dye, and the integrity of the cell membrane was quantified through released lactate dehydrogenase (LDH). Mouse calvaria 3T3-E1 cells were used for the study. Cells were grown in alpha modified eagles medium (MEM) supplemented with 10 % fetal bovine serum and 1 % penicillin-streptomycin at 37°C under an atmosphere of 5 % $CO_2$ with changes in medium every other day until 90 % confluence, at which point, cells were harvested and seeded at 10,000 cells per well in a 48 well plate for proliferation assays and 10,000 cells per well in a 96 well plate for LDH assay. A period of 24 hours were allotted for cell attachment, after which cells were treated with the supernatant of a HA or CoHA, prepared via synthesis or ion exchange, solution. The HA and CoHA supernatant solutions were prepared by dispersing particles, that were previously dispersed in 70 % ethanol and rinsed three times with sterile de-ionized water, at concentrations of 20, 50 or 100 μg/ml in alpha-MEM. Each condition was tested in quadruplicate.

For the proliferation assay the medium was changed every day and the amount of used solution was replaced with an equal volume of alpha-MEM. At day 1, 3 and 7 the proliferation was assessed by replacing the medium with fresh alpha-MEM and adding a 5 mg/ml MTT working solution equal to $1/10^{th}$ the medium volume. The treated cells were incubated for 4 hours at 37°C. The medium was then removed and a solution of 0.04 N HCl in isopropanol was added to dissolve the formed crystals. Aliquots of 200 μl were measured using a microplate reader (Biotek) at 560 nm and the background absorbance was measured at 680 nm.

LDH activity was evaluated with a LDH assay kit from Thermo Scientific. In brief, after the cell attachment period cells were treated with 100 µl of supernatant medium from day 3 and 7 and for controls one set of cells were treated with the provided lysis solution for maximum LDH release and another set of cells were treated with medium only. After incubation for 24 hours 50 µl of working solution was added to the medium and the plate was incubated for 30 minutes at room temperature in the dark. The stop solution, 50 µl, was then added to the medium and 150 µl aliquots were taken for measurement. The absorbance of the aliquots was measured at 480 nm and the background was measured at 680 nm.

### *6.3 Results*

#### *6.3.1 Starting Powder Characterization*

The CoHA powder was characterized thoroughly Chapter 5 and the findings are briefly summarized here. EDX confirmed the presence of cobalt in the CoHA sample powder. The powder was analyzed for crystal structure and phase purity using X-ray diffraction and Fourier transform infrared spectroscopy. Additionally, magnetic properties were studied using superconducting quantum interference device analysis. The results showed that after cobalt substitution the powder retained characteristic apatite crystal structure and functional groups. Additionally, cobalt substituted samples displayed paramagnetic properties, as opposed to the diamagnetism of pure HA.

#### *6.3.2 Density and Biaxial Flexural Strength*

Both green and sintered densities were measured for HA and CoHA, with 10 pellets being measured at each sintering temperature examined for each powder type. Density values

were recorded as the average of these measurements (with standard deviations reported). Green and sintered densities, as well as thickness and diameter measurements, are listed in Table 6.1, and sintered densities as a function of sintering temperature for both HA and CoHA pellets are shown in Fig. 6.1.

**Table 6.1** Diameter, thickness, and density measurements of sample pellets before and after sintering

| Sample | Avg. Green Diameter (mm) | Avg. Green Thickness (mm) | Avg. Green Density ($g/cm^3$) | Avg. Sintered Diameter (mm) | Avg. Sintered Thickness (mm) | Avg. Sintered Density ($g/cm^3$) |
|---|---|---|---|---|---|---|
| **HA 900°C** | 12.81 | 1.63 | 1.65 | 10.66 | 1.43 | 2.50 |
| **HA 1000°C** | | | | 10.33 | 1.38 | 2.73 |
| **HA 1100°C** | | | | 10.23 | 1.34 | 2.86 |
| **HA 1200°C** | | | | 10.17 | 1.33 | 2.92 |
| **HA 1300°C** | | | | 10.21 | 1.37 | 2.80 |
| **CoHA 700°C** | 12.81 | 1.80 | 1.41 | 12.29 | 1.72 | 1.46 |
| **CoHA 800°C** | | | | 11.59 | 1.71 | 1.61 |
| **CoHA 900°C** | | | | 11.54 | 1.66 | 1.70 |
| **CoHA 1000°C** | | | | 10.70 | 1.54 | 2.15 |
| **CoHA 1100°C** | | | | 10.14 | 1.50 | 2.45 |
| **CoHA 1200°C** | | | | 10.09 | 1.48 | 2.46 |

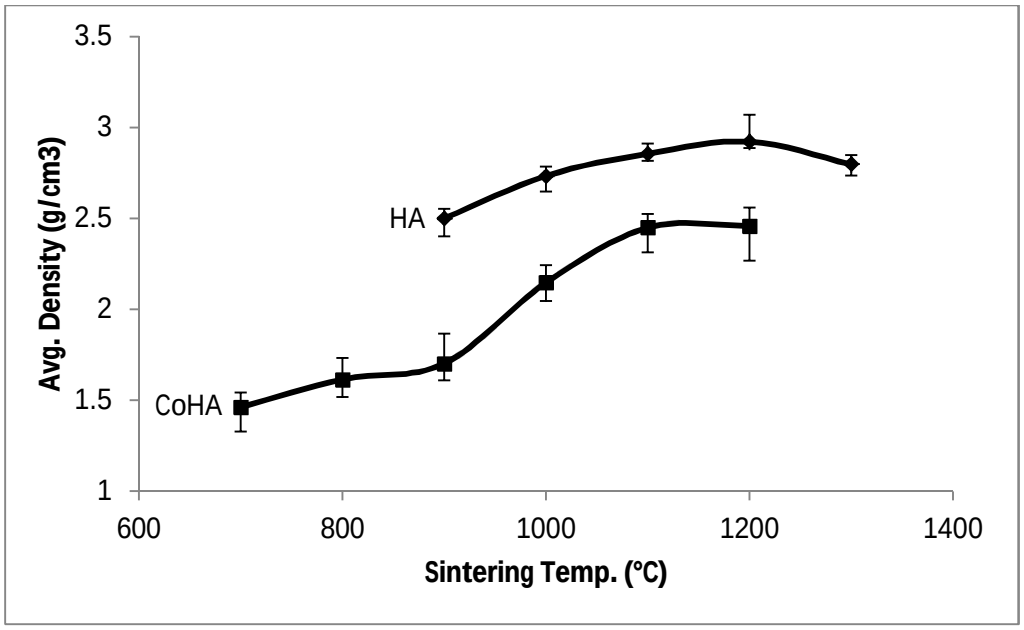


**Figure 6.1** Density as a function of sintering temperature for HA and CoHA pellets.

The average green density for pure HA pellets was 1.65 g/cm$^3$ and the average green density of CoHA pellets was 1.42 g/cm$^3$. The HA sintered densities increased with sintering temperature up to a maximum density of 2.92 g/cm$^3$ at 1200°C, and then dropped at 1300°C. The peak density achieved was 90% the theoretical density of HA. CoHA sintered densities increased with sintering temperature, to a maximum density of 2.46 g/cm$^3$ at 1200°C. There is a decrease in diameter with an increase in sintering temperature for every sample measured with the exception of the HA pellets sintered at 1300°C, and also a decrease in thickness compared to the green pellets for every sample measured with the exception of the HA pellets sintered at 1300°C.

After pellet densities were measured, the pellets were subjected to a modulus of rupture (MOR) test to study mechanical properties of the sintered pellets. The results of the MOR test are summarized in Table 6.2 and Fig. 6.2. The values are presented as averages plus/minus standard deviations.

**Table 6.2** Comparison of density and MOR values for HA and CoHA samples

| Sample | Avg. Density ($g/cm^3$) | Avg. MOR (MPa) |
|---|---|---|
| HA 900°C | 2.50 ±.05 | 36.50 ±11.1 |
| HA 1000°C | 2.73 ±.04 | 56.50 ±8.78 |
| HA 1100°C | 2.86 ±.03 | 54.34 ±6.80 |
| HA 1200°C | 2.92 ±.05 | 50.41 ±7.26 |
| HA 1300°C | 2.80 ±.03 | 29.13 ±5.19 |
| CoHA 700°C | 1.46 ±.06 | 10.02 ±1.59 |
| CoHA 800°C | 1.61 ±.07 | 11.80 ±3.36 |
| CoHA 900°C | 1.70 ±.08 | 15.89 ±4.58 |
| CoHA 1000°C | 2.15 ±.07 | 23.18 ±3.47 |
| CoHA 1100°C | 2.45 ±.06 | 28.86 ±9.19 |
| CoHA 1200°C | 2.46 ±.08 | 24.08 ±6.29 |

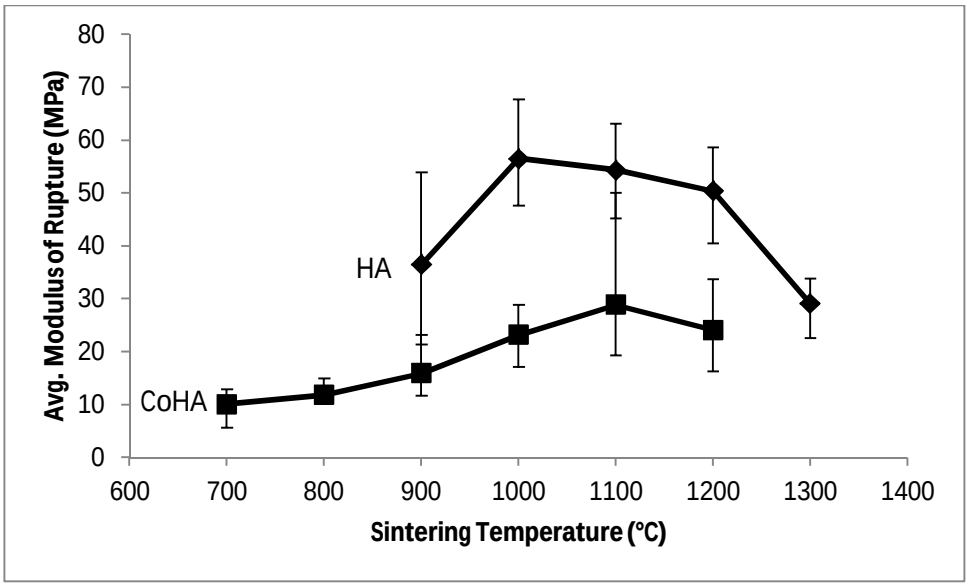


**Figure 6.2** MOR as a function of sintering temperature for HA and CoHA pellets.

The MOR of the sintered HA samples ranged from the lowest value of 29.13 MPa for pellets sintered at 1300°C to a peak value of 56.50 MPa for pellets sintered at 1000°C. Samples sintered at 900, 1100, and 1200°C had MOR values of 36.5, 54.34, and 50.41 MPa respectively (as shown in Figure 3). The MOR of the CoHA sintered samples were at a low of 10.02 MPa for the samples sintered at 700 °C and a high of 28.86 MPa for the samples sintered at 1100 °C. At sintering temperatures of 800, 900, 1000, and 1200°C, MOR values were 11.80, 15.89, 23.18, and 24.08 MPa, respectively.

An ANOVA F-test analysis was conducted on the mean MOR values resulting from 6 to 8 measurements at each temperature for both HA and CoHA. This analysis resulted in an F-value of 10.93 for the HA samples, greater than the $F_{crit}$-value of 2.76, thus there is a significant difference between the MOR values for the HA pellets sintered at different temperatures. ANOVA analysis for the CoHA samples resulted in an F-value of 12.59 ($F_{crit}$=2.46), indicating

significant difference between the MOR values for the CoHA pellets sintered at different temperatures.

*6.3.3 XRD Characterization*

Crystal structure and phase purity of the sintered HA and CoHA pellets were examined using XRD. The resulting XRD spectra are shown in Fig. 6.3 for HA and Fig. 6.4 for CoHA. HA sintered samples resulted in XRD spectra containing peaks that are identical to those present in the un-sintered HA control spectrum and match well with the HA JCPD reference card 9-432 for temperatures up to 1200°C. At 1200°C, an extraneous peak emerges at about 30° 2θ which would match with the TCP peak at 29.68° 2θ.

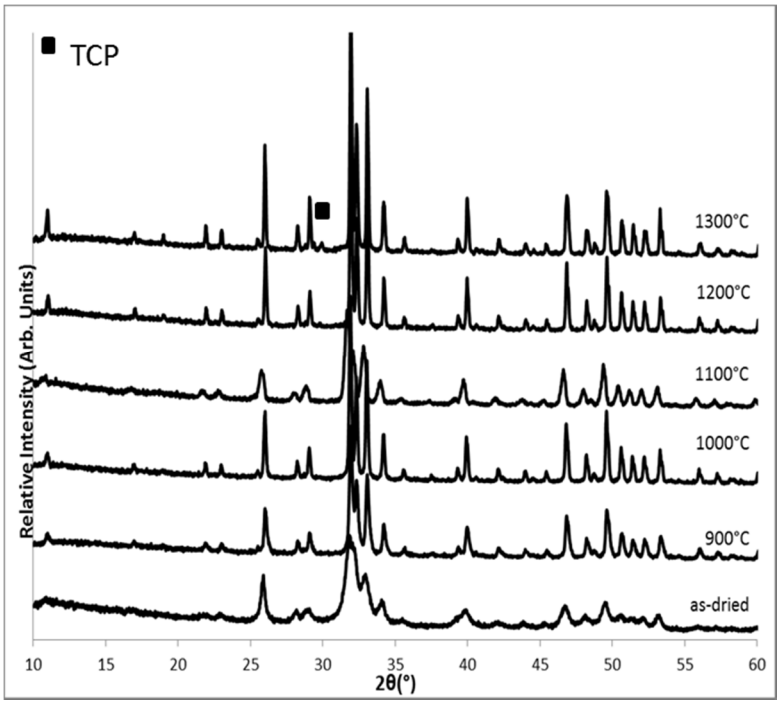

**Figure 6.3** XRD spectra for as-dried HA compared to HA sintered at 900, 1000, 1100, 1200 and 1300°C

CoHA sintered samples result in XRD spectra that do not match completely with the unsintered control sample. Extraneous peaks at about 13.7, 28.0, and 31.3° 2θ, which can be matched to TCP, emerge at sintering temperatures as low as 800°C. Additionally, starting at 700°C, there is an extraneous peak that emerges at about 36.5° 2 θ, which can likely be assigned to a cobalt oxide phase. In both HA and CoHA sintering led to sharper XRD peaks, indicating improved crystallinity as compared to the green samples.

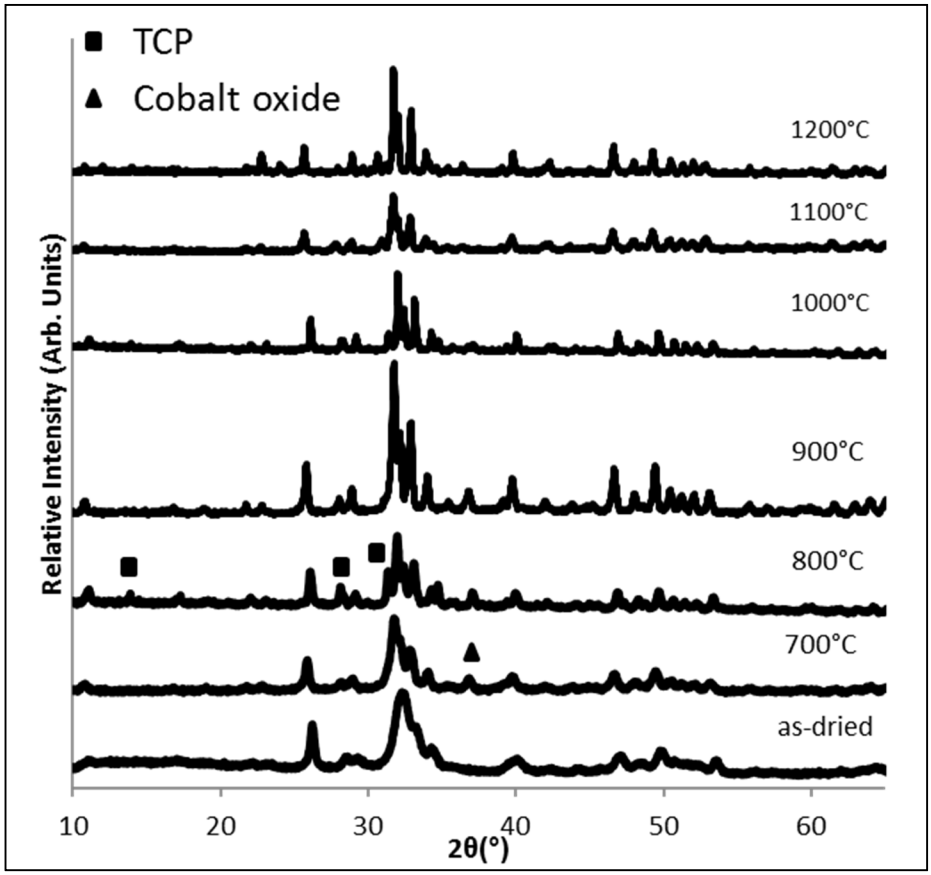


**Figure 6.4** XRD spectra for as-dried CoHA compared to CoHA sintered at 700, 800, 900, 1000, 1100 and 1200°C.

*6.3.4 FESEM Characterization*

Unpolished fracture surfaces of the sintered pellets were imaged using FESEM allowing the observation of the microporosity of these samples and the extent to which the samples have been sintered to be examined. Fig. 6.5 contains the micrographs of the HA pellet cross-sections sintered at different temperatures. It is apparent that sintering does not start until 1000°C, at which temperature sintering has just started, as evidenced by the consolidation of packed powder particles to bulk material, and there is a system of interconnected pores at the nanometer scale. At 1100°C the amount of sintering is increased and some areas are fully densified, but some retain the interconnected porosity as seen at 1000°C. The samples sintered at 1200°C are shown to be highly dense with discreet nanometer sized pores. At 1300°C, as in the 1200°C, the HA particles seem fully sintered, but discreet pores around micron in size start to appear.

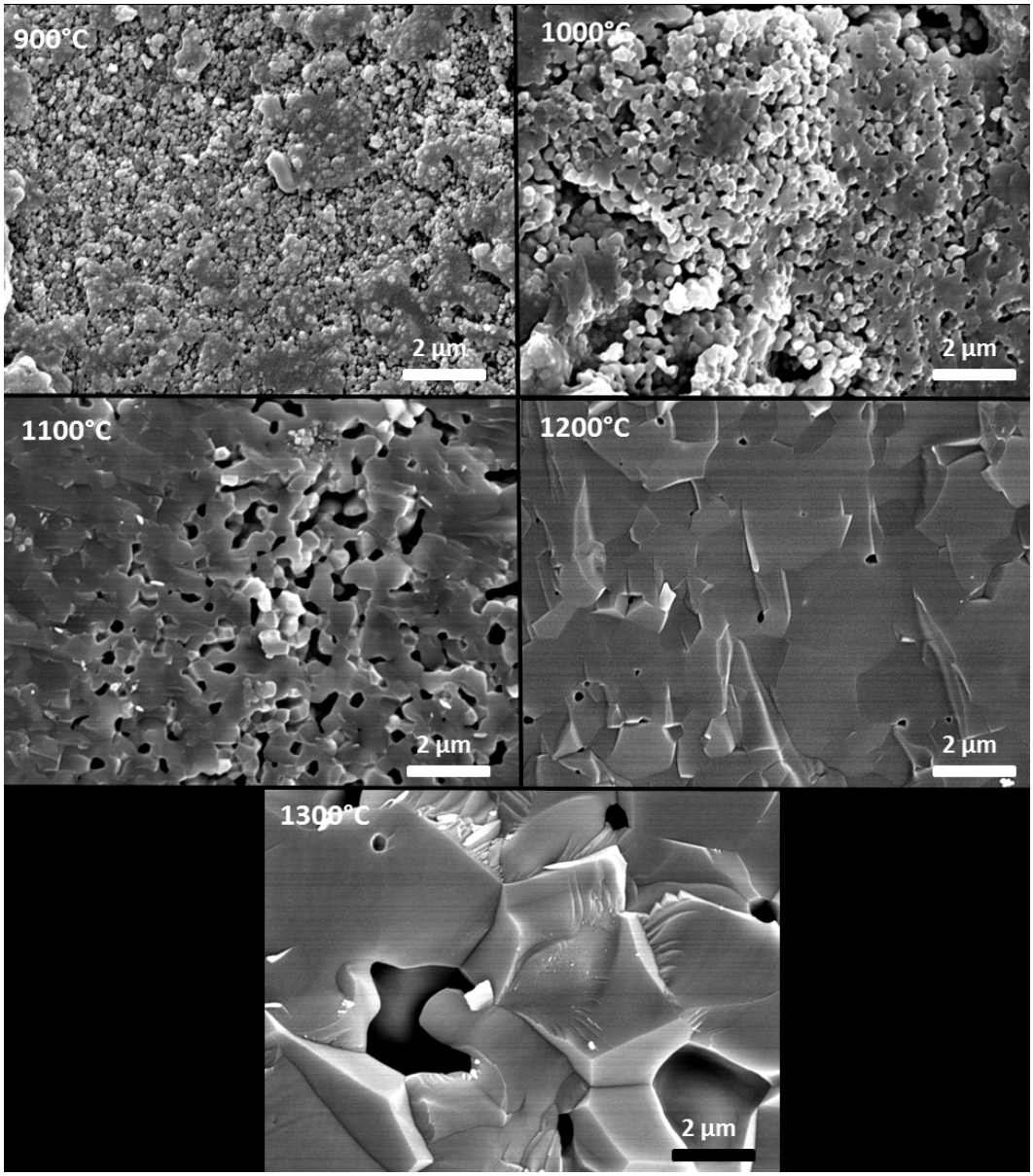


**Figure 6.5** Cross sections of HA pellets sintered at 900, 1000, 1100, 1200 and 1300°C. (Repeat of Fig. 4.7)

Fig. 6.6 contains the micrographs of the CoHA pellet cross-sections sintered at different temperatures. At 700°C, sintering has not begun in CoHA pellets, and the samples retain the interconnected microporosity seen in the HA samples sintered at 900°C. At 800 and 900°C sintering has begun, as demonstrated by the clear merging starting to occur between particles, but

the interconnected microporosity is preserved, and the pellets still retain a morphology that is mostly reflective of a packed powder. At 1000°C, sintering is well underway and the CoHA particles are no longer clearly differentiated. The pellets at 1000°C contain dense regions but are still highly porous with seemingly interconnected pores. The CoHA pellets sintered at 1100 and 1200°C are essentially a fully dense material interspersed with micron sized pores. The level of porosity is greater than that seen in the HA sintered at 1200 and 1300°C. Additionally, pore number decreases from 1100 to 1200°C, but pore size increases.

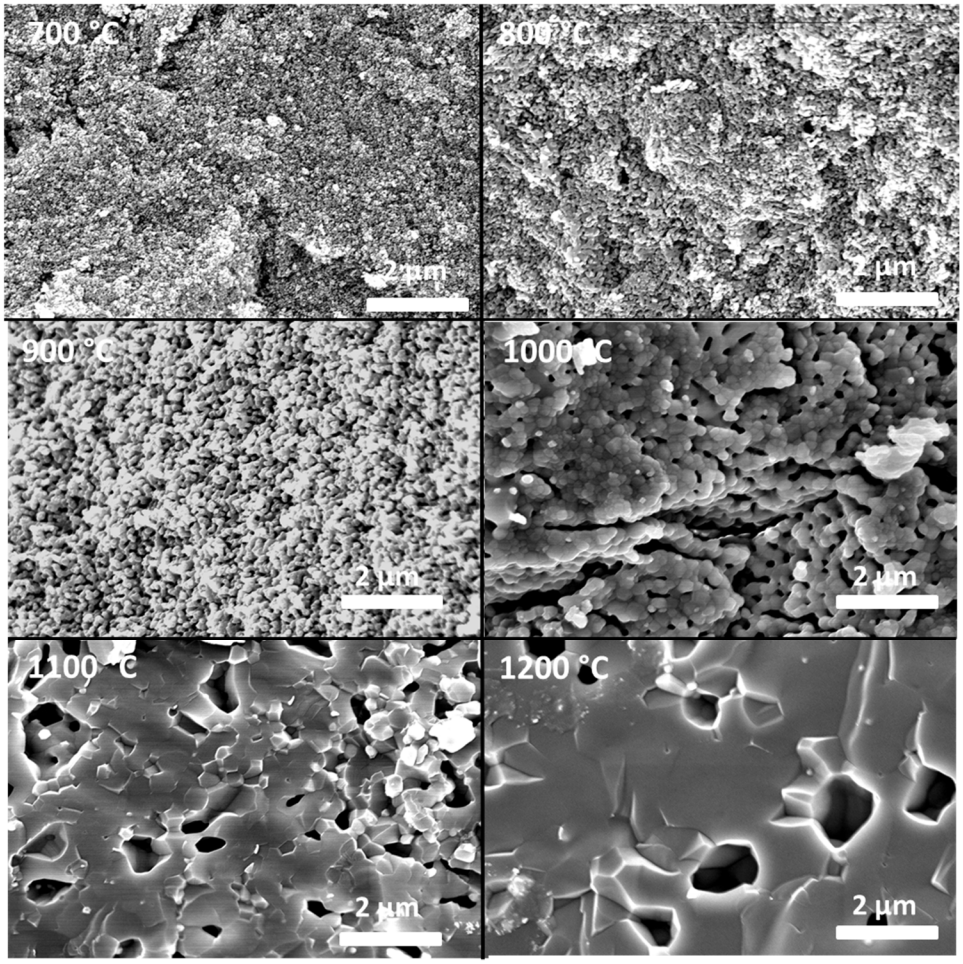


**Figure 6.6** Cross sections of CoHA pellets sintered at 700, 800, 900, 1000, 1100 and 1200°C.

*6.3.5 Cell Culture Study*

The effect of CoHA on cellular proliferation was inhibitive, while HA supported cell proliferation, as seen in Fig. 6.7. The HA treated cells proliferated at the same rate over the course of one week. In contrast the CoHA treated cells did not proliferate from day 1 to 3 with the optical density (O.D.) remaining the same while the cell number decreased from day 3 to 7 with a decrease in O.D.. The LDH assay results are presented in Fig. 6.8. Compared to the spontaneous release of LDH from cells treated with medium alone there is no statistical difference between the spontaneous release and the release from HA or CoHA treatments for 3 and 7 days.

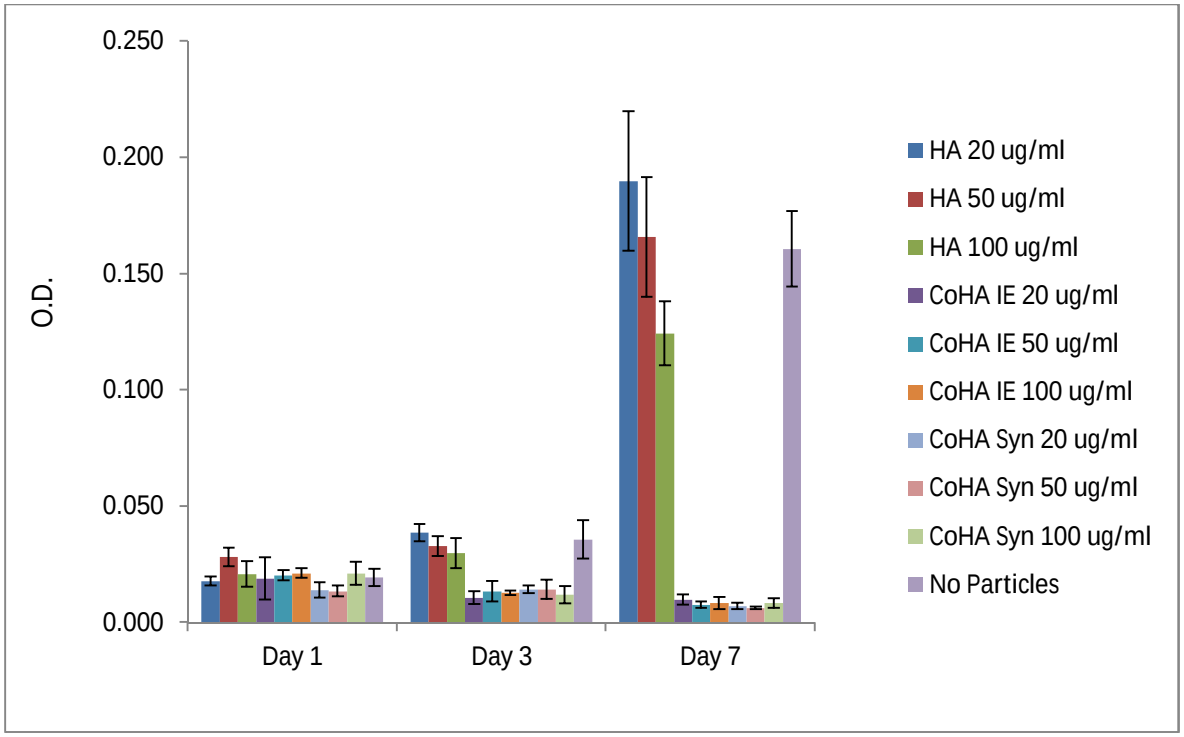


**Figure 6.7** Cellular proliferation of cells treated with HA and CoHA supernatants in a 48 well plate.

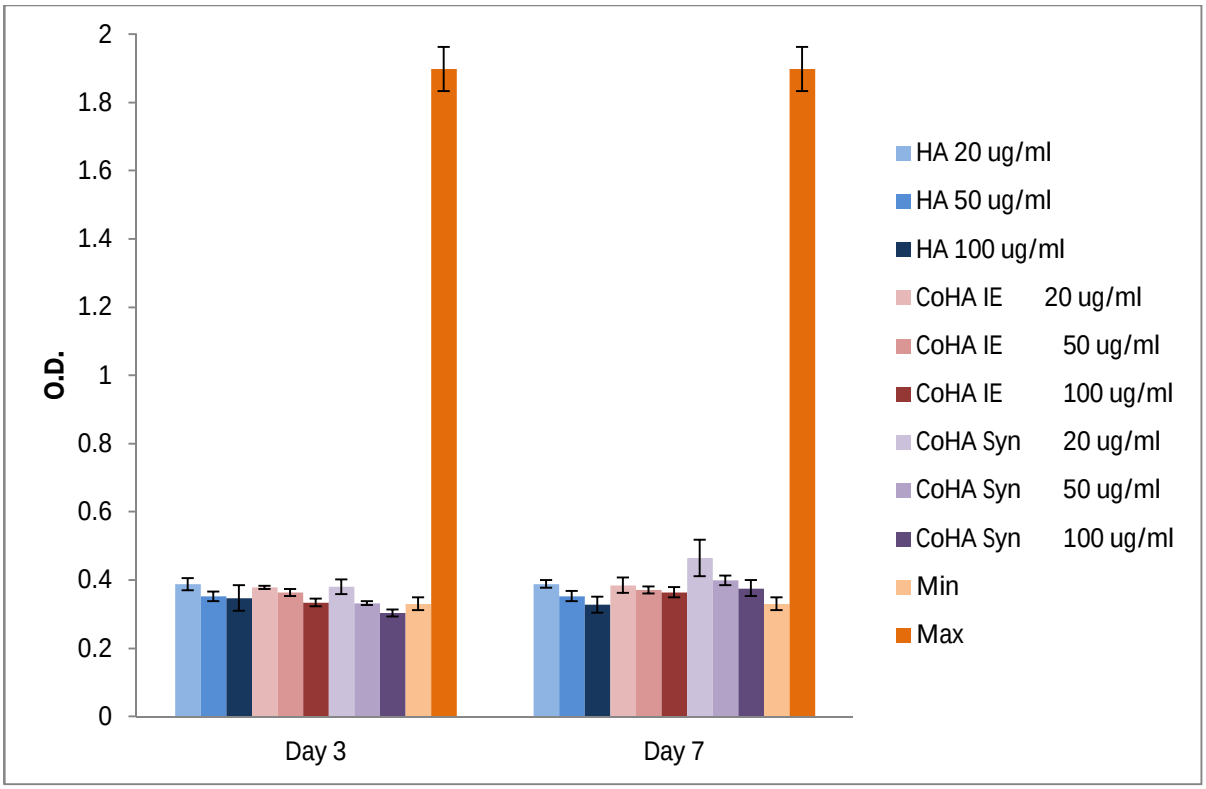


**Figure 6.8** LDH release of cells incubated with supernatant from HA and CoHA for 24 hours. Supernatants were collected from 3 and 7 days after the powders were immersed in medium.

*6.4 Discussion*

HA can generally be sintered up to 1200°C or above before it is decomposed to TCP and CaO [99, 11]. In this study, HA was sintered from 900°C up to 1300°C and cobalt substituted HA was sintered from 700°C up to 1200°C. The HA pellets underwent shrinkage (from an average diameter of 12.81 mm for the green pellets down to an average diameter of 10.17 mm for pellets sintered at 1200°C) but otherwise retained their white appearance with flat top and bottom surfaces. The CoHA pellets, on the other hand, underwent not only shrinkage but also an obvious color change upon sintering.

Fig. 6.9 is a photograph of green and sintered CoHA pellets showing the change in color that accompanied the sintering procedure at each temperature point. Un-sintered CoHA pellets demonstrate a bright purple color, but upon sintering this changes drastically. Pellets sintered at 700°C exhibit such a dark color that they look essentially black. Sintering at 800°C results in dark charcoal grey. Pellets sintered at temperatures from 900 to 1200°C all display grey coloring, which gets darker with increasing temperature. In addition to getting darker, the grey becomes increasingly muddy and brownish. Although the CoHA pellets undergo distinct color changes, they also retain the typical flat surfaced appearance of the HA pellets, and diameter shrinks with increasing sintering temperature.

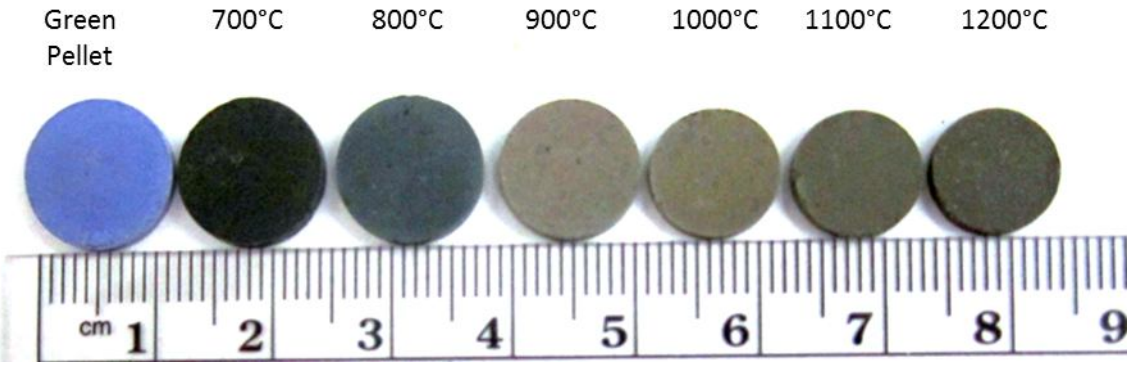


**Figure 6.9** Photograph of CoHA pellets sintered at various temperatures

CoHA sintered pellets have obvious visual differences compared to the pure HA pellets, but densification behavior and mechanical properties show similar trends, although the actual densities and MOR achieved are different. HA pellet density increased until 1200°C, and at 1300°C began to drop. CoHA pellet density also increased to 1200°C, with the largest increase coming between 900 and 1000°C, but the actual densities achieved were lower than those

achieved with pure HA at the same temperatures. For example, for pellets sintered at 900, 1000, and 1100°C, the density of HA samples are 2.50, 2.73, and 2.86 g/cm$^3$, respectively, but CoHA pellets sintered at the same temperatures have average densities of 1.70, 2.15, and 2.45 g/cm$^3$, respectively. This is unsurprising considering that the green density of CoHA was also lower than that of pure HA. The overall trend of increasing density is to be expected, since densification typically increases with sintering temperature prior to the onset of significant decomposition [106]. At their peak density, the HA pellets attain a density of 2.92 g/cm$^3$ sintered at 1200°C, which is 93% of the theoretical density of HA (3.156 g/cm$^3$). The density of CoHA on the other hand, never approaches the theoretical density of HA within the temperature range tested. CoHA density in this study peaked at 2.46 g/cm$^3$, which is only 78% the theoretical density of HA.

Considering the lower achieved densities, the MOR of the CoHA pellets are also lower than that of the HA pellets. The HA pellets achieve a maximum MOR value of 56.50 MPa, a value that compares favorably to the mechanical properties of bulk HA achieved by other groups in the literature [105, 106], and is also within the mechanical properties range of natural bone, which possesses flexural modulus values ranging from 35 to 283 MPa [107]. CoHA achieved a maximum MOR value of 28.86, slightly below the low end of the range of flexural modulus values for natural bone.

The MOR is displayed as a function of sintering temperature in Fig. 6.3 and as a function of density in Table 6.2. For pure HA, the MOR roughly plateaus between 1000 and 1100°C, with a slightly decrease at 1200°C. A significant decrease in MOR at 1300°C corresponds to a decrease in pellet density. This decrease may be due to the onset of decomposition of HA at high temperatures. The MOR of the CoHA pellets increase steadily to 1100°C and begins to

decrease significantly at 1200°C, despite the fact that density has not yet begun to decrease at that temperature point.

The porosity of the sintered HA pellets dramatically increased at 1300°C, as shown by the FESEM images and corroborated by the decrease in density shown in Fig. 6.2 and Table 6.1. The increase in both number and size of micropores at 1300°C compared to 1200°C may be due to increased decomposition. Sintering initially causes the close of pores, but concurrent dehydroxylation results in the formation of an internal vapor pressure that eventually overcomes the mechanical strength of the solid, resulting in the formation of blowholes. At higher temperatures a large amount of irreversible dehydroxylation occurs coupled with decomposition, of which water vapor is a product, leading to a collapse of the hydrated HA structure, and a large increase in blowhole area [108].

The CoHA pellets were shown to have increased porosity at 1200°C, as compared to 1100°C. This increase in porosity was accompanied by a decrease in MOR, despite a slight increase in overall density. At no sintering temperature are the density and porosity of the HA sintered at 1200°C approximated by the CoHA pellets. This is likely a result of an earlier onset of decomposition and formation of blowholes in CoHA than in HA. A similar result was also observed for iron-substituted HA, which decomposed at temperatures are low as 700°C (Chapter 4). In addition to the density and mechanical property measurements, it is clear from visual inspection that the CoHA pellets have a different sintering behavior than the pure HA. It is likely caused by the presence of cobalt ions in the HA lattice resulting in a less stable crystal structure, thereby resulting in decomposition and formation of second phases at lower temperatures than those initiating decomposition in HA. XRD analysis was conducted and confirmed this hypothesis.

A single-phase HA was achieved at sintering temperatures up to 1200°C, which was indicated by no extraneous peaks being present in the relative XRD spectra in Figure 4, which mimics typical sintering behavior in pure HA [99, 100]. The emergence of an extraneous peak at 30° 2θ, which can be assigned to TCP, indicates the onset of decomposition. This explains the decrease in density and mechanical properties observed in the HA pellets sintered at 1200 and 1300°C. CoHA pellets were found to be less thermally stable than the HA, and emergence of a secondary cobalt containing phase indicating cobalt oxidation started as low as 700°C, with emergence of TCP peaks indicating hydroxyapatite decomposition occurring as low as 800°C.

In CoHA sintered at 800°C and above extraneous peaks emerged at about 13.5, 28, and 31° 2θ. Each of these three peaks can be assigned to TCP, which has major peaks at 13.64, 27.79, and 31.05° 2θ. At 700° C and above there is also an obvious extraneous peak at about 36.5° 2θ. Neither HA nor TCP have XRD peaks at this location, so the possibility must be investigated that this peak belongs to an emerging cobalt containing phase, likely a cobalt oxide or hydroxide. Possibilities, determined by which cobalt oxide and hydroxide phases have significant peaks around 36.5° 2θ, include CoO, $Co_3O_4$, and $Co(OH)_3$. Unfortunately, other significant peaks for these materials overlap with HA and TCP peaks, so direct identification based on extraneous peaks is difficult. Sintered CoHA pellets likely contain varying mixtures of calcium phosphate (HA and TCP) and cobalt oxide and hydroxide phases. From 600-700°C, CoO is readily oxidized in air to $Co_3O_4$. This behavior, combined with the fact that $Co_3O_4$ is characterized by a typical black color accounting for the color change seen in the CoHA pellet sintered at 700°C, allows us to conclude that $Co_3O_4$ is present in the CoHA pellets sintered at 700°C. Examination of the calcium phosphate peaks in the XRD spectra for this sample indicates that at 700°C the $Co_3O_4$ is present mostly in combination with HA. Beginning at

800°C we see a change in pellet color away from black and towards an increasingly muddy greyish brownish color. Our XRD results suggest that TCP also starts to emerge at this temperature. Samples sintered at 800°C and above are therefore combinations of HA, TCP, and various cobalt oxide or hydroxide phases. Above 900°C CoO is thermally stable (as opposed to $Co_3O_4$), but can be readily oxidized to $Co(OH)_3$. CoO has a characteristic olive color, whereas $Co(OH)_3$ is grayish brownish in color. From 800°C to 1200°C there is probably a phase change from $Co_3O_4$ to $Co(OH)_3$. This conclusion is based on an inspection of the color change seen in the pellets combined with knowledge about cobalt oxide and hydroxide relative thermal stabilities, oxidation behaviors, and characteristic XRD spectra. In summary, we can conclude that CoHA samples sintered in air undergo various phase transformations from pure CoHA to apatite plus cobalt oxide, then further transform to a combination of calcium phosphate phases (mostly HA and TCP) plus a combination of cobalt oxide and hydroxide phases, with cobalt hydroxide dominating at higher temperatures.

The incorporation of cobalt ions into the HA lattice in the form of CoHA results in a material that is less thermally stable than pure HA, as proven by the difference in decomposition behavior as a result of sintering. Additionally, the relatively lower density and MOR of CoHA compared to HA make CoHA less suitable for bulk applications, particularly those which are load bearing, since a MOR within the range of natural bone was not achieved by the CoHA material. Even bulk HA is typically used only in low-load-bearing situations, and the mechanical strength of CoHA is even more poor. The CoHA material may, however, be useful in biomedical applications which call for nanoparticles in powder form, or as a coating or filler phase in a composite, specifically applications which utilize paramagnetic properties. The lower stability of the CoHA material compared to the HA control suggests that degradation in vivo

may be quicker. A faster degradation rate may be a desirable trait for certain applications which call for short-term use of nanoparticles.

Prior to utilization in biomedical applications, the biocompatibility of CoHA needs to be evaluated. While the results from the proliferation experiment may initially suggest that CoHA is not biocompatible, the findings from the LDH assay, Fig. 6.8, suggest differently. The discrepancy between these results suggests that either a catalytic reaction occurs between CoHA and the cell culture medium or the release of cobalt ions inhibits cell proliferation. Although a degradation study indicated the total cobalt release over the course of a month (Chapter 5) is extremely low, there was a burst release of cobalt ions at day 1. It may be beneficial to include an extended 24 hour washing step in DIW in the CoHA synthesis protocols, to remove loosely bound cobalt ions responsible for the burst seen in the degradation study. The cell culture studies presented in this chapter are also limited in that a single cell line was used. Various cell lines may react differently to differing culture conditions. For example, Wu et al. established that low amounts of cobalt incorporation into a scaffold resulted in no cytotoxicity in human bone marrow stromal cells (BMSCs). Additionally, cobalt ion release from the scaffold induced VEGF protein secretion, HIF-1α expression, and bone-related gene expression in BMSCs, indicating that while cobalt ions result in a response that mimics hypoxic conditions, they did not induce toxicity or cell death [126]. Additionally, *in vitro* cell culture conditions are simple and static, as compared to *in vivo* conditions. *In vivo* response to cobalt release from CoHA may differ from that seen *in vitro*. The cell culture results obtained in this chapter are not sufficient to draw any strong conclusions, and the CoHA material needs to be further investigated for its biocompatibility.

*6.5 Conclusion*

The sintering behavior of CoHA, a paramagnetic biodegradable nanoparticle material, was thoroughly examined in this study. Density measurements, mechanical testing, FESEM, and XRD analysis were used to elucidate the sintering behavior of CoHA as compared to pure HA. It was found that CoHA has a lower stability than pure HA, and begins to decompose into a multi-phase material containing HA and cobalt oxide at temperatures as low as 700°C, and HA, TCP, and cobalt oxide and hydroxide at temperatures of 800°C and above. It is expected, based on these results, that CoHA will degrade more quickly *in vivo* than pure HA. Thus, together with other characterizations of CoHA (magnetic properties and degradation behavior), it is suggested that CoHA is a biomaterial suitable for applications which require fast biodegradable magnetic materials, although cell culture results in this study were inconclusive.

# Chapter 7

## Conclusions and Future Work

### *7.1 Conclusions*

In this work iron- and cobalt-substituted hydroxyapatite powders have been synthesized and fully characterized. Both FeHA and CoHA sample powders were found to be phase-pure, with no secondary phase formation. This is significant because phase purity influences the bioactivity, solubility, and *in vivo* behavior of bioceramics. Furthermore, all samples tested were found to have paramagnetic properties. The magnetic susceptibility of the substituted powders was not a function of iron or cobalt content. Unlike in bulk materials where magnetic susceptibility is an inherent material constant, in nanomaterials magnetic susceptibility is a function of a number of factors including particle size and shape [78]. The paramagnetic properties displayed by the substituted apatites will allow them to be utilized for a wide range of biomedical applications that pure HA nanoparticles are not suitable for.

FeHA can be achieved using a simple ion exchange procedure. CoHA can be attained using this same ion exchange procedure, or via wet synthesis. These methods are simple, fast, and low-cost procedures for tailoring the material properties of HA.

A sintering study conducted on FeHA and CoHA sample pellets showed that substituted hydroxyapatite is less thermally stable than pure HA. At temperatures much lower than those that induce decomposition in HA the FeHA and CoHA pellets began to decompose to TCP and metal oxide phases. Although CoHA begins to decompose at similar low temperatures as FeHA, they demonstrated better mechanical properties than FeHA, achieving density and mechanical

strengths closer to HA. A lower thermal stability suggests that the substituted HA particles degrade at a faster rate *in vivo* than pure HA, a trait which may be desirable to prevent accumulation of magnetic nanoparticles for transient and/or repetitive applications. *In vitro* degradation studies lasting up to a month confirmed that despite the less stable nature of the substituted apatites, the release of metal ions ($Fe^{3+}$ and $Co^{2+}$) were at low enough levels to be tolerated by the human body, thus alleviating some concerns about material biocompatibility.

Cell viability was also tested for FeHA and CoHA. The FeHA material resulted in cell viability comparable to that of pure HA, a widely used and highly biocompatible material. CoHA degradation study results were promising, as only low levels of cobalt were released for the duration of the study, but cell culture results were inconclusive. Thorough characterization of these substituted apatite materials indicate that FeHA and CoHA are especially attractive materials for use in transient biomedical applications requiring magnetic properties, such as drug delivery, MRI contrast, and hyperthermia based cancer treatments. They may also have potential in a wider range of applications including, but not limited to, cell stimulation in bone repair, cell labelling and separation, and combined therapies.

## *7.2 Future Work*

### *7.2.1 Application-Driven Testing of FeHA and CoHA*

FeHA and CoHA have been thoroughly characterized, and thus should next be subjected to application-driven testing. This will allow further evaluation of which applications these materials are suitable for, and will begin moving these materials towards clinical use. Application-driven experiments will also indicate whether the magnetic properties of these materials need to be adjusted, which can be done by altering the size or shape of the

nanoparticles, or potentially the amount of metal ion doped into the material if necessary [78]. Materials examined in this work demonstrating paramagnetic behavior may demonstrate superparamagnetic behavior if the particle size scale is decreased sufficiently.

In order to evaluate whether the FeHA or CoHA materials can be applied as MRI contrast agents the $T_1$ and $T_2$ relaxation times can be measured using nuclear magnetic resonance (NMR) spectroscopy. After initial measurements are conducted on nanoparticles in solution, the nanoparticles can be introduced to tissue samples, and the resulting relaxation times can be compared to those of the tissue without the FeHA or CoHA nanoparticles. Other paramagnetic materials have been shown to be effective as MRI contrast agents, and as such the outlook for magnetic substituted HA materials as MRI contrast agents is positive [127, 128].

The ability of FeHA and CoHA nanoparticles to generate heat needs to be examined to determine the suitability of the materials for use in hyperthermia related cancer treatments. The materials would need to be exposed to an alternating magnetic field in a thermally insulated sample holder equipped with a thermocouple to measure temperature change.

The utility of FeHA and CoHA as magnetic drug delivery agents will need to be tested. The ceramic nanoparticles should be conjugated to model protein molecules and the distribution of the drug-carrier complex should be measured in animal models both with and without external magnetic fields. In order for the magnetic field to successfully concentrate the drug-carrier complex, the magnetic force acting on the particles must overcome the hydrodynamic force acting on the particle as a result of blood flow. The magnetic force, $F_m$, can be described as:

$$F_m = V_m \Delta\chi \nabla \left(\frac{1}{2} B \cdot H\right),$$

where $V_m$ is the volume of the particle, $\Delta\chi$ is the difference in magnetic susceptibility between the particle and the surrounding fluid (blood), B is the magnetic field flux, and H is the

magnetic field strength. The magnetic field used for this application would be static, and therefore the field strength is limited only by the strength of magnet that can be obtained. There is no evidence or example of a strong static magnetic field causing negative pathological effects [129]. This allows the use of a magnet strong enough to cause a response in paramagnetic particles to be used for further testing for drug delivery applications of FeHA and CoHA.

### *7.2.2 Manganese Substituted Hydroxyapatite*

Another substituted apatite system of interest may be manganese. Manganese metals and its ions also have intrinsic paramagnetic properties [130]. Manganese has the additional attractive feature of improving cellular adhesion [131-134]. As such, MnHA would be an excellent candidate for use in bone repair scaffolds where it could potentially magnetically stimulate osteoblast cells while also improving cellular adhesion to the implanted scaffold.

### *7.2.3 Rare Earth Substituted Hydroxyapatite*

The rare earth elements are also interesting candidates for generating hydroxyapatites with magnetic properties. Among the rare earth elements samarium, europium, gadolinium, and terbium may be the most attractive options. Europium, gadolinium, and terbium have the strongest magnetic properties (paramagnetic for europium, and ferromagnetic for gadolinium and terbium), while also maintaining acceptable biocompatibility [135-137]. Samarium is also paramagnetic, although with a magnetic susceptibility an order of magnitude lower than europium, and has been shown to be a favorable substrate for osteoblasts in the oxide form [135, 136].

**References**

[1] Martini FH. Fundamentals of Anatomy and Physiology. San Francisco: Pearson-Benjamin Cummings; 2006.

[2] Weiner S, Wagner HD. The Material Bone: Structure-Mechanical Function Relations. Annu Rev Mater Res. 1998; 28: 271-298.

[3] Suchanek W, Yoshimura M. Processing and properties of hydroxyapatite-based biomaterials for use as hard tissue replacement implants. J Mater Res. 1998; 13: 94-117.

[4] Ferraz MP, Monterio FJ, Manuel CM. Hydroxyapatite nanoparticles: A review of preparation methodologies. J Appl Biomater Biom. 2004; 2: 74-80.

[5] Park JB, Bronzino JD. Biomaterials Principles and Applications. Boca Raton: CRC Press, 2003.

[6] Snyders R, Music D, Sigumonrong D, Schelnberger B, Jensen J, Schneider JM. Experimental and ab initio studies of the mechanical properties of hydroxyapatite. Appl Phys Lett. 2007; 90: 193902.

[7] Mostafa NY, Brown PW. Computer simulation of stoichiometric hydroxyapatite: Structure and substitutions. J Phys Chem Solids. 2007; 68: 431-437.

[8] Posner AS, Perloff A, Diorio AF. Refinement of the hydroxyapatite structure. Acta Cryst. 1958; 11: 308.

[9] Sadat-Shojai M, Khorasani MT, Dinpanah-Khoshdargi E, Jamshidi A. Synthesis methods for nanosized hydroxyapatite with diverse structures. Acta Biomater. 2013; 9: 7591-7621.

[10] Gergely G, Wéber F, Lukács I, Illés L, Tóth AL, Horváth ZE, Mihály J, Balázsi C. Nano-hydroxyapatite preparation from biogenic raw materials. Cent Eur J Chem. 2010; 8: 375-381.

[11] Marchegiani F, Cibej E, Vergni P, Tosi G, Fermani S, Falini G. Hydroxyapatite synthesis from biogenic calcite single crystals into phosphate solutions at ambient conditions. J Cryst Growth. 2009; 311: 4219-4225.

[12] Rivera EM, Araiza M, Brostow W, Castaño VM, Díaz-Estrada JR, Hernández R, Rogelio Rodríguez J. Synthesis of hydroxyapatite from eggshells. Mater Lett. 1999; 41: 128-134.

[13] Siva Rama Krishna D, Siddharthan A, Seshadri SK, Sampath Kumar TS. A novel route for synthesis of nanocrystalline hydroxyapatite from eggshell waste. J Mater Sci: Mater Med. 2007; 18: 1735-1743.

[14] Pramanik S, Agarwai AK, Rai KN, Garg A. Development of high strength hydroxyapatite by solid-state-sintering process. Ceram Int. 2007; 33: 419-426.

[15] Yeong KCB, Wang J, Ng SC. Mechanochemical synthesis of nanocrystalline hydroxyapatite from CaO and $CaHPO_4$. Biomaterials. 2001; 22: 2705-2712.

[16] Tas AC. Combustion synthesis of calcium phosphate bioceramic powders. J Eur Ceram Soc. 2000; 20: 2389-2394.

[17] Pratihar SK, Garg M, Mehra S, Bhattacharyya S. Phase evolution and sintering kinetics of hydroxyapatite synthesized by solution combustion technique. J Mater Sci: Mater Med. 2006; 17: 501-507.

[18] Fulmer MT, Brown PW. Hydrolysis of dicalcium phosphate dihydrate to hydroxyapatite. J Mater Sci: Mater Med. 1998; 9: 197-202.

[19] Durucan C, Brown PW. Alpha-Tricalcium phosphate hydrolysis to hydroxyapatite at and near physiological temperature. J Mater Sci: Mater Med. 2000; 11: 365-371.

[20] Monma H, Ueno S, Kanazawa T. Properties of hydroxyapatite prepared by the hydrolysis of tricalcium phosphate. J Chem Technol Biot. 1981; 31: 15-24.

[21] Ishikawa K, Eanes ED. The hydrolysis of anhydrous dicalcium phosphate intro hydroxyapatite. J Dent Res. 1993; 72: 474-480.

[22] Monma H, Kamiya T. Preparation of hydroxyapatite by the hydrolysis of brushite. J Mater Sci. 1987; 22: 4247-4250.

[23] Sopyan I, Toibah AR, Natasha AN. Nanosized bioceramic hydroxyapatite powders via sol-gel method. IJMME. 2008; 3: 133-138.

[24] Chai CS, Gross KA, Ben-Nissan B. Critical ageing of hydroxyapatite sol-gel solutions. Biomaterials. 1998; 19: 2291-2296.

[25] Liu DM, Troczynski T, Tseng WJ. Water-based sol-gel synthesis of hydroxyapatite: process development. Biomaterials. 2001; 22: 1721-1730.

[26] Liu DM, Yang Q, Troczynski T, Tseng WJ. Structural evolution of sol-gel derived hydroxyapatite. Biomaterials. 2002; 23: 1679-1687.

[27] Weng H, Huang L, Han G. The alkoxide sol-gel process in the calcium phosphate system and its applications. Appl Organomet Chem. 1999; 13: 555-564.

[28] Masuda Y, Matubara K, Sakka S. Synthesis of hydroxyapatite from metal alkoxides through sol-gel technique. J Ceram Soc Jpn. 1990; 98: 1255-1266.

[29] Hattori L, Lwadate Y. Hydrothermal Preparation of Calcium Hydroxyapatite Powders. J Am Ceram Soc. 1990; 73: 1803-1805.

[30] Montazeri L, Javadpour J, Shokrgozar MA, Bonakdar S, Javadian S. Hydrothermal synthesis and characterization of hydroxyapatite and fluorhydroxyapatite nano-size powders. Biomed Mater. 2010; 5: 045004.

[31] Jinlong N. Hydrothermal Synthesis of Nano-crystalline Hydroxyapatite. Key Eng Mat. 2007; 330-332: 247-250.

[32] Han JK, Song HY, Saito F, Lee BT. Synthesis of high purity nano-sized hydroxyapatite powder by microwave-hydrothermal method. Mater Chem Phys. 2006; 99: 235-239.

[33] Pang YX, Bao X. Influence of temperature, ripening time, and calcination of the morphology and crystallinity of hydroxyapatite nanoparticles. J Eur Ceram Soc. 2003; 23: 1697-1704.

[34] Lazic S, Zec S, Milijevic N, Milonjic S. The effect of temperature on the properties of hydroxyapatite precipitated from calcium hydroxide and phosphoric acid. Thermochim Acta. 2001; 374: 13-22.

[35] Peng F, Veilleux E, Schmidt M, Wei M. Synthesis of hydroxyapatite nanoparticles with tailorable morphology and carbonate substitutions using precipitation method. J Nanosci Nanotechno. 2012; 11: 1-9.

[36] Kothapelli C, Wei M, Vasiliev A, Shaw MT. Influence of temperature and concentration on the sintering behavior and mechanical properties of hydroxyapatite. Acta Mater. 2004; 52: 5655-5663.

[37] Zhang H, Darvell BW. Morphology and structural characteristics on hydroxyapatite whiskers: Effect of the initial Ca concentration, Ca/P ratio, and pH. Acta Biomater. 2011; 7: 2960-2968.

[38] Osaka A, Miura Y, Takeuchi K, Asada M, Takahashi K. Calcium apatite prepared from calcium hydroxide and orthophosphoric acid. J Mater Sci: Mater Med. 1991; 2: 51-55.

[39] Correia RN, Magalhães MCF, Marques PAAP, Senos AMR. Wet synthesis and characterization of modified hydroxyapatite powders. J Mater Sci: Mater Med. 1996; 7: 501-505.

[40] Saeri MR, Afshar A, Ghorbani M, Ehsani N, Sorrell CC. The wet precipitation process of hydroxyapatite. Mater Lett. 2003; 57: 4064-4069.

[41] Donadel K, Laranjeira MCM, Goncalves VL, Favere VT, de Lima JC, Prates LHM. Hydroxyapatites produced by wet chemical methods. J Am Ceram Soc. 2005; 88: 2230-2235.

[42] López-Macipe A, Rodríguez-Clemente R, Hidalgo-López A, Arita I, García-Garduño MV, Rivera E, Castaño VM. Wet Chemical Synthesis of Hydroxyapatite Particles from Nonstoichiometric Solutions. J Mater Synth Proces. 1998; 6: 21-26.

[43] Santos MH, de Oliveira M, de Freitas Souza LP, Mansur HS, Vasconcelos WL. Synthesis control and characterization of hydroxyapatite prepared by wet precipitation process. Mat Res. 2004; 7: 625-630.

[44] Biji A, Boanini E, Capuccini C, Gazzano M. Strontium-substituted hydroxyapatite nanocrystals. Inorg Chim Acta. 2007; 360: 1009-1016.

[45] Pan Y, Fleet ME. Compositions of the Apatite-Group Minerals: Substitution Mechanisms and Controlling Factors. Rev Mineral Geochem. 2002; 48: 13-49.

[46] Qu H, Vasiliev AV, Aindown M, Wei M. Incorporation of Fluorine Ions in Hydroxyapatite by a pH Cycling Method. J Mater Sci: Mater Med. 2005; 16: 447-453.

[47] Qu H, Wei M. Synthesis and Characterization of Fluorine-Containing Hydroxyapatite by a pH-Cyclic Method. J Mater Sci: Mater Med. 2005; 16: 129-133.

[48] Cazalbou S, Eichert D, Ranz X, Drouet C, Combes C, Hamand MF, Rey C. Ion exchanges in apatites for biomedical applications. J Mater Sci: Mater Med. 2005; 16: 405-409.

[49] Miyaji F, Kono Y, Suyama Y. Formation and structure of zinc-substituted calcium hydroxyapatite. Mater Res Bull. 2005; 40: 209-220.

[50] Ren F, Xin R, Ge X, Leng Y. Characterization and structural analysis of zinc-substituted hydroxyapatites. Acta Biomater. 2009; 5: 3141-3149.

[51] Ergun C, Webster TJ, Bizios R, Doremus RH. Hydroxylapatite with substituted magnesium, zinc, cadmium, and yttrim. JBMR:A. 2002; 59: 305-311.

[52] Guerra-Lopez J, Pomés R, Della Védova CO, Viña R, Punte G. Influence of nickel on hydroxyapatite crystallization. J Raman Spectrosc. 2001; 32: 255-261.

[53] Suchanek WL, Byrappa K, Shuk P, Riman RE, Janas VF, TenHuisen KS. Preparation of magnesium-substituted hydroxyapatite powders by the mechanochemical-hydrothermal method. Biomaterials. 2004; 25: 4647-4657.

[54] Ren F, Leng Y, Xin R, Ge X. Synthesis, characterization and ab initio simulation of magnesium-substituted hydroxyapatite. Acta Biomater. 2010; 6: 2787-2796.

[55] Bigi A, Falini G, Foresti E, Ripamonti A. Magnesium influence on hydroxyapatite crystallization. J Inorg Biochem. 1993; 49: 69-78.

[56] Li Y, Nam CT, Ooi CP. Iron(II) and manganese(II) substituted hydroxyapatite nanoparticles: characterization and cytotoxicity analysis. J Phys Conf Ser. 2009; 187: 012024.

[57] Sutter B, Hossner LR, Ming DW. Dissolution kinetics of Iron-, Manganese-, and Copper-Containing Synthetic Hydroxyapatites. Soil Sci Am J. 2005; 69: 362-370.

[58] Pon-On W, Meejoo S, Tang IM. Substitution of manganese and iron into hydroxyapatite: core/shell nanoparticles. Mater Res Bull. 2008; 43: 2137-2144.

[59] Paluszkiewicz C, Slosarczyk A, Pajocha D, Sitarz M, Bucko M, Zima A, Chroscicka A, Lewndiwska-Szumiel M. Synthesis, structural properties and thermal stability of Mn-doped hydroxyapatite. J Mol Struct. 2010; 976: 301-309.

[60] Ciobanu CS, Iconaru SL, Massuyeau F, Constantin LV, Costescu A, Predoi D. Synthesis, Structure and Luminescent Properties of Europium-Doped Hydroxyapatite Nanocrystalline Powders. J Nanomater. 2012; 2012: 942801.

[61] Get'man EI, Loboda SN, Tkachenko TV, Yablochkova NV, Chebyshev KA. Isomorphous Substitutions of Samarium and Gadolinium for Calcium in Hydroxyapatite Structure. Russ J Inorg Chem. 2010; 55: 333-338.

[62] Jiang M, Terra J, Rossi AM, Morales MA, Baggio Saitovitch EM, Ellis DE. $Fe^{2+}/Fe^{3+}$ substitution in hydroxyapatite: Theory and experiment. Phys Rev B: Condens Matter Mater Phys. 2002; 66: 224107.

[63] Wang J, Nonami T, Yubata K. Synthesis, structure, and photophysical properties of iron containing hydroxyapatite prepared by a modified pseudo-body solution. J Mater Sci: Mater Med. 2008; 19: 2663-2667.

[64] Wu HA, Wang TW, Sun JS, Wang WH. A novel biomagnetic nanoparticle based on hydroxyapatite. Nanotechnology. 2007; 18: 9pp.

[65] Morrissey R, Rodriguez-Lorenzo LM, Gross KA. Influence of ferrous iron incorporation on the structure of hydroxyapatite. J Mater Sci: Mater Med. 2005; 16: 387-392.

[66] Gross KA, Jackson R, Cashion JD, Rodriguez-Lorenzo LM. Iron Substituted Apatites: A Resorbable Biomaterials with Potential Magnetic Properties. Eur Cells Mater. 2002; 3: 114-117.

[67] Prakash KH, Kumar R, Ooi CP, Sritharan T, Cheang P, Khor KA. Wet Chemical Synthesis and Magnetic Property Studies of Fe (III) Ion Substituted Hydroxyapatite. MCB. 2006; 3: 177-178.

[68] Pankhurst QA, Connolly J, Jones SK, Dobson J. Application of magnetic nanoparticles in biomedicine. J Phys D: Appl Phys. 2003; 36: R167-R181.

[69] Duguet E, Vasseur S, Mornet S, Devoisselle JM. Magnetic nanoparticles and their applications in medicine. Nanomedicine. 2006; 1: 157-168.

[70] Jain TK, Richey J, Strand M, Leslie-Pelecky DL, Flask CA, Labhasetwar V. Magnetic nanoparticles with dual functional properties: Drug delivery and magnetic resonance imaging. Biomaterials. 2008; 29: 4012-4021.

[71] Lu AH, Salabas EL, Schüth F. Magnetic Nanoparticles: Synthesis, Protection, Functionalization, and Application. Agnew Chem, Int Ed. 2007; 46: 1222-1244.

[72] Gupta AK, Gupta M. Synthesis and surface engineering of iron oxide nanoparticles for biomedical applications. Biomaterials. 2005; 26: 3995-4021.

[73] Tiwari G, Tiwari R, Sriwastawa B, Bhati L, Pandey S, Pandey P, Bannerjee SK. Drug delivery systems: An updated review. Int J Pharm Investig. 2012; 2: 2-11.

[74] Allen TM, Cullis PR. Drug Delivery Systems: Entering the Mainstream. Science. 2004; 303: 1718-1822.

[75] Kumar CSSR. Tissue, Cell and Organ Engineering. Weinheim: Wiley-VCH; 2006.

[76] Enderle J, Blanchard S, Bronzino J. Introduction to Biomedical Engineering. San Diego: Academic Press; 2000.

[77] Westbrook C, Kaut C. MRI in Practice. Oxford: Blackwell Scientific Publications; 1993.

[78] Na HB, Song IC, Hyeon T. Inorganic Nanoparticles for MRI Contrast Agents. Adv Mater. 2009; 21: 2133-2148.

[79] Streffer C. Hyperthermia and the Therapy of Malignant Tumors. Berlin: Springer-Verlag; 1987.

[80] Lee JH, Jang J, Choi J, Moon SH, Noh S, Kim J, Kim JG, Kim IS, Park KI, Cheon J. Exchange-couples magnetic nanoparticles for efficient heat induction. Nat Nanotech. 2011; 6: 418-422.

[81] Markides H, Rotherham M, El Haj AJ. Biocompatibility and Toxicity of Magnetic Nanoparticles in Regenerative Medicine. J Nanomater. 2012; 2012: 614094.

[82] Kozissnik B, Dobson J. Biomedical applications of mesoscale magnetic particles. MRS Bull. 2013; 38: 927-931.

[83] Singh N, Jenkins GJS, Asadi R, Doak SH. Potential toxicity of superparamagnetic iron oxide nanoparticles (SPION). Nano Reviews. 2010; 1: 5358.

[84] Liu J, Ye X, Wang H, Zhu M, Wang B, Yan H. The influence of pH and temperature on the morphology of hydroxyapatite synthesized by hydrothermal method. Ceram Int. 2003; 29: 629-633.

[85] Bouyer E, Gitzhofer F, Boulos MI. Morphological study of hydroxyapatite nanocrystal suspension. J Mater Sci: Mater Med. 2000; 11: 523-531.

[86] Smickilas I, Onjia A, Raicevic S. Experimental design approach to the synthesis of hydroxyapatite by neutralization method. Sep Purif Technol. 2005; 44: 97-102.

[87] Burge R, Dawson-Hughes B, Solomon DH, Wong JB, King A, Tosteson A. Incidence and Economic Burden of Osteoporosis-related Fractures in the United States, 2005-2025. J Bone Miner Res. 2007; 22: 465-475.

[88] Bowden VR, Greenberg CS. Children and Their Families: The Continuum of Care. Philadelphia: Lippincott Williams & Wilkins; 2010.

[89] Ratner BD, Hoffman AS, Schoen FJ, Lemonds JE. Biomaterials Sciences- An Introduction to Materials in Medicine. San Diego: Elsevier Academic Press; 2004.

[90] Kay MI, Young RA. Crystal Structure of Hydroxyapatite. Nature. 1964; 204: 1050-1052.

[91] Patel N, Best SM, Bonfield W. Characterisation of Hydroxyapatite and Substituted-Hydroxyapatite for Bone Grafting. J Aust Ceram Soc. 2005; 41: 1-22.

[92] Goldfarb D, Bernardo M, Strohmaier KG, Vaughan DEW, Thomann H. Characterization of Iron in Zeolites by X-Band and Q-Band ESR, Pulsed ESR, and UV-Visible Spectroscopies. J Am Chem Soc. 1994; 116: 6344-6353.

[93] Low HR, Phonthammachai N, Maignon A, Stewart GA, Bastow TJ, Ma LL, White TJ. The Crystal Chemistry of Ferric Oxyhydroxyapatite. Inorg Chem. 2008; 47: 11774-11782.

[94] Ennas G Musinu A, Piccaluga G, Zedda D, Gatteschi D, Sangregorio C, Stanger JL, Concas G, Spano G. Characterization of Iron-Oxide Nanoparticles in an Fe2O3-SiO2 Composite Prepared by a Sol-Gel Method. Chem Mater. 1998; 10: 495-502.

[95] Dorozhkin SV, Epple M. Biological and medical significance of calcium phosphates. J Mater Chem. 2004; 14: 2148-2153.

[96] Elliot JC. Structure and Chemistry of the Apatites and Other Calcium Orthophosphates. Amsterdam: Elsevier Science; 1994.

[97] Kramer ER, Morey AM, Staruch M, Suib SL, Jain M, Budnick JI, Wei M. Synthesis and characterization of iron-substituted hydroxyapatite via a simple ion-exchange procedure. J Mater Sci. 2013; 48: 665-673.

[98] Gibson IR, Ke S, Best SM, Bonfield W. Effect of powder characteristics on the sinterability of hydroxyapatite powders. J Mater Sci Mater Med. 2001; 12: 163-171.

[99] Ruys AJ, Sorrell CC, Brandwood A, Milthorpe BK. Hydroxyapatite sintering characteristics: correlation with powder morphology by high resolution microscopy. J Mater Sci Lett. 1995; 14: 744-747.

[100] Finoli A, McKeef D, Gerlach J, Nettleship I. Phase transformation behavior of hydroxyapatite foams subject to heat treatment. Biomed Mater. 2010; 5: 015004.

[101] Kim SR, Lee JH, Kim YT, Rui DH, Jung SJ, Lee YJ, Chung SC, Kim YH. Synthesis of Si,Mg substituted hydroxyapatites and their sintering behaviors. Biomaterials. 2003; 24: 1389-1398

[102] Qiu ZY, Li G, Zhang YQ, Liu J, Hu W, Ma J, Zhang SM. Fine structure analysis and sintering properties of Si-doped hydroxyapatite. Biomed Mater. 2012; 7: 045009.

[103] ASTM Standard F 394, 1996, "Test Method for Biaxial Flexure Strength (Modulus of Rupture) of Ceramic Substrates," ASTM International, West Conshohocken, PA, 2003, DOI: 10.1520/F0394-78R96, www.astm.org.

[104] Reed JS. Principles of Ceramic Processing: 2nd Edition. New York: John Wiley & Sons Inc; 1995.

[105] Pattanayak DK, Divya P, Upadyay S, Prasad RC, Bao BT, Rama Mohan TR. Synthesis and Evaluation of Hydroxyapatite Ceramics. Trends BiomaterArtif Organs. 2005; 18: 87-92.

[106] Pattanayak DK, Dash R, Prasad RC, Rao BT, Rama Mahan TR. Synthesis and sintered properties evaluation of calcium phosphate ceramics. Mater Sci Eng C. 2007; 27: 654-690.

[107] An YH, Draughn RA. Mechanical Testing of Bone and Bone-Implant Interface. Boca Raton: CRC Press; 2000.

[108] Ruys AJ, Wei M, Sorrell CC, Dickson MR, Brandwood A, Milthorpe BK. Sintering effects on the strength of hydroxyapatite. Biomaterials. 1995; 16: 409-415.

[109] Chou YF, Huang W, Dunn JC, Miller TA, Wu BM. The effect of biomimetic apatite structure on osteoblast viability, proliferation, and gene expression. Biomaterials. 2005; 26: 285-295

[110] Nebe JB, Müller L, Lüthen F, Ewald A, Bergemann C, Conforto E, Müller FA. Osteoblast response to biomimetically altered titanium surfaces. Acta Biomater. 2008; 4: 1985-1995.

[111] Oreffo ROC, Driessens FCM, Planell JA, Triffitt JT. Growth and differentiation of human bone marrow osteoprogenitors on novel calcium phosphate cements. Biomaterials. 1998; 19: 1845-1854.

[112] Stojanovic Z, Veselinovic L, Markovic S, Ignjatovic N, Uskokovic D. Hydrothermal Synthesis of Nanosized Pure and Cobalt-Exchanges Hydroxyapatite. Mater Manuf Process. 2009; 24: 1096-1103.

[113] Veselinovic L, Karanovic L, Stojanovic Z, Bracko I, Markovic S, Ignajatovic N, Uskokovic D. Crystal structure of cobalt-substituted calcium hydroxyapatite nanopowders prepared by hydrothermal processing. J Appl Crystallogr. 2010; 43: 320-327.

[114] Tank KP, Chudasama KS, Thaker VS, Joshi MJ. Cobalt-doped nanohydroxyapatite synthesis, characterization, antimicrobial and hemolytic studies. J Nanopart Res. 2013; 15: 1644.

[115] Moseke C, Gelinsky M, Groll J, Gbureck U. Chemical characterization of hydroxyapatite obtained by wet chemistry in the presence of V, Co, and Cu ions. Mater Sci Eng C. 2013; 33: 1654-1661.

[116] Jia M, Hong Y, Duan S, Liu Y, Yuan B, Jiang F. The influence of transition metal ions on collagen mineralization. Mater Sci Eng C. 2013; 33: 2388-2406.

[117] Browning E. Toxicity of Industrial Metals, 2nd ed. London: Butterworth & Co.; 1969.

[118] Carson BL, Ellis III HV, McCann JL. Toxicology and Biological Monitoring of Metals in Humans. Boca Raton: Lewis Publishers; 1986.

[119] Tkaczyk C, Petit A, Antoniov J, Zukor DJ, Tabrizian M, Huk OL. Significance of Elevated Blood Metal Ion Levels in Patients with Metal-on-Metal Prostheses: An Evaluation of Oxidative Stress Markers. Open Orthop J. 2010; 4: 221-227.

[120] Wei M, Uchida M, Kim H, Kokubo T, Nakamura T. Apatite-Forming Ability of CaO-Containing Titania. Biomater. 2002; 23: 167-172.

[121] Elkabouss K, Kacimi M, Ziyad M, Ammar S, Bozon-Verduraz F. Cobalt-exchanged hydroxyapatite catalysts: Magnetic studies, spectroscopic investigations, performance in 2-butanol and ethane oxidative dehydrogenations. J Catal. 2004; 226: 16-24.

[122] Borod-ko YG, Vetchinkin SI, Zimont SL, Ivleva IN, Shul'ga YM. Nature of satellites in x-ray photoelectron spectra XPS of paramagnetic cobalt (II) compounds. Chem Phys Lett. 1976; 42: 264-267.

[123] Ignjatovic N, Ajdukovic Z, Savic V, Najman S, Mihailovic D, Vasiljevic P, Stojanovic Z, Uskokovic V, Uskokovic D. Nanoparticles of cobalt-substituted hydroxyapatite in regeneration of mandibular osteoporotic bones. J Mater Sci Mater Med. 2013; 24: 343-354.

[124] Cheng ZH, Yasukawa A, Kandor K, Ishikawa T. FTIR Study of Adsorption of $CO_2$ on Non Stoichiometric Calcium Hydroxyapatite. Langmuir. 1998; 14: 6681-6686.

[125] Dee KC, Puleo DA, Bizios R. An Introduction to Tissue-Biomaterial Interactions. Hoboken: Wiley-Liss; 2002.

[126] Wu C, Zhou Y, Fan W, Han P, Chang J, Yuen J, Zhang M, Xiao Y. Hypoxia-mimicking mesoporous bioactive glass scaffolds with controllable cobalt ion release for bone tissue engineering. Biomaterials. 2012; 33: 2076-2085.

[127] Mikawa M, Kato H, Okumura M, Narazaki M, Kanazawa Y, Miwa N, Shinohara H. Paramagnetic Water-Soluble Metallofullerenes Having the Highest Relaxivity for MRI Contrast Agents. Bioconjugate Chem. 2001; 12: 510-514.

[128] Strijkers GJ, Mulder WJM, von Heeswijk RB, Frederik PM, Bomans P, Magusin PCMM, Nicolay K. Relaxivity of liposomal paramagnetic MRI contrast agents. Magn Reson Mater Phys. 2005; 18: 186-192.

[129] Schenck JF. Safety of Strong, Static Magnetic Fields. J Magn Reson Im. 2000; 12: 2-19.

[130] Lide DR. Handbook of Chemistry and Physics, 85th ed. Boca Raton: CRC Press; 2004.

[131] Afshari FT, Kwok JC, Andrews MR, Faissner A, Ffrench-Constant C, Fawcett JW. Integrin activation or alpha 9 expression allows retinal pigmented epithelial cell adhesion on Bruch's membrane in wet age-related macular degeneration.

[132] Rabinovitch M, DeStefano MJ. Manganese stimulates adhesion and spreading of mouse sarcoma I ascites cells. J Cell Bio. 1973; 59: 165-176.

[133] Zhang Z, Gu B, Zhu W, Zhu L. Integrin mediated osteoblastic adhesion on porous manganese-incorporated $TiO_2$ coating prepared by plasma electrolytic oxidation. Exp Ther Med. 2013; 6: 707-714.

[134] Fujitani W, Hamada Y, Kawaguchi N, Mori S, Daito K, Uchinaka A, Matsumoto T, Kajima Y, Daito M, Nakano T, Matsuura N. Synthesis of Hydroxyapatite Containing Manganese and Its Evaluation of Biocompatibility. Nano Biomedicine. 2010; 2: 37-46.

[135] Kizukii T, Ohgaki M, Nakamura S, Hashimoto K, Toda Y, Yamashita K. Synthesis of New Biocompatible Apatite-type Rare-earth Silicates. Key Eng Mat. 2003; 240-242: 559-562.

[136] Herath HMTA, DiSilvio L, Evans JRG. In vitro evalutation of samarium (III) oxide as a bone substituting material. JBMR:A. 2010; 94: 130-136.

[137] Patra CR, Maneim SSA, Wang E, Dutta S, Patra S, Eshed M, Mukherjee P, Gedanken A, Shah VH, Mukhopadhyay D. In vivo toxicity studies of europium hydroxide nanorods in mice. Toxicol Appl Pharm. 2009; 240: 88-98.

**Appendix: Manganese substituted hydroxyapatite – preliminary results**

*Trial 1:*

*Materials and Methods:* Initially, manganese substitution was attempted using the same procedure as that detailed for iron substitution. Hydroxyapatite powder was prepared via a wet precipitation method based on previous work done by Kothapelli et al. [48]. Briefly, a volume of 200 mL ammonium phosphate (99+%, Acros) 2 g/dL aqueous solution was added dropwise at a moderate dropping rate under vigorous stirring to 600 mL of an aqueous calcium nitrate tetrahydrate (99%, Fisher) solution of the same concentration at 75°C. An 80 mL volume of ammonium hydroxide (~30%, Fisher) was also added to the mixed solution to bring up the pH to 11-12. After 3 hours of stirring at 75°C, the HA particles were collected by filtration and washed thoroughly with deionized water. The collected HA precipitates were vacuum dried for 48 hours at room temperature and ground by mortar and pestle into a fine powder.

HA powder was then subjected to a simple soaking procedure to achieve manganese substitution for calcium in the HA crystal lattice. Manganese (II) chloride (Fisher, 98+%) at a concentration of 0.02M was used as the soaking solution. HA powder was soaked in the manganese solution at an amount of 200 mL of solution per gram of HA, under moderate stirring for one hour, and then collected by filtration and washed thoroughly by deionized water. The powder was dried overnight and ground by mortar and pestle.

*Results:*

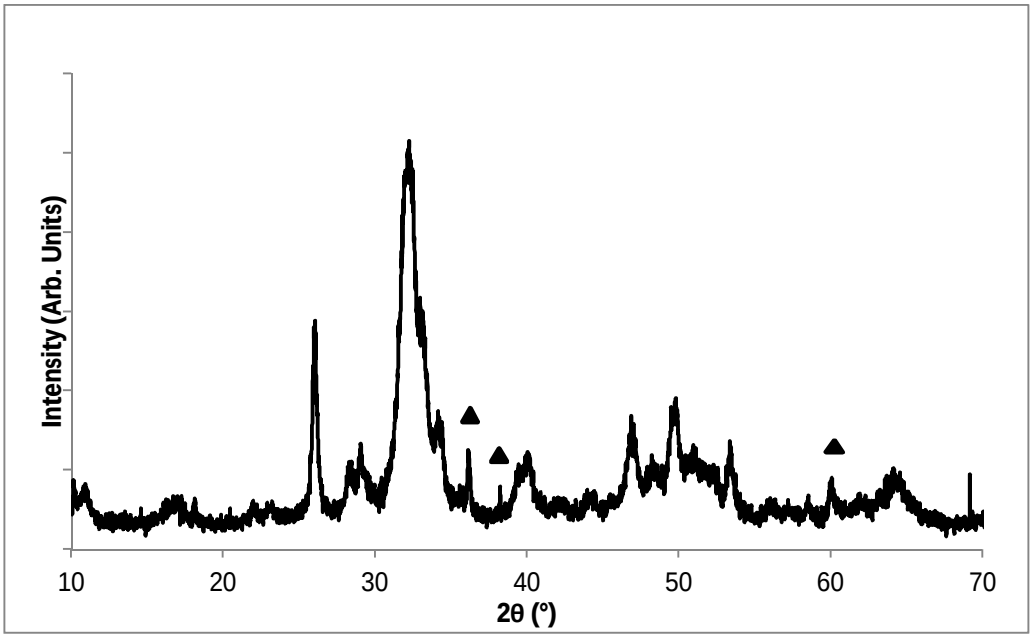


**Figure A.1** XRD plot of MnHA synthesized via simple ion exchange. The triangles indicate extraneous peaks that cannot be matched with HA.

*Conclusion:* The attempt to synthesize MnHA via wet synthesis yielded a material with a secondary phase, most likely $Mn_3O_4$ (JCPD 18-803).

*Trial 2:*

*Materials and Methods:* Manganese incorporation via wet synthesis was also attempted. A quantity of manganese (II) chloride that would allow for 10 wt% substitution was added to the phosphate containing solution. The rest of the synthesis was conducted exactly as described in the first paragraph of the Trial 1 section.

*Results:*

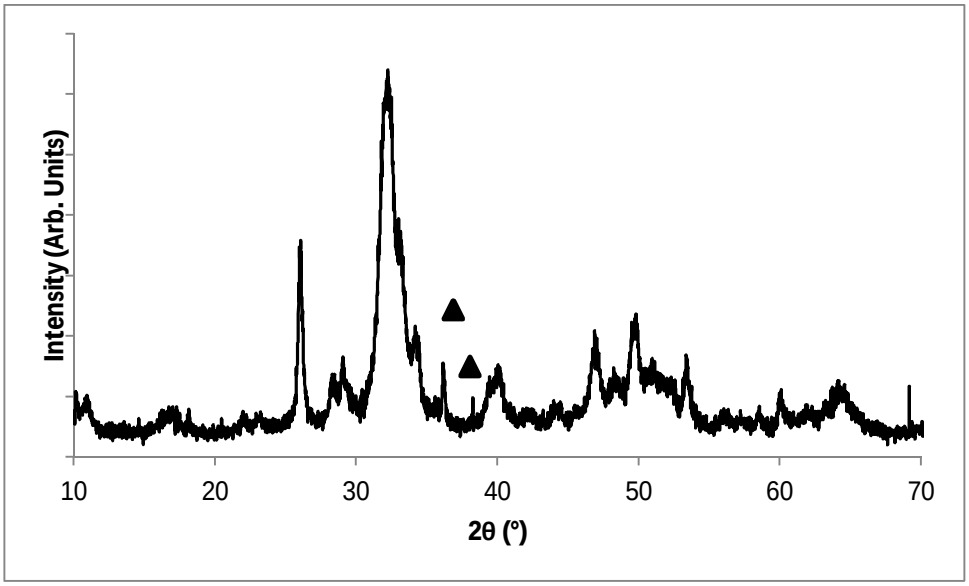


**Figure A.2** XRD plot of MnHA synthesized via simple ion exchange. The triangles indicate extraneous peaks that cannot be matched with HA.

*Conclusion:* The attempt to synthesize MnHA via wet synthesis yielded a material with a secondary phase, most likely $Mn_3O_4$ (JCPD 18-803).

*Trial 3:*

*Materials and Methods:* HA powder was synthesized as described above. The HA was then subjected to ion exchange using a slightly modified simple soaking procedure to achieve manganese substitution for calcium in the HA crystal lattice. Manganese (II) chloride (Fisher, 98+%) at a concentration of 0.02M was used as the soaking solution, with the pH adjusted to 4 with HCl. HA powder was soaked in the manganese solution at an amount of 200 mL of solution per gram of HA, under moderate stirring for one hour, and then collected by filtration

and washed thoroughly by deionized water. The powder was dried overnight and ground by mortar and pestle.

*Results:*

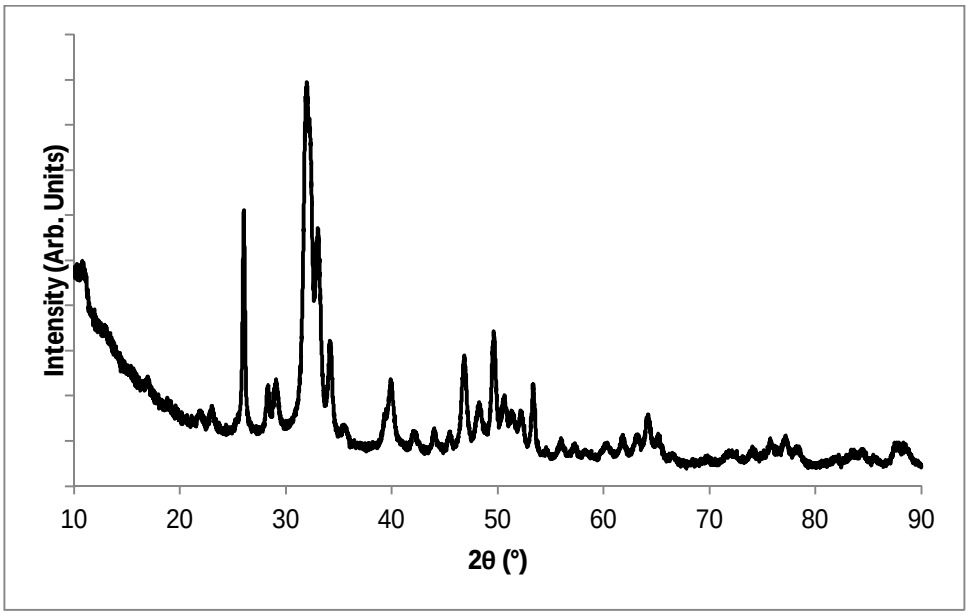


**Figure A.3** XRD plot of MnHA synthesized via simple ion exchange with controlled pH. No obvious extraneous peaks are present.

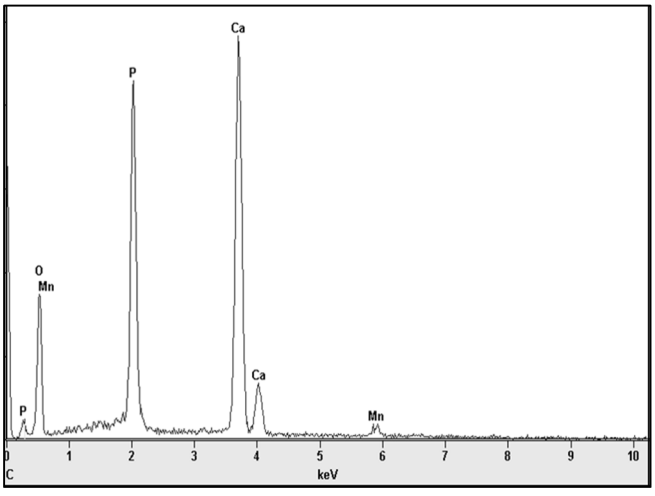


**Figure A.4** EDX spectra of MnHA synthesized via simple ion exchange with controlled pH verifying the presence of manganese in the powder.

*Conclusions:* Using a simple ion exchange procedure with a controlled acidic pH, MnHA can be achieved. Preliminary characterizations indicate a pure apatite resulting structure using this method. The adjustment of the soaking solution pH likely led to a successful substitution due to the fact that $Mn^{2+}$ is more thermodynamically stable at lower pH compared to $Mn_3O_4$, which becomes thermodynamically favorable as neutral and alkaline pH is approached. Additionally, the acidic aqueous conditions help facilitate substitutions as surface layers of HA become loosely bound and calcium deficient. This powder needs to be more fully characterized, but it may be an attractive material for tissue engineering applications due to manganese's promotion of cell adhesion. If this material is found to have magnetic properties it can also be applied to a wider range of biomedical applications including drug delivery, MRI imaging, and hyperthermia treatments.